SUPPRESSION OF MAGNETISM BY SPIN-ORBIT COUPLING AND BINDING-LIMITED DEINTERCALATION KINETICS REVEALED IN NEW HONEYCOMB IRIDATES

by
DAVID COOPER WALLACE

A dissertation submitted to Johns Hopkins University in conformity with the requirements for the degree of Doctor of Philosophy

Baltimore, Maryland
May, 2016

1 Abstract

Iridium oxide materials (*iridates*) are an exciting class of compounds for physicists and materials scientists, as they host a rare meeting between several different types of electronic interactions. In iridates, strong bonds between iridium and oxygen cooperate with electron-electron repulsion to force the highest energy electrons in the material to remain localized on the iridium atoms. These localized, unpaired electrons behave strangely due to a relativistic effect called spin orbit coupling (SOC): the interaction between an electron's spin and the magnetic field generated by its orbit around the heavily charged iridium nucleus. This unique meeting between strong bonding, coulombic repulsion and SOC interactions has been the focus of significant theoretical and experimental attention in recent years, particularly with regard to iridates that form two dimensional honeycomb lattices. The so-called honeycomb iridates received significant attention after the proposal that they could host a rare, cutting-edge magnetic state known as a spin liquid. Despite this attention, precious few materials have been discovered in which the theory describing electronic and magnetic behavior in honeycomb iridates can be developed and investigated. This dissertation presents the results of several exploratory syntheses and detailed experimental investigations that have culminated in the discovery of three new honeycomb iridates and yielded significant insight into the influence of spin-orbit coupling in iridium compounds. It also demonstrates an important case of a solid state reaction in which diffusion is not the rate limiting step, which is a key insight that can be used to drive innovation in materials chemistry and battery technology.

Chapter 3 presents the results of a detailed study on defects and disorder in a canonical honeycomb iridate, Na_2IrO_3, by controlled chemical doping and careful structural characterization of a new solid solution, $Na_{3-\delta}(Na_{1-x}Mg_x)Ir_2O_6$. These results ultimately show how even small concentrations of sodium vacancy defects, chemical doping and structural disorder can dramatically affect the material's magnetic properties. This work also hints at the strong influence of iridium's spin orbit coupling.

In chapter 4, the structures and basic physical properties of two new honeycomb iridates, $NaIrO_3$ and $Sr_3CaIr_2O_9$, are reported. These new iridates are the first of their kind, as all of the iridium metal centers exist in the 5+ oxidation state. Conventional crystal field theory suggests these materials should be magnetic with a total of two unpaired electrons and $S = 1$, but magnetic susceptibility measurements and neutron scattering show complete suppression of magnetism. We demonstrate that this non-magnetic state occurs due to a strong spin-orbit interaction in the Ir^{5+} ion.

In the final chapter, the kinetics of the heterogeneous solid–liquid Na^+ ion deintercalation reaction between Na_2IrO_3 and an oxidizing solution are shown to be determined by the binding affinity of the solution-phase oxidant at temperatures above $T \approx 0°C$. This result is contrary to the belief that diffusion in the solid is always the rate-limiting step in such reactions, and provides insight that can be used to synthesize new materials and potentially improve the performance of modern lithium and sodium ion batteries.

Dissertation committee

Advisor *– Professor Tyrel M. McQueen*

Professor John D. Tovar

Professor V. Sara Thoi

For my parents

Acknowledgments

The research presented in this work was primarily made possible by the guidance and vision of my advisor, Professor Tyrel McQueen. Tyrel has motivated me to become a better scientist by sharing his own passion and knowledge in a way that cannot be mimicked. He constantly pushes for more work and new results, but does so in a way that illustrates his genuine interest in the wellbeing of his students. I feel extremely fortunate and proud to call myself a member of his research group, and I cannot wait to see the scientific innovations and talented scientists that his efforts will continue to produce.

I extend my gratitude to Professors J.D. Tovar, Sara Thoi, Jerry Meyer, Todd Hufnagel and Nina Markovic for the help and feedback they have provided as members of my oral and thesis committees. I also wish to thank my professors and mentors, particularly Professors Douglas Poland, Art Bragg, Tamás Budavari and Howard Fairbrother, whose engaging lectures and demanding coursework laid the foundation for my graduate studies. In addition, numerous staff members, including Jean Goodwin, Rosalie Elder, Boris Steinberg, David Brewster, Joe Russel and Brian Schriver have been tremendously helpful to me throughout graduate school. Many thanks to all of you for your hard work.

Special thanks is due to Prof. James R. Neilson, Dr. Seyed Koopayeh, Dr. W. Adam Phelan, and Prof. Allyson Fry-Petit who, in addition to providing countless hours of technical assistance and mentorship, were incredible sources of encouragement throughout my graduate studies. To the many members of the McQueen lab with whom I have worked many hours and shared many experiences, Dr. John Sheckelton, Dr. Patrick Cottingham, Kathryn Arpino, Benjamin Trump, Zachary Kelly, Jessica Panella, Benjamin Wasser, Jacob Tutmaher, Jennifer Morey, Artem Talanov, and many other talented undergraduates: your company and collaboration has been invaluable to me, and I could not have asked for a more passionate and intellectually stimulating group of people to work with. I thank you all sincerely, and wish you the best of luck in your lives and careers.

This work would not have been completed without the support and companionship of

many dear friends and family. In particular, I wish to thank Christopher Malbon and Tyler Chavez, whose friendship has been an invaluable source of support and an outlet for frustration. Thanks to my brother, Connor Wallace, whose hours of programming assistance added significant strength to my work. I am sincerely grateful to my grandfather, Jim Gelatt, for taking an active interest in my education and wellbeing. I also wish to thank Annabel Hudson for her unshakable love, companionship and encouragement. Finally, I owe the most thanks to my parents, Tim and Beth, who always strove to provide the best for me and encouraged me to pursue my passions. Without their constant love and support, this dissertation would never have been written.

Table of Contents

List of Figures

List of Tables

2 Introduction

In a Venn diagram of scientific disciplines, the region of overlap between chemistry, physics, and materials science comprises a field known as *materials and solid state chemistry*. Scientists working in this multidisciplinary field must develop deep chemical intuition, maintain close contact with developments in physical theory, and be well versed in materials characterization techniques. Further, because materials chemistry remains largely an exploratory field, the solid state chemist must be inquisitive and persistent, and maintain an eye for the unexpected. An excellent example of the impact made by such researchers is the discovery of high-T_C superconductivity in copper oxide materials. After studying the theory of superconductivity developed by Bardeen, Cooper and Schriefer, Bednorz and Müller hypothesized that transition metal oxides with Jahn-Teller active metal centers could host a unique combination of electron mobility and lattice vibrations that would give rise to superconductivity at high temperatures. This hypothesis was outlandish at the time, as most transition metal oxides do not conduct electricity well, but their willingness to explore paid off enormously. Their discovery in 1986 of high-T_C superconductivity in the Ba-La-Cu-O system [1] earned them the Nobel prize in physics, and ultimately forced a paradigm shift in the study of superconductivity. Despite significant progress in both theoretical physics and materials engineering, exploratory research remains necessary for fields in which large gaps in theory still exist.

This dissertation describes several key insights that were revealed by the synthesis of new compounds in a small family of materials known as *honeycomb iridates*. While the experienced materials chemist may wish to skip directly to chapters 3-5 to view the new research, in this chapter I will attempt to quickly paint an intuitive picture of chemical bonding in solids that will aid the less experienced reader in understanding the results detailed in subsequent chapters. Before getting started, however, it is important to note that this discussion will leave a large gap in the reader's understanding with respect to the concept of *symmetry*, the mathematical framework for which is known as *group theory*. Group theory forms the foundation upon which much of chemistry and physics are based, and is crucial to our understanding of chemical bonding and the behavior of crystalline solids. In spite of the necessity of group theory, this introduction will make only passing reference to group theoretical concepts, and will instead focus heavily on a more basic interpretation of bonding in solids. The reader is directed to references [2, 3] for a much more thorough introduction to group theory.

2.1 Energy and Entropy

Throughout this introduction frequent reference will be made to the concepts of *energy* and *entropy*, which are fundamental physical quantities in thermodynamics that are key to our understanding of physical phenomena and chemical reactivity. Energy comes in many forms, including light, motion, chemical bonds, and gravity. Energy and entropy are governed by the laws of thermodynamics, listed below.

- **Zeroeth Law**: If two separate systems are in equilibrium with a third system, then they must be in equilibrium with one another.

The zeroeth law is often omitted in discussions of the laws of thermodynamics because it is, in a sense, quite intuitive. Put in a different way, the zeroeth law implies that a low-energy system cannot give energy to a high-energy system.

- **First Law**: Energy is conserved.

Energy can be converted to a different type in a process, but it cannot be created or destroyed. For instance, when light shines onto a darkly colored surface, its energy is converted to heat (vibrations) and excited electronic states on the surface.

- **Second Law**: The entropy or "randomness" of the universe is always increasing.

Put another way, when an energy-transfer process occurs in an isolated system, the total potential energy of the system decreases by an amount called the entropy. More potential energy can be added to the system from the surroundings, but this in turn increases the entropy of the surroundings.

- **Third Law**: The entropy of a perfect crystal at absolute zero is exactly zero.

This law allows for a rigorous definition of entropy: the number of states with equivalent energy. A perfectly ordered crystal has only one possible ground state, and thus the entropy of such a system is zero. In practice, such a crystal cannot be obtained, and certain small amount of residual entropy will always be trapped when a material is cooled close to absolute zero.

These laws lead to a a very basic rule for chemical reactions: chemical systems will always seek to minimize their energy and increase their entropy, and any process that increases the energy or reduces the entropy of a system requires an external energy source and a net gain in entropy for the system's surroundings.

2.2 Wavefunctions and Atomic Structure

To understand how atoms bond together, one must first understand how they are structured in isolation. The chemist's understanding of an atom's structure has its roots in the work of Erwin Schrödinger, who showed that when a particle is confined to a small area, its wave-like nature forces it to form standing waves or *stationary states* within that defined

space that are distinct and discrete. They are also necessarily symmetric, as they cannot vary in time and cannot exhibit a net polarization. Because these stationary states are oscillatory (i.e. wavelike) in nature and cannot exhibit asymmetry, they are distinguished by the number of nodes in their waveform, which can be related to a discrete variable n, called a *quantum number*. By constructing the Schrödinger equation for a given system, one can solve for the stationary states of that system, which are referred to as *wavefunctions*. Wavefunctions are special because they provide a complete description of a quantum-mechanical system, and can be used to calculate classical-mechanical observables such as energy and angular momentum. A wavefunction also has the unique property that computing its square (the product of the wave function and its complex-conjugate) yields a probability distribution that describes the spatial characteristics of the wavefunction. A common toy system used to illustrate these concepts is a particle confined to a 1-dimensional box, where the edges of the box have an infinite repulsive potential. The solutions to the Schrödinger equation for a particle in a 1-D box, shown in Figure 2.1, give a qualitative description of the concepts necessary to understand wavefunctions: phase and probability density. The first stationary state is the lowest in energy (E_1) of the particle in a box, and consists of a broad wave with nodes at both of the boxes edges. This wave can have either positive or negative phase, and is symmetric about the center of the box. Multiplying this wavefunction ψ by its complex conjugate ψ^* yields the probability density function, which goes to zero at the edges and has a maximum at the center. The second lowest energy (E_2 state has a additional node at the center of the box, and exhibits a phase change between each half of the box. Computing the density function $\psi\psi^*$ confirms the presence of the third node, as the density function goes to zero at the box center. Note that the number of nodes is directly related to the wave function's energy, A linear combination (i.e. addition) of the two lowest energy states is called a *superposition*. In combining two states, the phase of each state is important: areas of the two wavefunctions that have the same phase will exhibit constructive interference resulting in amplification of the wave in that area, while

areas in which the wavefunctions have opposite phase will exhibit destructive interference resulting in attenuation of the wave. In the case of the superposition of states 1 and 2, the pattern of constructive and destructive interference leads to a net polarization in the particle's positional density that must vary as a function of time with frequency $\omega = \frac{E_2 - E_1}{\hbar}$. The concept of interference is crucial to our understanding of chemical bonds and many other important phenomena.

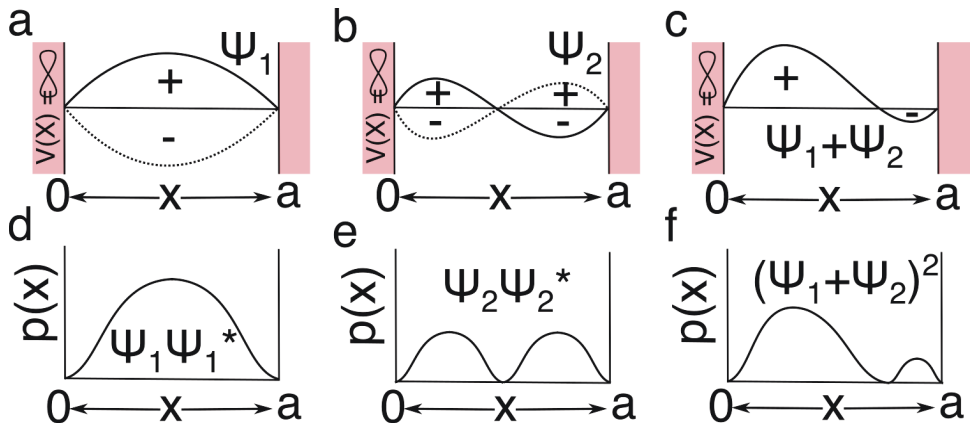

Figure 2.1: a, b) A graphical representation of the wavefunctions for the first and second lowest energy wavefunctions (ψ_1, ψ_2) of a particle confined to a 1-dimensional box. The + and - symbols indicate the phase of the wavefunction as a function of the particle's position x in the box. **c)** A superposition of two states ψ_1 and ψ_2. Multiplying a wavefunction ψ by its complex congugate ψ^* yields a probability density function that can be used to visualize the shape of the wavefunction in real space. The probability density function for each of the three wavefunctions in parts a-c are shown in parts **d-f)**.

While atomic systems are much more complex than the particle in a box model, one can find exact solutions for several simple atomic systems [5]. By constructing and solving the Schrödinger equation for a hydrogen atom (one electron orbiting a proton), one obtains the "hydrogenic" wavefunctions, which are frequently used to describe chemical bonding in multi-electron systems. The hydrogenic wavefunctions are specified by three quantum numbers: the principal quantum number n, the azimuthal quantum number ℓ, and the magnetic quantum number m_ℓ. Each of these three quantum numbers specifies a different property of the wavefunction: n specifies the energy level or "shell" (energy increases

Table 2.1: Quantum numbers determined from solutions to the Schrödinger equation for the hydrogen atom.

Quantum number	**Symbol**	**Values**
principle	n	$1, 2, 3, 4$ ...
azimuthal	ℓ	$0, 1, 2$ ... $(n-1)$
magnetic	m_ℓ	$0, \pm 1, \pm 2, \pm 3$ ... $\pm \ell$

with n), ℓ is related to the orbital angular momentum which determines the subshell (shape) within a given energy level, and m_ℓ specifies the orientation within a given energy level and subshell. The allowed values of these quantum numbers are listed in Table 2.1. For the remainder of this discussion, we will consider the word "orbital" to indicate a specific combination of n, ℓ and m_ℓ.

In visualizing electronic orbitals, it is common practice to draw density and phase in the same picture by coloring one half of the electronic density. Figure 2.2(a) shows the 1*s* (n = 1, ℓ = 0, m_ℓ = 0), 2*p* (n = 2, ℓ = 1, m_ℓ = -1, 0, 1) and 3*d* (n = 3, ℓ = 2, m_ℓ = -2, -1, 0, 1, 2) orbitals in 3-dimensions with shading to indicate phase. Note that orbitals with different azimuthal components (*s* vs. *p* vs. *d*) have different shapes: while the *s* orbital is perfectly spherical, the *p* orbitals have distinct "dumbbell" shapes, and four of the five *d* orbitals have a "four-leaf clover made of dumbbells" shape. The fifth *d* orbital resembles a "dumbbell inside a doughnut". For this reason, individual orbitals are given symmetry labels to indicate their shape relative to the cartesian coordinate system. While these labels are helpful for remembering the shapes of the orbitals, they are primarily employed to emphasize the ways in which they can interact with the orbitals of other atoms to form bonding and antibonding molecular orbitals.

The chemical properties of an atom are entirely determined by its electrons, and it is therefore important to understand how electrons are organized in an isolated atom. The Pauli exclusion principle states that no two particles can occupy the same quantum state (have the exact same quantum numbers). This necessitates a discussion of the concept of

spin angular momentum, which is parameterized by the quantum number *S*. While *orbital* angular momentum has already been introduced as a quantity that gives rise to an orbital's shape, the electron has a second form of angular momentum that we refer to as "spin" for simplicity. This is not the same spin as, say, a basketball spinning on one's finger, but the analogy to a spinning ball is somewhat instructive, as both are examples of angular momentum. This analogy is also helpful in understanding that spin can only take on one of two distinct values, just as a ball can only spin on an axis clockwise or counter-clockwise. For the purpose of this discussion, the two possible values of s, $+\frac{1}{2}$ and $-\frac{1}{2}$, are referred to as *spin up* and *spin down*. Given that no two electrons can have the exact same quantum number, we know that each combination of n, ℓ and m_ℓ can hold at most two electrons of opposite spin. The Aufbau principle dictates that an electron will preferentially occupy the lowest energy orbital that is unfilled, meaning that electrons "fill" into an atom's orbitals starting from the lowest energy, and pairing up 2 by 2 with opposite spins. The highest energy shell that contains electrons is called the *valence* shell, and the electrons in this shell are called *valence electrons*. It is the valence electrons that primarily contribute to bonding interactions.

The number of unpaired electrons determines a compound's magnetic behavior. A compound with one or more unpaired electrons is said to be *paramagnetic*, and will have an attractive interaction with a magnet. This attractive force is a result of unpaired electrons aligning their spins with the magnetic field. Dioxygen (O_2) is an example of a paramagnetic compound–it has two unpaired electrons per molecule, and is visibly attracted to magnetic fields when liquified. Dinitrogen (N_2) has no unpaired valence electrons, and is said to be *diamagnetic* because it has almost no interaction with a magnetic field (although sensitive instrumentation can detect small repulsive interactions between diamagnetic substances and magnetic fields). For equivalent electronic configurations, Hund's rules dictate that the configuration with the highest number of unpaired spins has the lowest energy.

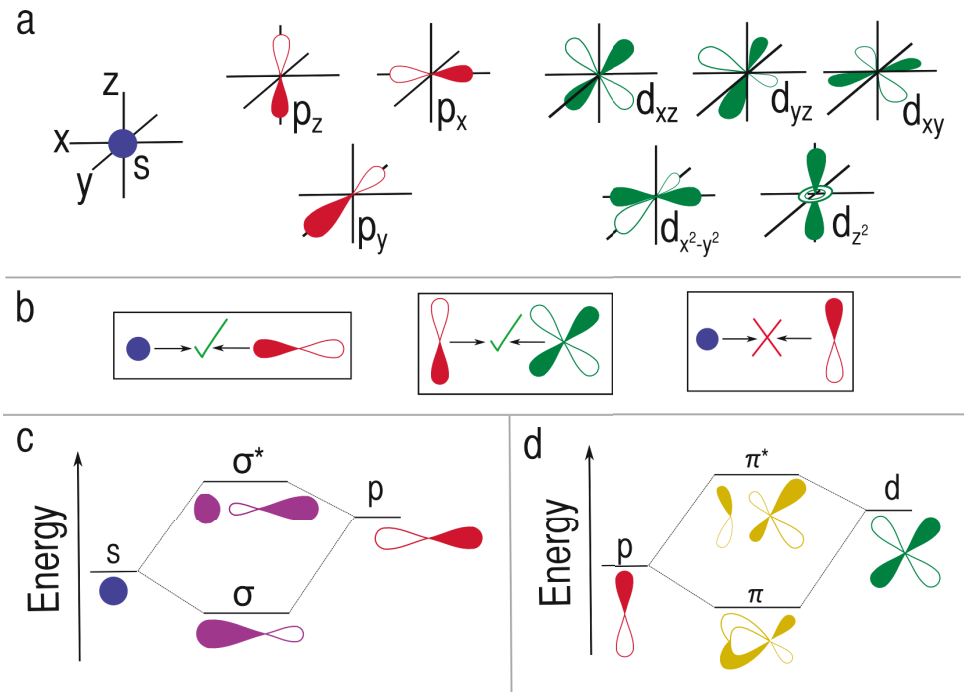

Figure 2.2: **a)** The basic shapes and phases of s-orbitals (blue), p-orbitals (red) and d-orbitals (green) are shown in cartesian (x,y,z) coordinates. **b)** When two atoms are in proximity to one another, electronic orbitals on each atom can overlap with one another if they have the same symmetry with respect to the bonding axis. The s-orbital of one atoms can interact with a p-orbital on another atom if the p-orbital is oriented along the bonding axis, as shown in the first box. This type of one-dimensional bonding as sigma (σ) bonding. Another common type of bond is the pi (π) bond, which is when overlap between orbitals occurs in two dimensions, as shown in the second box. Orbitals that do not share the same symmetry with respect to the bonding axis do not interact, as shown in the third box. **c)** s and p orbitals can overlap to form low- and high-energy states known as bonding and anti bonding orbitals (σ and σ*). **d)** Overlap between p and d orbitals results in π bonding and antibonding pairs.

2.3 Chemical Bonding

Having established an understanding of atomic orbitals in terms of electronic density, phase and symmetry, one can begin to consider cases in which two atoms are brought into close proximity. Figure 2.2(b) illustrates three cases in which electronic orbitals of two different atoms are brought into close contact. In order for the orbitals of two separate atoms to interact with each other, they must have the same phase relationship with respect to the axis formed by both nuclei, referred to here as the *bonding axis*. As a simple example, consider the $1s$ orbital of a hydrogen atom brought into contact with the $2p$ orbital of a fluorine atom: these orbitals can interact with each other because they share the same rotational symmetry–their phases do not change when they are rotated around the axis formed by the two atoms. There are thus only two possible linear combinations of the $1s$ and $2p$ orbitals in this case: one in which both orbitals have the same phase and therefore exhibit constructive interference (*bonding*), and one in which the two orbitals have opposite phase and therefore exhibit destructive interference (*antibonding*). Bonding interactions result in a lower energy, and antibonding interactions result in higher energy. A similar situation arises when two p orbitals are brought together parallel to one another. Because they share the same symmetry with respect to the bonding axis, they can form bonding and antibonding molecular orbitals. When two orbitals that do not share the same symmetry with respect to the bonding axis are brought into proximity, they do not interact and are therefore said to be *non-bonding*. Note that a chemical bond is distinguished by its symmetry with respect to the bonding axis: σ-bonds are formed between orbitals that do not share a nodal plane, while π-bonds are formed between orbitals that share a single nodal plane, and δ bonds have two nodal planes. In general, low order bonds are stronger (lower in energy) than higher order bonds, and while bond orders greater that δ are, in theory, possible, they have not been experimentally observed.

The ability of orbitals to exhibit constructive and destructive interference in the form of orbital overlap provides only half of the information necessary to determine whether or not

a bond will actually form. Take again the example of hydrogen and fluorine: hydrogen has one unpaired valence electron in its $1s$ orbital, while fluorine has a single unpaired valence electron in a $2p$ orbital. When the hydrogen $1s$ orbital comes into contact with the fluorine $2p$ orbital, a σ-bonding interaction results in a low energy σ-bond and a high energy σ*antibond, as shown in Figure 2.2(c). Since each atom contributes only one electron, these electrons pair up in the low energy σ bonding orbital, and the result is a chemical compound HF. Note that by sharing these two electrons, both hydrogen and fluorine have achieved a completely full shell of electrons, thus satisfying what is called the *octet rule* for elements whose valence electrons fall in the p block of the periodic table. The octet rule states that atoms in the p block ($\ell = 2$) will preferentially form bonds that result in a completely filled shell of 8 electrons. This rule is particularly strict for carbon, nitrogen, oxygen and fluorine, which almost universally form 4, 3, 2 and 1 bonds, respectively, in order to achieve a completely filled valence.

Just as fluorine formed a bond with hydrogen to achieve a full shell of 8 electrons, transition metals seek to form bonds in order to fill their outermost shell as well. This is a tall order, as the addition of the d subshell ($\ell = 2$) leaves room for an additional 10 electrons, for a total of 18 desired electrons per metal atom [6]. For this reason, transition metals often form bonds with multiple atoms to form a compound called a *complex*. One of the most common bonding motifs in transition metal-based complexes involves 6 small atoms, commonly referred to as *ligands*, which all bond with a central metal atom. The prevalence of octahedral coordination in metal complexes and solids is a direct consequence of the strong bonding interactions formed between the metal s and p orbitals and σ-type ligands, which form strong σ bonds to the metal center. Figure 2.3 illustrates how octahedral coordination takes place. In isolation, the d-orbitals of a metal atom all have the same energy and are therefore said to be *degenerate*. Considering σ-type ligand-metal interactions only, when 6 atoms approach the metal atom, these sigma ligands have the correct symmetry to interact only with the $d_{x^2-y^2}$ and d_{z^2} orbitals of the metal atom, leaving the d_{xy}, d_{xz} and d_{yz}

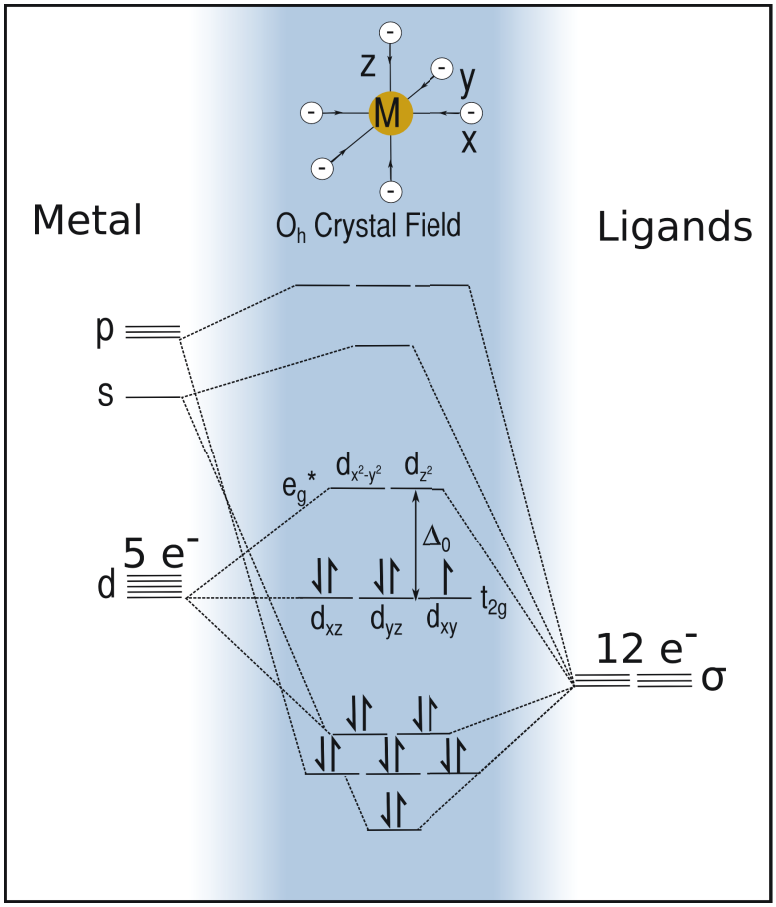

Figure 2.3: Illustration of a d^5 metal ion in an octahedral crystal field formed by 6 σ-donor ligands. The σ ligands form strong bonding interactions with unoccupied metal *s* and *p* orbitals, leaving the metal's remaining valence electrons in *d* orbitals. The $d_{x^2-y^2}$ and d_{z^2} orbitals, causing them to rise in energy. The charges do not interact with the d_{xy}, d_{xy}, or d_{xy} orbitals due to symmetry. Thus in this case, the ground electronic state is five electrons in a threefold degenerate t_{2g} orbital.

orbitals untouched. These symmetry-dependent interactions remove the five-fold degeneracy of the d-orbitals by raising the energy of the $d_{x^2-y^2}$ and d_{z^2} orbitals relative to the others, and result in two distinct sets of orbitals with new symmetry labels and degeneracy. The low energy set, which has three fold degeneracy and consists of the d_{xy}, d_{xz} and d_{yz} non bonding orbitals, is given the symmetry label t_{2g}, while the high energy $d_{x^2-y^2}$ and d_{z^2} orbitals are twofold degenerate and are labeled e_g. The energy difference between these two sets is referred to as the *octahedral crystal field stabilization energy* (Δ_0 or $10Dq$), and is directly dependent on the strength of the ligands and their proximity to the metal. In many transition metal complexes, it is either the t_{2g} or the e_g manifold that holds the highest energy electron, and for this reason the t_{2g} and e_g manifolds are responsible for the majority of the magnetic and optical properties of the complex.

The magnitude of Δ_0 has a significant effect on the magnetic properties of the complex, as it determines the amount of energy required to promote an electron from the t_{2g} to the e_g manifold. If Δ_0 is less than the amount of energy yielded from increasing the number of unpaired spins, the complex will adopt a high-spin configuration in which the spin is maximized at the expense of a small jump between the t_{2g} to the e_g manifold. Because Δ_0 is directly related to the strength and proximity of the bonding ligands, complexes with identical numbers of d-electrons can exist in both high and low spin states. The magnitude of Δ_0 also has a significant effect on the optical properties of the complex, as Δ_0 is often on the order of 0.1 to 1 eV, which is near the visible range of the electromagnetic spectrum. As a result, octahedral transition metal complexes are are often brightly colored, making them excellent for use in dyes and basic optical spectroscopy experiments.

In 1937, H.A. Jahn and E. Teller demonstrated that polyatomic systems with electronic degeneracy will undergo a structural distortion in order to achieve a lower ground state energy [8]. One such example is the low-spin $d5$ electronic configuration of a metal ion in an octahedral crystal field, shown in Figure 2.3. Simple electron filling according to the Pauli exclusion principle yields 5 electrons in a threefold degenerate t_{2g} manifold consisting

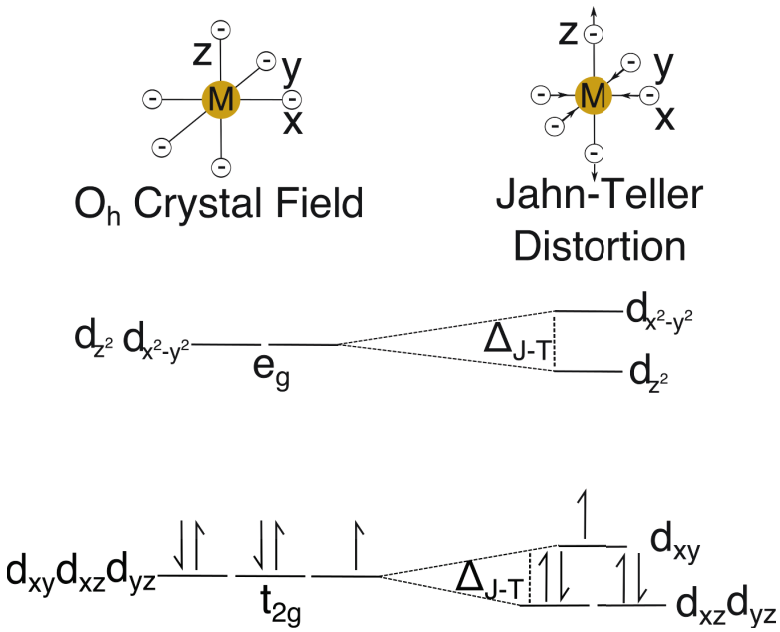

Figure 2.4: Systems with degeneracy may undergo a structural distortion to achieve a lower ground state energy. In the example shown here, a low spin d^5 metal in an octahedral crystal field may exhibit an axial elongation along one axis, resulting in a loss of electronic degeneracy.

of the metal's nonbonding d_{xy}, d_{xz} and d_{yz} orbitals. A elongation of the octahedral crystal field along the z-axis removes the degeneracy in this manifold by lowering energies of the d_{xz} and d_{yz} orbitals relative to the d_{xy} orbital. This distortion results in a lower ground state energy. Despite the clear predictions made by Jahn and Teller's theory, a static Jahn-Teller distortion was not documented until over a decade later by Bleaney, Bowers and Trenam, who were able to observe the distortion by electron paramagnetic resonance in the Cu^{2+} impurities of a zinc fluosilicate crystal [9]. Figure 2.4 provides an illustration of this phenomenon, known as a Jahn-Teller distortion. Although it won't be discussed in detail here, the experienced reader may recognize the analogy of this type of distortion to that predicted by Peierl's theorem, which states that a 1-D chain of 1 electron atoms will distort to form alternating short and long bonds in order to achieve a lower ground state energy.

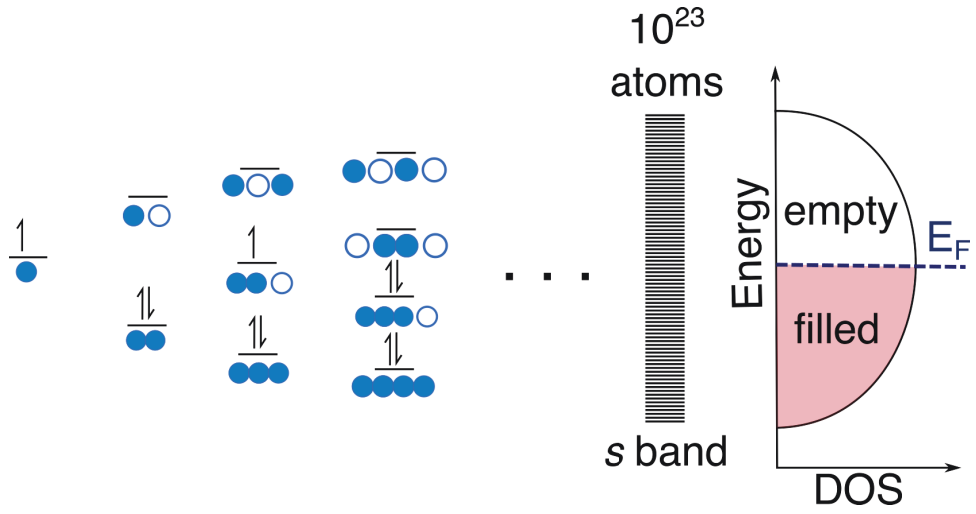

Figure 2.5: Overlap between the *s* orbitals of two adjacent atoms gives rise to a bonding and antibonding molecular orbital, and the two electrons of each isolated atom fill into the lowest energy orbital. Addition of a third atom creates an additional molecular orbital, and the third electron goes into the middle orbital. As the number of atoms is increased, the number of molecular orbitals increases. When a large number of atoms are bonded together, as is the case in macroscopic solids which have on the order of 10^{23} atoms, it is convenient to view the collection of bonding and anti bonding orbitals as a "band" of *s* states, or an *s* band. A density of states diagram shows how the electronic states are distributed in energy. In this particular case, each atom contributes one electron and one *s* orbital, so the resulting *s* band is exactly half-filled, as indicated by the shaded region in the density of states diagram. The energy of the highest occupied state at $T = 0$ K is called the Fermi energy E_F.

2.4 Bonding In Extended Solids

Thus far in this introduction we have only considered bonding interactions between a few atoms in order to develop an understanding of the electronic and magnetic structure of isolated complexes. This is far cry from the situation in solids, where the number of atoms is often on the order of Avogadro's number (10^{23}), and at such a large scale it is not instructive to consider discrete bonds and electrons. Figure 2.5 illustrates how increasing the length of an atomic chain leads to a large, densely packed collection of electronic states known as a *band*. A plot of the number of available electronic states at a given energy is known as a *density of states* diagram.

2.5 Electronic Conduction in Solids

As was the case in the isolated complexes considered in the previous section, the number of electrons in a particular band have a profound effect on the physical properties of a solid. At absolute zero, all electrons in a solid must fill the lowest energy available states, and the energy of the highest occupied state is known as the *Fermi energy* E_F. This is not to be confused with the Fermi *level*, which describes the statistical distribution of electrons in a band at finite temperature. The density of states at E_F determines the electrical conductivity of a material. In particular, the ability of a valence electron to move between states at low energetic cost is the primary factor that determines whether a material will be a good conductor of electricity. We can therefore classify a material as a good conductor (*metal*), a *semiconductor*, or a poor conductor (*insulator*), simple by looking at how the electrons in the system fill the density of states diagram, i.e. the density of states at E_F.

Figure 2.6 illustrates how band filling gives rise to each of the three basic types of electronic conductivity: metallic, semiconducting, and insulating. When a band is partially filled, there is a non-zero density of states at E_F, and the electrons can therefore move through the solid freely. In this *metallic* regime, the electrical conductivity is primarily limited by the vibrations of the underlying lattice (*phonons*) and defects, with which electrons

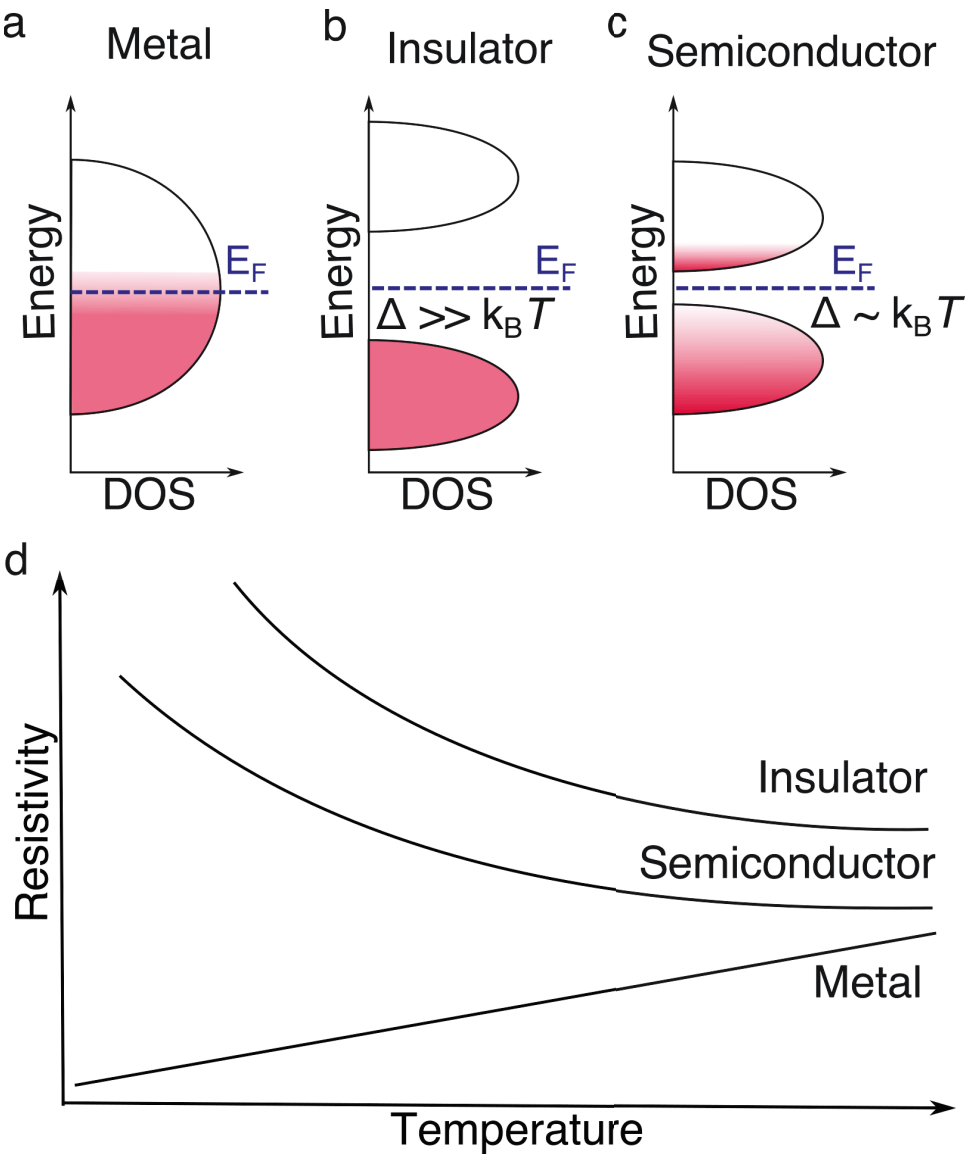

Figure 2.6: The electrical conductivity of a solid can be determined by examining the density of states (DOS) at the Fermi energy E_F. **a)** Materials that have a nonzero density of states at E_F will exhibit metallic electronic conduction, as is shown in the first plot. When the DOS at E_F is zero, the material will exhibit either insulating or semiconducting behavior, depending on the energy difference Δ between the highest occupied band (the valence band) and the lowest unoccupied band (the conduction band), known as the band gap. If Δ is much greater than the thermal energy $k_B T$, the material will not conduct electricity well and is said to be an insulator (**b**). If, however, $\Delta \leq k_B T$, thermal excitation of electrons from the valence band to the conduction band will allow for the material to exhibit semiconducting behavior (**c**). **d)** The basic trends in electrical resistivity as a function of temperature for each of the three cases outlined above.

collide. Lattice vibrations increase as temperature increases, so *the electrical conductivity of a metal decreases as temperature increases*. When a band is completely filled, E_F lies between the filled band and the next lowest energy band. In this scenario, the filled band is referred to as the *valance band*, the empty band is referred to as the *conduction band*, and the energy gap between the two is known as the *band gap*. When the band gap is small, valence electrons with sufficient thermal energy can jump into the conduction band and move freely amongst the available states. This is known as *semiconducting* behavior, because the material relies on outside energy to conduct electricity. When the band gap is large, there are essentially no electrons with enough energy to make the jump into the next band, and therefore the solid cannot conduct electricity. This is known as insulating behavior because the material cannot conduct electricity even when a large amount of energy is put into the system. Because the amount of energy available to a valence electron increases with temperature, *the electrical conductivities of insulators and semiconductors increase with temperature*. Figure 2.6(d) shows the trends in conductivity as a function of temperature for metals, semiconductors, and insulators.

While metallic conduction can always be traced to a finite density of states at E_F, the origin of insulating and semiconducting behavior can often be unclear. This is because there are numerous energy scales at play in solids that can give rise to a gap in the density of states of the conduction band and lead to insulating or semiconducting behavior. A particularly interesting type of insulating state occurs when a band is half-filled. In this case, the repulsive interaction between electrons, called the *Hubbard U* becomes extremely important, and causes a gap to open in the density of states [10]. Figure 2.7(a) illustrates how Hubbard U opens a gap in a half-filled band. When U is small, the lowest energy excited state is between the lower Hubbard band and the upper Hubbard band, i.e. the two halves of the band that was split by U–materials in which this occurs are referred to as Mott insulators (figure 2.7(b)) [11]. When U is large, however, the lower Hubbard band can be lower in energy than the highest energy state in the valence band, and in

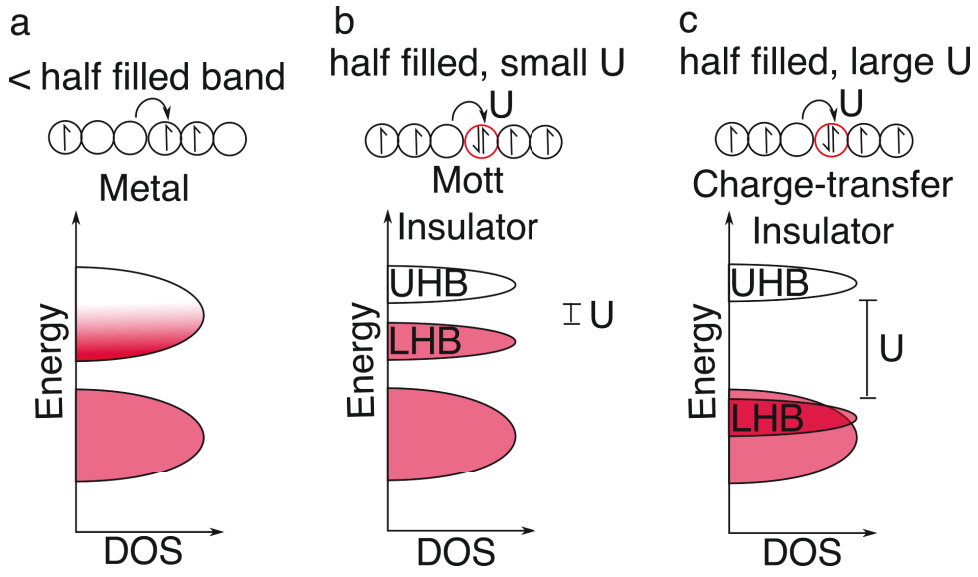

Figure 2.7: **a)** A partially filled band exhibits metallic conduction. **b)** A special case occurs when the band is half-filled, as electron-electron repulsion (Hubbard U) creates a pairing energy that opens a gap in the density of states. When this gap is small, the lowest energy excitation is between electrons in the lower Hubbard band (LHB) and the upper Hubbard band (UHB). **c)** When U is large, the LHB can be forced below the highest energy state in the valence band. In this case, the lowest energy electronic excitation is between the valence band, which is primarily ligand in character, and the UHB, which is primarily metal in character. Because this requires transfer of charge from the ligand to the metal, this scenario is called a charge transfer insulator.

this case the lowest energy excitation is between the valence band and the upper Hubbard band (figure 2.7(c)). This distinction is especially important for systems in which metallic and even superconducting behavior can emerge upon addition or withdrawal of electrons from the system (electron or hole-doping) [12]. Hubbard U, depicted in figure 2.7, is a particularly dominant energy in transition metal oxides, where strong covalent bonds between metal and oxygen force localization of non-bonding d electrons and conduction electrons are confined to narrow bands that are subject to strong electronic correlations. Thus transition metal oxides are almost always poor conductors of electricity. For these same reasons, however, transition metal oxides exhibit a wide variety of interesting and useful magnetic phenomena, as will be discussed in the following section.

2.6 Magnetism in Solids

As in isolated complexes, the presence of unpaired electrons in a solid causes a solid to interact with external magnetic fields. The main difference is that in solids the unpaired spins can have strong interactions with one another and will often spontaneously and order themselves either parallel (ferromagnetic) or antiparellel (antiferromagnetic) in order to obey the Pauli exclusion principle. The interaction between free spins in a solid is referred to as *exchange* and is parameterized by the exchange constant J. magnetic exchange can occur through four main pathways: 1) *direct exchange*, in which unpaired spins on different atoms interact with one another through direct orbital overlap; 2) *superexchange*, in which the unpaired electrons interact through bonds to a third mediator atom; 3) *indirect exchange*, in which unpaired spins interact with one another through delocalized conduction electrons, and 4) dipole-dipole interaction between the small magnetic field generated by each spin. In insulating oxides there are no conduction electrons, so only the first two types of exchange are possible. In general, the dominant magnetic interaction in a material determines the type of magnetic order present at low temperatures (close to absolute zero). The main types of magnetic order are *ferromagnetism*, where all spins point in the same

direction and the material exhibits a net magnetization, *antiferromagnetism*, where spins align opposite to their neighbors and the material exhibits no net magnetization, and *ferrimagnetism*, where spins align opposite to their neighbors but the magnitude of neighboring spins are different and the material exhibits a net magnetization. When thermal energy is sufficient to overcome spin–spin interactions, all materials exhibit *paramagnetism* where interactions between neighboring spins are present but are not strong enough to cause the spins to order. The rules regarding magnetic exchange in transition metal oxides were pioneered by Goodenough and Kanamori in the mid to late 1950's and do a remarkably good job of describing the magnetism observed in many transition metal oxides [19–21]. Figure 2.8(a and b) shows common spin-spin interaction pathways in transition metal oxides and several types of magnetic order than can result from these interactions. Direct d-d overlap between neighboring transition metals leads to antiferromagnetic (antiparallel spin alignment) exchange. Superexchange between adjacent metal sites can occur *via* the fully-occupied oxygen 2p orbitals. In the superexchange case, the geometry of the exchange pathway determines the sign of the exchange constant. When the metal-oxygen-metal (M–O–M) bond angle is 180°, magnetic exchange occurs through a single oxygen 2p orbital and the resulting metal–metal interaction will be strong and antiferromagnetic in accordance with the Pauli exclusion principle. When the M–O–M bond angle is 90°, the exchange pathway is through two separate, orthogonal oxygen 2p orbitals, which exhibit only a weak Coulombic interaction that favors maximum spin multiplicity. This results in a ferromagnetic exchange constant $J > 0$ between the two metal centers.

Ferromagntism, antiferromagnetism and paramagnetism all have distinct experimental signatures that can be observed by measuring the magnetization induced in a material by a magnetic field. A common example of such an experiment is holding a material near a known ferromagnet. If the material is strongly attracted or repelled, then the material is clearly ferromagnetic. More quantitatively, the type of magnetic interactions present in a material (or lack thereof) can be determined by measuring the material's *magnetic*

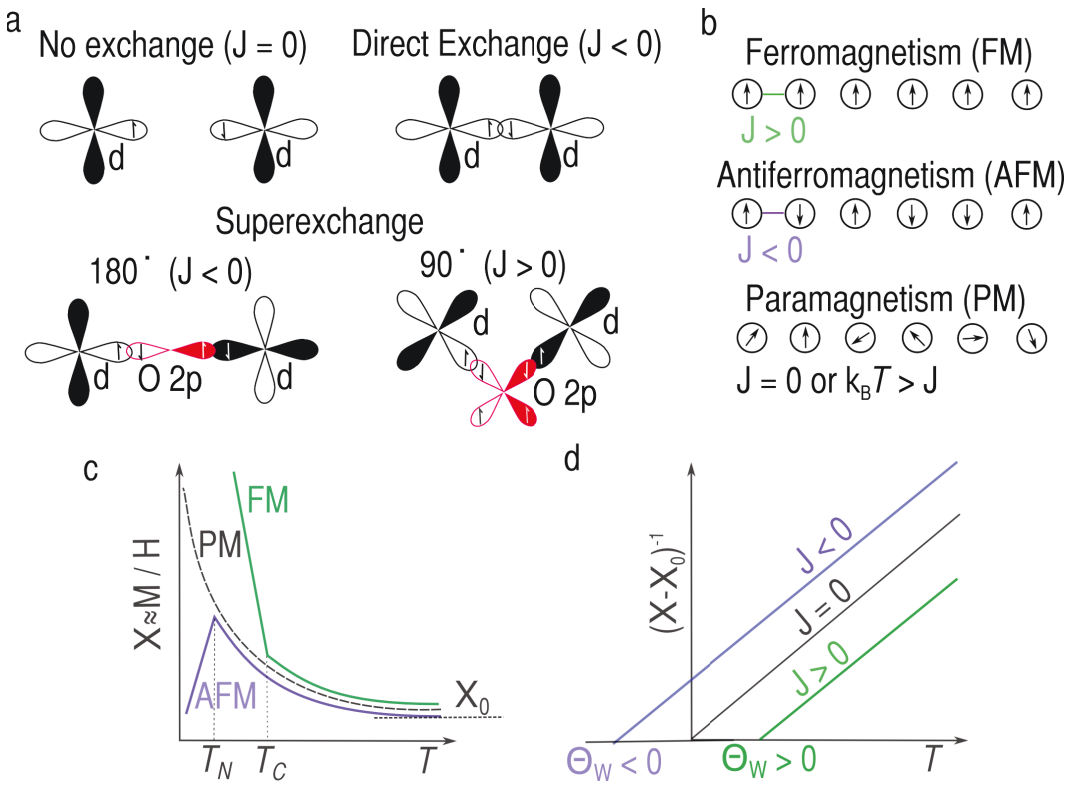

Figure 2.8: **a)** Common types of magnetic exchange in insulating $S = \frac{1}{2}$ transition metal oxides. The sign and magnitude of J indicates whether antiferromagnetic ($J < 0$) or ferromagnetic ($J > 0$) exchange interactions dominate between localized spins. If there are no interactions between spins, J = 0. **b)** The value of J determines the type of magnetic order observed in the system. When thermal energy $k_B T$ is greater than the value of J, all systems are in the paramagnetic state and exhibit Curie-Weiss behavior. **c)** Magnetic susceptibility data can distinguish between the different types of magnetic order. The temperatures below which antiferromagnetic or ferromagnetic order develops are called the Néel temperature T_N and the Curie temperature T_C, respectively. **d)** A plot of the inverse magnetic susceptibility versus temperature will be linear for a material in the paramagnetic regime. The slope and intercept of the line yield the Curie constant C and the Weiss temperature θ.

susceptibility χ. The magnetic susceptibility of a material is defined as the derivative of magnetization with respect to the magnitude of the applied magnetic field:

$$\chi = \frac{dM}{dH}, \tag{1}$$

where M is the magnetization is the applied magnetic field H. In practice, χ is often approximated as $\chi \approx M/H$ so that the applied magnetic field can be kept at a constant strength while varying the temperature of the material. For a perfectly paramagnetic material in which free spins are completely independent (J = 0), the susceptibility follows the Curie law:

$$\chi = \frac{C}{T}. \tag{2}$$

When the susceptibility is normalized by the molar quantity of the material, the Curie constant is related to the effective magnetic moment μ_{eff} of the magnetic ion by:

$$C = (\frac{\mu_{eff}}{8})^2 \tag{3}$$

and has units of $\frac{emu \times K}{mol \times Oe}$ in centimeter-gram-second (CGS) units. The ideal value of μ is related to the spin and angular momentum quantum numbers of the magnetic ion by:

$$\mu_{S+L} = \sqrt{4S(S+1) + L(L+1)}. \tag{4}$$

This expression is valid for an unperturbed free ion, where both the spin and angular momenta of the unpaired electrons contribute to the net magnetic moment. In solids the orbital angular momentum L is quenched by crystal field interactions, and the magnetic moment is better described by considering only the spin component:

$$\mu_{S+L} = g\sqrt{S(S+1)}. \tag{5}$$

where g is the gyromagnetic ratio for a free electron, and is roughly equal to 2.0. Magnetic ions in solids often interact with one another ($J \neq 0$), which causes the susceptibility to deviate from ideal Curie behavior. This deviation is described by the Curie-Weiss law:

$$\chi = \frac{C}{T - \theta_W} + \chi_0, \tag{6}$$

where C is the Curie constant, θ_W is the Weiss temperature, and χ_0 is a temperature independent correction. In all materials, when the thermal energy k_BT exceeds the magnetic interaction magnetic coupling energy J, the spins cannot order due to thermal fluctuations and the system will follow the Curie-Weiss law. The Weiss temperature θ_W is a measure of the net magnetic interactions present in the material; a negative Weiss temperature means that antiferromagnetic interactions dominate in the material, while a positive value indicates dominant ferromagnetic interactions. Thus the average magnetic moment of the metal ions in a material, as well as the magnitude and sign of the exchange interactions between metal sites, can be determined experimentally. Figure 2.8(c) shows the general trend in magnetic susceptibility as a function of temperature for ferromagnetic, antiferromagnetic, and paramagnetic systems. At high temperatures when a material is forced into the paramagnetic regime, a plot of the inverse magnetic susceptibility will be linear. By performing a simple algebraic rearrangement, the Curie-Weiss law can be linearized for straightforward calculation of the Curie constant and the Weiss temperature by least-squares fitting:

$$\frac{1}{\chi - \chi_0} = \frac{T}{C} - \frac{\theta_W}{C}. \tag{7}$$

2.6.1 Spin–Orbit Coupling

Thus far, three major factors have been discussed that have profound effects over the magnetic and electronic properties of solids: The crystal field, Jahn-Teller effects, and the Hubbard U. The energy scales associated with each of these factors are large for small

atoms, but U becomes smaller when moving down the periodic table due to the increasingly diffuse nature of the valence d-orbitals. It has been taken for granted that the spin and orbital angular momenta of an electron are independent of one another, which for light atoms is a valid assumption. However, as the nuclear charge of an electron's parent atom increases, so too must its orbital velocity around the nucleus, and the increase in orbital velocity means that the electron's orbit produces a significant magnetic field with which its spin interacts. This phenomenon is known as *spin-orbit coupling* (SOC), and is particularly strong for transition metals in rows 6 and below, where the f electrons do an exceptionally poor job of shielding the valence d electrons from nuclear charge. In these heavy transition metals, SOC can result in a significant reordering of orbital energies and ultimately change the magnetic and electronic properties of the complex. As will be shown in chapters 3 and 4, SOC has a significant influence on the magnetic properties of iridium oxides.

2.7 Synthesis

The energetic stability of a chemical system can be quantified by a single number called the Gibbs energy G, which is an energy related to the total bond enthalpy H, the entropy S, and temperature T as:

$$G = H - TS. \tag{8}$$

For systems in which multiple phases exist, the phase with the lowest Gibbs energy is the most energetically favorable phase, and the system may undergo a chemical reaction or phase transition to achieve the lowest energy phase. The amount of energy lost in the transition between two phases with different Gibbs energies is the Gibbs free energy ΔG:

$$\Delta G = \Delta H - T\Delta S. \tag{9}$$

Thus for a particular set of reactants, the reaction pathway that produces the largest negative value of ΔG will be the most exothermic and therefore yield the most thermodynamically

stable products. In this case, the lowest energy product (the *thermodynamic products*) are attained *via thermodynamic control*. However, a large value of ΔG does not necessarily mean that a particular reaction will take place. On the contrary, it is often the *activation energy* E_a of the reaction pathway that governs its likelihood of occurring. Therefore it is possible to guide a reaction toward a less thermodynamically stable product by controlling the amount of energy available to the system, and in the second case the reaction with the lowest activation energy yields products with higher overall energy. Controlling a reaction in this way is called *kinetic control*, and the product is referred to as the *kinetic product*. Figure 2.9 shows an example of a chemical system with two different possible reaction pathways. By controlling the temperature of this system, one can direct the system to either the thermodynamic product or the kinetic product.

The *reaction rate* is governed by the kinetic degrees of freedom of the reactants. In liquid and solution phase reactions, molecules have full translational and rotational freedom, and for two molecules to react they must collide in the appropriate orientation and with sufficient energy to create an *activated complex*. When two reactants finally collide properly, the reaction proceeds rapidly to completion. Thus the rate-limiting step in solution-phase and gas-phase reactions is often the formation of the activated complex. Solid state reactions present a completely different situation because vibrations are the only kinetic degrees of freedom. In this case, the only pathway by which two solids can react with one another is *diffusion*: the gradual, random drift of atoms in a solid driven by thermal vibrations. Solids are thus relatively inert in comparison to liquids and gasses.

One obvious solution to the problem of solid state reactivity is simply to melt the reactant elements together, and this is indeed possible for many systems–welding is an excellent example of a melting synthesis. This solution fails, however, for systems which have very high melting points, or decompose before melting. This is the case for many oxides, and thus melting is not an option for these systems. An effective but slower alternative to melting is known as the solid-state synthesis, or "shake n' bake" synthesis, in which reactant

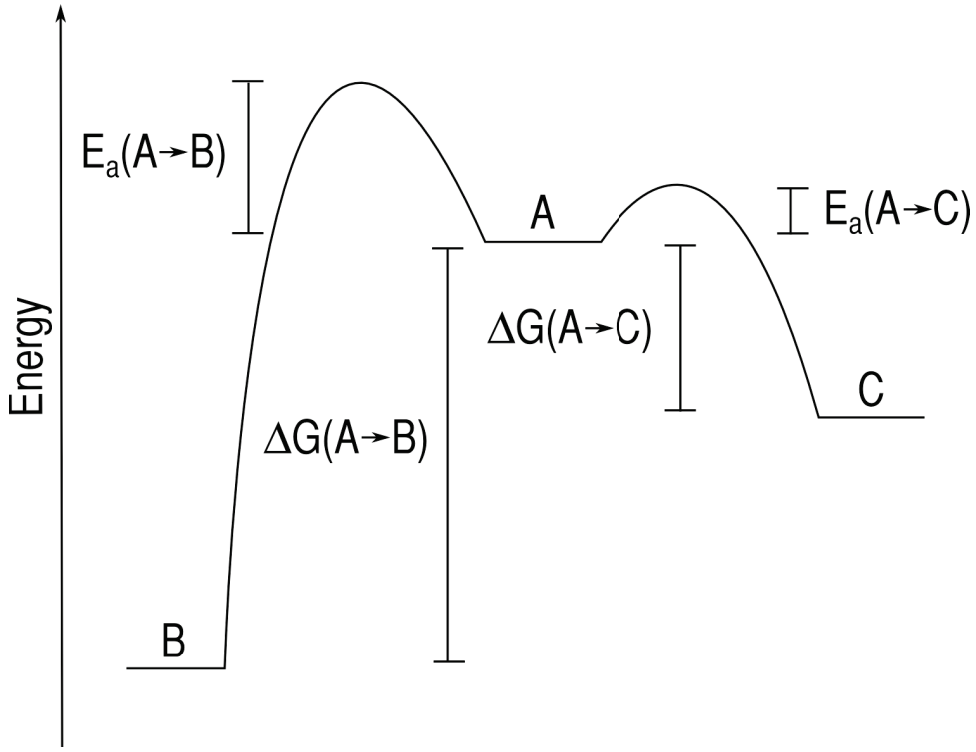

Figure 2.9: Two possible reaction pathways for a chemical system A are shown with energy on the y-axis. ΔG is largest for the reaction A$\rightarrow$B and therefore B is the thermodynamic product. In contrast, the reaction A$\rightarrow$C is less exothermic (smaller ΔG) but also has a smaller activation energy E_a. Thus at low temperatures ($E_a(A\rightarrow B) >> k_B T > E_a(A\rightarrow C)$), product C will be preferentially obtained. C is therefore called the kinetic product.

solids are thoroughly mixed and then heated together at a temperature high enough to force significant diffusion. This is by far the most common approach for producing transition metal oxide compounds, and has yielded countless breakthrough materials including many high-T_C copper oxide superconductors[1].

The high temperatures required for solid state synthesis can introduce substantial numbers of chemical and structural defects into the product of interest, as defect formation produces a significant entropic gain at high temperatures. To illustrate this concept, consider the synthetic procedure for Na_2IrO_3, which is one of the honeycomb iridium oxide discussed in future sections. The first reported synthesis for this compound requires combining 1 molar equivalent of sodium carbonate (Na_2CO_3) with a single molar equivalent of either iridium oxide (IrO_2) or iridium metal and heating the mixture at 900°C:

$$Na_2CO_3 + IrO_2 \longrightarrow Na_2IrO_3 + CO_2. \tag{10}$$

Sodium ions can also be lost to vaporization as Na_2O, a decomposition product of Na_2CO_3, and the vapor pressure of the Na_2O results in a sodium vacancy defect equilibrium:

$$Na_2IrO_3 \longrightarrow Na_{2-x}IrO_3 + xNa^+, \tag{11}$$

At a given temperature, the equilibrium number of defects can be estimated from the enthalpy and entropy associated with formation of a single defect, i.e. from the Gibbs free energy change:

$$\Delta G_{defect} = \Delta H_{defect} - T\Delta S_{defect}, \tag{12}$$

where ΔH_{defect} can be estimated from the electrostatic potential of an Na^+ ion in a octahedral cage of 6 oxygen atoms and ΔS can be estimated from the number of possible locations in the crystal at which the defect can occur:

$$\Delta S = k_B \, ln \, \omega. \tag{13}$$

Here, ω is the number of sodium sites in the entire crystal. Even for small samples, this number will be on the order of 10^{20}, and therefore the entropic gain for introducing a single sodium vacancy defect is quite large. At 900°C, one can expect a sodium ion defect concentration on the order of 5 percent of the total number of sodium sites. One can reduce the number of defects by adding an excess of sodium carbonate. LeChatalier's principle dictates that this will suppress the defect equilibrium, thereby shifting the thermodynamic defects curve in Figure 2.12 slightly to the right. This approach, coupled with a slightly lower synthesis temperature of 800°C to suppress Na_2O vaporization, results in a significantly lower sodium ion vacancy defect concentration in Na_2IrO_3[51].

Figure 2.10 shows a graphical illustration of the enthalpic and entropic energies associated with defect formation. In the thermodynamic limit, the equilibrium number of defects is determined by the minimum in the ΔG curve, and defect concentrations can be increased substantially by changing the thermodynamic driving force for defect formation. This is the goal of a large class of heterogeneous solid state reactions referred to as soft chemistry or "*chimie douce*." In chapters 4 and 5, a sodium ion vacancy defect concentration of 50% is produced in Na_2IrO_3:

$$Na_2IrO_3 \longrightarrow NaIrO_3 + Na^+. \tag{14}$$

This is accomplished through the use of a strong oxidant, namely iodine or bromine, which provides an electrochemical driving force for sodium ion removal. This process can be described by two separate oxidation and reduction half reactions:

$$Ir^{4+} \longrightarrow Ir^{5+} + e^- \ (ox) \tag{15}$$

$$2Na^+ + 2e^- + X_2 \longrightarrow 2NaX \ (red). \tag{16}$$

This reaction can be carried out in solution at room temperature with the oxidant in solution, and the product $NaIrO_3$ is stable on the benchtop at room temperature, even after the excess oxidant and side products have been removed. It is interesting to note, however, that

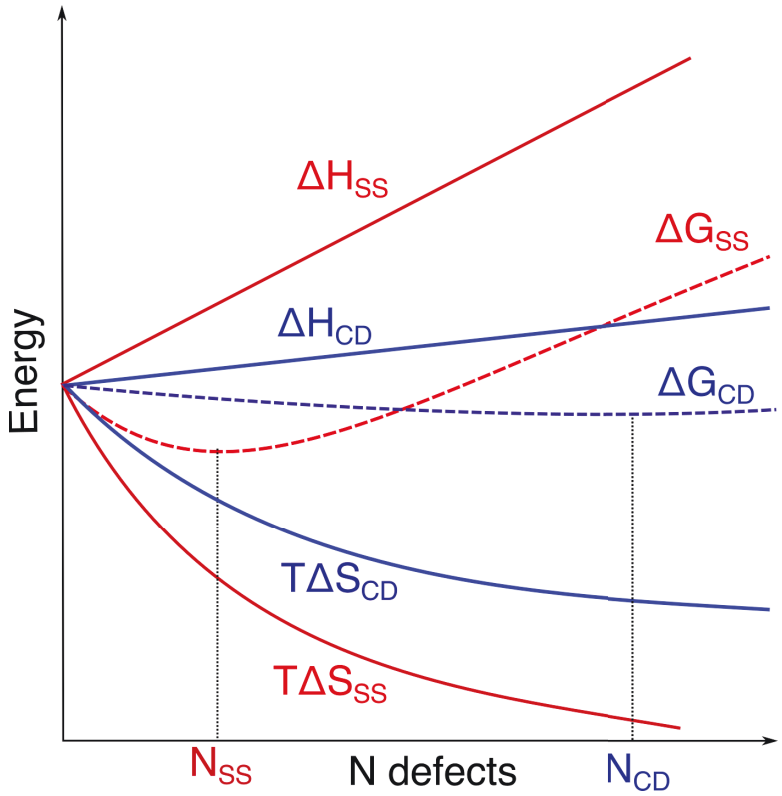

Figure 2.10: Formation of defects in a crystal is enthalpically costly but entropically favorable, and the number of defects in a crystal at equilibrium is determined by the Gibbs free energy change associated with defect formation. Conventional solid state synthesis (SS) produces a finite number of defects (N_{SS}) that is determined by the minimum of the ΔG curve. Higher or lower defect concentrations can be obtained by changing the thermodynamic driving force, i.e. changing the reactants, as is the case in *chimie douce* (CD) techniques, which often take place at much lower temperatures. This lowers the total enthalpic cost for the defect formation while maintaining a large entropic gain, thus resulting in a greater number of defects at equilibrium (N_{CD}) .

the product $NaIrO_3$ decomposes into at least two phases upon heating in air at modest temperatures of a few hundred Celsius. Though this decomposition has not been investigated in detail, it is likely that $NaIrO_3$ decomposes into the original Na_2IrO_3 phase and iridium oxide species:

$$2NaIrO_3 \longrightarrow Na_2IrO_3 + IrO_2 + \frac{1}{2}O_2. \tag{17}$$

There are two possible explanations for the stability of $NaIrO_3$ at room temperature that are illustrated in figure 2.11. The first possibility is that $NaIrO_3$ is indeed the thermodynamic product at low temperatures, and the decomposition products become more stable at higher temperatures. The second possibility is that $NaIrO_3$ is **not** the thermodynamic product at low temperatures, and is only obtained due to the large activation barrier for the phase separation to Na_2IrO_3 and IrO_2. In the latter case, $NaIrO_3$ is the kinetic product, and is therefore *metastable* at low temperatures. The kinetics associated with the first step in this reaction ($Na_2IrO_3 \longrightarrow NaIrO_3$), explored in depth in chapter 5, lead to the rather striking conclusion that the rate-limiting step (which determines the activation energy E_a1) is not diffusion in the solid at temperatures above 0^oC.

This tradeoff between kinetic and thermodynamic control can be generalized for a particular chemical process by considering how each of the two factors vary as a function of temperature. Figure 2.12 shows a plot of defect concentration versus temperature normalized by energy-per-defect to illustrate the effect of temperature of the equilibrium defect concentration. The kinetic component of this plot is large at low temperatures, while at high temperatures the defect concentration is determined by the thermodynamics of the defect (ΔG), and the sum of these two curves determines the equilibrium number of defects at a given temperature. One can therefore obtain kinetic or thermodynamic control over defect concentration by controlling temperature.

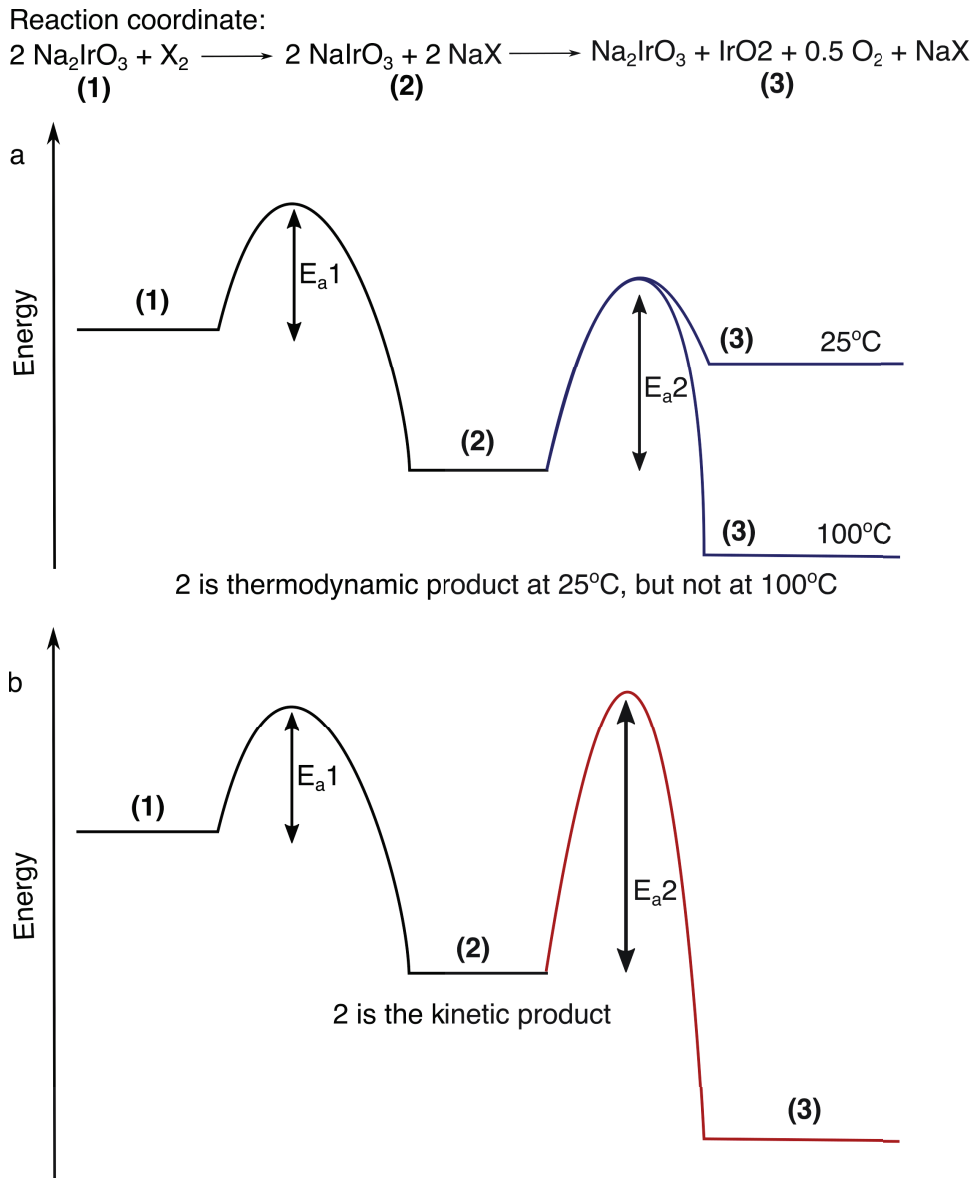

Figure 2.11: A reaction coordinate diagram shows the energies of phases **1**, **2** and **3**, with activation energies E_a1 and E_a2. This plot shows two possible reasons for the stability of $NaIrO_3$ at room temperature. **a)** At $T = 25^oC$ **2** is the thermodynamically stable phase, and heating to higher temperatures causes phase **3** to be lower in energy. Thus at low temperatures **2** will be obtained as the thermodynamic product. **b)** Phase **3** is the most thermodynamically stable, but the activation energy required to produce **3** from **2** is greater that the available thermal energy at 25^oC. **2** is obtained at low temperatures but will decompose to produce **3** when $k_BT > E_a1$, and therefore **2** is referred to as the kinetic product in this case.

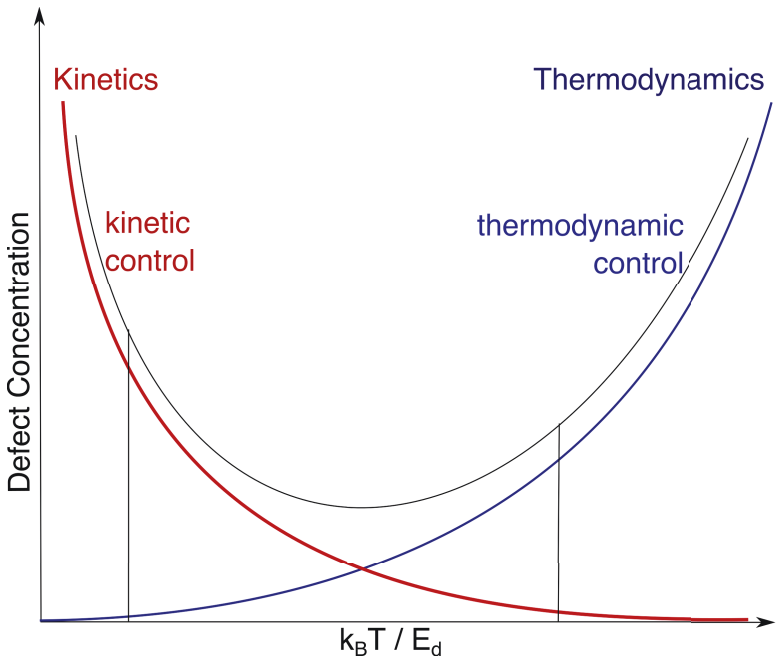

Figure 2.12: A qualitative plot of defect concentration as a function of thermal energy k_BT normalized by energy per defect E_d. In the high temperature limit the thermodynamics govern the defect concentration and the equilibrium number of defects is determined by the minimum of ΔG, while in the low-temperature limit the number of defects produced by a chemical reaction is determined by the kinetics of the defect formation. One can thus use temperature as a knob with which to tune defect concentration in both equilibrium and non-equilibrium regimes.

2.8 Structural Characterization

The ability of an atom to scatter radiation forms the basis for most structural characterization. The scattering of radiation by an atom can be roughly described by two functions: the *form factor* and the *cross section*. The form factor depends on the radiation type, and describes the amplitude of the scattered wave as a function of angle from the incident radiation vector. X-ray and electron radiation are similar in that they are scattered strongly by the electron cloud of an atom, and therefore they have similar form factors: the form factor X-rays or electrons wave is greatest for scattering at 0° from the incident beam and decreases to a minimum at 180°. In contrast, neutrons do not interact with the electron cloud and are instead scattered by the atom's nucleus. Neutrons essentially do not have a form factor, and scattering of a neutron by an atom can therefore by assumed to be independent of angle. The cross section depends on the atom off of which the radiation is scattered, and describes the likelihood that radiation will be scattered from that atom. The cross section for X-rays and electrons increases as a function of atomic number, since the number of electrons per atom increases with atomic number. The cross section for neutrons is a function of the internal structure of the nucleus and has no consistent trend with atomic number. The net result of this information is that X-rays, electrons and neutrons all provide complimentary information about the periodic structure and chemical makeup of a material. X-rays are the most commonly utilized radiation due to the relative ease with which they can be produced, monochromated, guided and detected, while experiments involving electrons and neutrons require more specialized equipment and expertise.

Because individual atoms follow strict rules with regard to the bonds they form, extended solids are generally comprised of repeating units that are well ordered in a periodic fashion. In 1912, Max von Laue and colleagues demonstrated that when high energy electromagnetic radiation (X-rays) is directed onto a crystalline solid, the radiation is reemitted in an ordered pattern that is related to the internal periodic structure of the material. Two years after his work on this topic was published, Laue was awarded the Nobel prize in

physics for his discovery of X-ray *diffraction*. In practice, diffraction techniques are distinguished by the type of radiation they employ and the geometry of the sample they probe. The most common types of radiation used in diffraction experiments are X-rays, electrons, and neutrons because they can be reliably produced with wavelengths on the scale of interatomic spacings in solids.

The work presented in this text was made possible by frequent use of X-ray and neutron diffraction, and these two techniques will be now be discussed in more detail. Figure 2.13(a, b) shows how focused beam of monochromatic (single wavelength) radiation with wavelength λ scatters off of two particles separated by a distance d. In the two particle case, incident radiation is scattered off of each particle in a diffuse pattern with the same wavelength as the incident radiation. The waves scattered from each particle exhibit constructive and destructive interference at different angles with respect to the incident beam path. At angles where constructive interference occurs the scattered wave is amplified, while at angles where destructive interference occurs the wave is attenuated to zero amplitude. The resulting pattern of amplification and attenuation is known as the *diffraction pattern*, which depends solely on the spacing between the two particles and the wavelength of the incident radiation. This means that the space between the two particles can be directly determined based on the wavelength of the incident radiation and the angles at which constructive interference is observed. The theory of diffraction was pioneered by a famous father son duo, William Henry and William Lawrence Bragg [13]. Bragg's Law states that the wavelength of the incident radiation is related to the d-spacing and the diffracted angle by the following equation:

$$n\lambda = 2dsin(\theta), \tag{18}$$

where λ is the wavelength, d is the d-spacing, and θ is the diffracted angle.

In extended solids, diffraction occurs from parallel planes of atoms, and the characteristic diffraction pattern of a material can be used to identify its structure. The smallest repeating geometrical unit in a particular solid is known as its *unit cell*, and in 3 dimensions

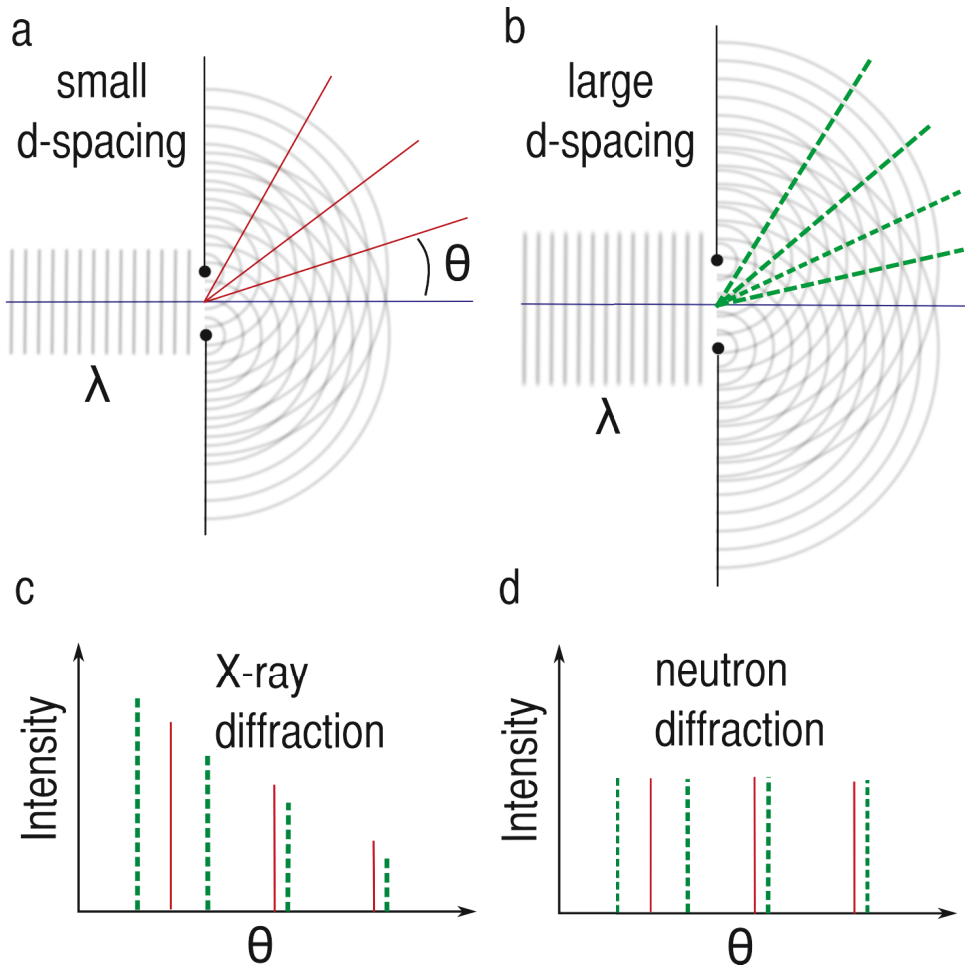

Figure 2.13: a) Monocromatic, collimated radiation with wavelength λ is scattered off of two particles separated by a distance d. The waves scattered by the two particles interfere with one another, giving rise to a pattern of amplification and attenuation, indicated by red lines. **b)** Increasing the distance between the two particles results in additional regions of constructive overlap, shown as green lines. The angles at which the scattered radiation is amplified are related to the wavelength of the incident radiation and the inter-particle d-spacing by Bragg's law: $n\lambda = 2d\sin(\theta)$. **c, d)** The observed amplitude (*intensity*) of the scattered wave is plotted as a function of angle for the two d-spacings shown in parts a and b. When X-rays are the radiation emplyed, the observed intensity decreases as a function of angle due to the X-ray scattering form factor. In contrast, when neutrons are the radiation of choice the observed intensity is not a function of the diffraction angle, as neutrons have an isotropic scattering form factor.

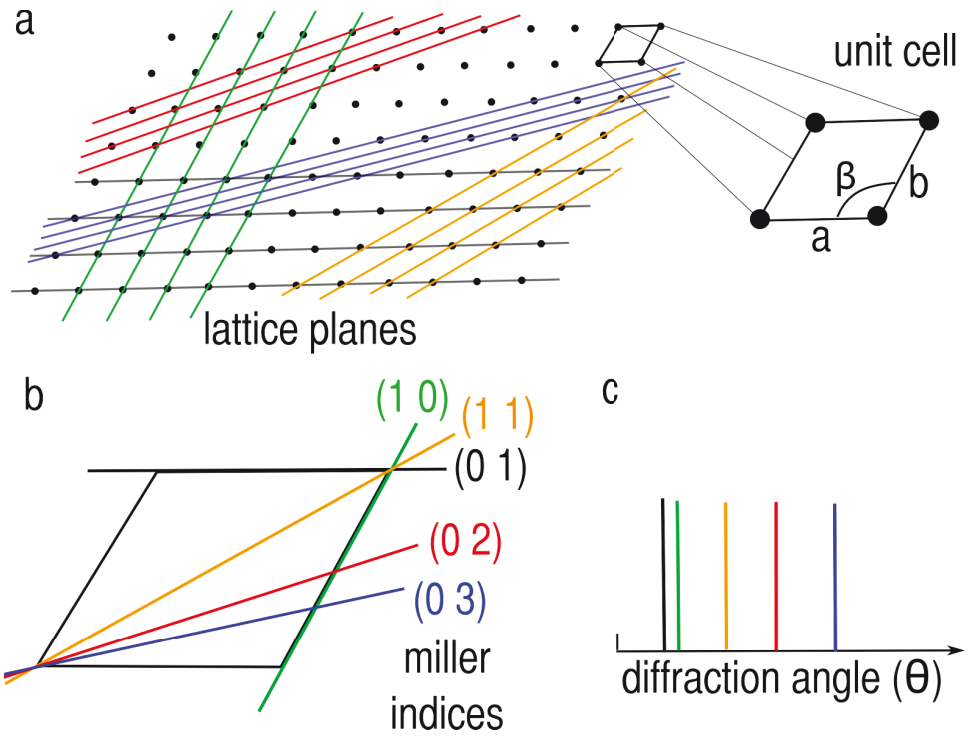

Figure 2.14: a) A 2 dimensional lattice of points is shown along with its unit cell and several collections of lattice planes. **b** The lattice planes highlighted in part a are distinguished by their Miller indices, which are determined by where they intersect the edges of the unit cell. **c)** Each unique set of planes produces its own set of diffraction peaks, and the angle at which each collection of planes produces a diffraction peak is inversely related to the spacing between equivalent planes. In this case, the (0 1) planes have the largest spacing, and thus result in the lowest-angle diffraction peak.

there are a total of 7 different types of possible unit cells, called crystal systems, that can be used to characterize nearly all types of crystalline solids[52]. Figure 2.14(a) shows a simple example of a 2-dimensional lattice of identical atoms. Diffraction of monochromatic radiation from a 2 dimensional lattice gives a distinct pattern of peaks in one dimension (θ), which result from constructive interference between waves scattered from geometrically equivalent planes of atoms. Note that sets of lattice planes that are closely spaced give rise to diffraction peaks at high angles, whereas planes with large spacing yield peaks at low angles. This inverse relationship between d-spacing and diffraction angle is a result of the fact that the diffraction pattern is related to the periodicity of the lattice by a Fourier transform. While this concept is crucial to an in-depth understanding of diffraction phenomena, it is possible to develop an intuitive understanding of crystallography without knowledge of the mathematics. For a more deeper introduction to diffraction, B. E. Warren provides a thorough but approachable summary of X-ray diffraction physics [14].

Determining a material's crystal structure can be accomplished in two primary ways that are distinguished by the geometry of the sample of interest. Just as different types of radiation offer complementary information about a material's atomic composition, diffraction from single crystals provides information that can be complementary to diffraction from well ground powders, and *vice versa*. Diffraction experiments using single crystals can be a convenient method of determining a material's structure because they eliminate many extrinsic factors that make analysis of the diffraction pattern difficult. However, single crystals can often be prohibitively difficult to synthesize, and diffraction experiments suffer from effects that are related to the crystal's shape and internal defects. Powder diffraction is the technique of choice in this work, as it allows new materials to be characterized rapidly without the need for difficult, time consuming crystal growths. However, because multiple Bragg planes can have the same d-spacing in a material and diffraction from these planes will produce overlapping peaks in the powder pattern, one cannot solve a crystal structure from powder diffraction data using direct methods.

In a powder diffraction experiment, the material of interest is thoroughly ground in order to achieve small particles with sizes on the order of a few hundred microns that are oriented in a perfectly random fashion, and monochromatic radiation is used to produce a diffraction pattern. When a perfectly isotropic distribution of particle sizes and orientations is achieved, the diffraction pattern produced by these particles represents every possible diffraction peak that can be produced by the unit cell of the material, and can be collected by simply recording the *intensity* of the diffracted wave as a function of *diffraction angle* θ from the incident radiation beam. The resulting data is commonly used to produce a plot of intensity versus diffraction angle θ, which is often written as 2θ based on the geometry of the instrument. Each peak in the plot corresponds to a diffraction from a particular set of lattice planes and will have some finite width that is inversely related to the particle size. When a single peak corresponding to a particular lattice plane is isolated, the height and width of the peak is directly related to several important parameters, a few of which are listed below:

- Peak multiplicity (how many times the plane occurs in the unit cell).
- Structure factor (how well the atoms in the plane scatter radiation).
- Temperature (lattice vibrations decrease peak intensity).
- Particle size (large particles produce sharper diffraction peaks).
- Interparticle strain (strain decreases peak intensity and changes peakshape).

Because the number of parameters affecting the width and height of a given peak is large, robust solution of even simple crystal structures from powder diffraction data was not possible until 1969, when Hugo Rietveld introduced a least-squares method of accounting for the observed powder diffraction data [15]. Using this method, known as *Rietveld refinement*, solution of crystal structures using powder diffraction is now common and widely accepted practice.

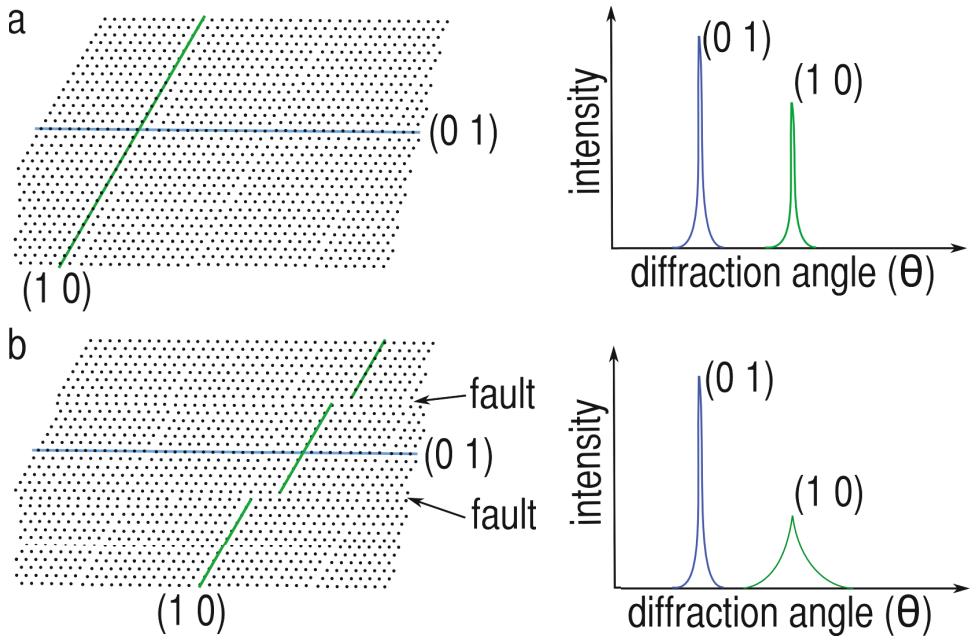

Figure 2.15: a) Diffraction from a particle of finite size results in peaks that are visibly broad, especially at their base. In this case, the particle size is roughly the same for the (0 1) planes and the (1, 0) planes, so the diffraction peaks corresponding to those lattice planes have similar widths. **b)** introduction of just two stacking faults in the (0 1) plane causes a drastic reduction in effective particle size for the (1 0) planes. The resulting diffraction pattern shows a sharp (0 1) peak and an unusually broad and short (1 0) peak.

Aside from the common types of chemical disorder discussed previously, several of the layered materials discussed in the following chapters exhibit a type of structural disorder that results from incorrect stacking of 2 dimensional honeycomb layers. This arises due to the fact that there are multiple ways in which a honeycomb layer can rest on top of another honeycomb layer without producing a significant difference in energy. While the lowest energy stacking arrangement generally dominates the structure as a whole, occasionally a *fault* will occur in which a single layer is stacked in one of the slightly higher energy arrangements. While this comes at small energetic cost, it effectively reduces the particle size for an entire collection of Bragg peaks. This large structural perturbation makes characterization *via* diffraction techniques difficult, as illustrated in Figure 2.15. This can be accounted for in practice by introducing a second or even third variable in the structural refinement to allow for direction-dependent broadening. Several Rietveld refinement software packages such as GSAS [16] and FullProf [17] have incorporated such a phenomenological treatment of stacking faults with varying degrees of success. DIFFaX provides a method of simulating stacking faults in periodic lattices, and can often provide a qualitative account of stacking disorder and fault concentration in a sample, as described in chapters 2 and 3 [18].

2.9 *in-situ* Solid–Liquid Reaction Kinetics

As described in section 2.7, control over the kinetics (i.e. rate) of a particular reaction can be a powerful method of producing new compounds that are not accessible using conventional solid state synthesis techniques. It is therefore important to understand what exactly governs the rate of a particular reaction, and what the activation energy associated with that particular step in the reaction mechanism is. Reaction kinetics are particularly important but poorly understood in heterogeneous solid-liquid reactions, which drive numerous important technologies. At the time of writing, lithium ion batteries power a substantial portion of the world's portable electronic devices. These batteries operate under the basic

principle of *deintercalation*, which can be described as the electrochemically driven removal of ions from a solid into an electrolyte. A great deal of research is currently targeted at improving the cycling (charge/discharge) rates, storage capacity, and durability of cathode materials for lithium and sodium ion batteries. Despite these efforts, little is known of the precise mechanism of charge transfer across the cathode/electrolyte interface. One possible reason for the lack of understanding of such an elementary reaction is that experiments in the field of deintercalation kinetics focus almost entirely on the cycling abilities of batteries, which by nature are affected by a large number of extrinsic factors. Recent works have used highly specialized techniques such as synchrotron X-ray imaging to probe the discharge mechanism in phase-separating materials, but have no way of definitely separating their results from the extrinsic effects of, the electrolyte solution or the binding material used to contact the cathode material.

In the final chapter, I present the results of a novel study on the rate of charge transfer across the solid–liquid interface in which extrinsic, potentially rate–limiting factors such as contact resistance and electrode binding materials are eliminated completely in favor of an oxidizing electrolyte solution. This work made use of the strong optical absorption bands of the solution phase oxidant to track the reaction progress *in-situ* using ultraviolet-visible (UV-Vis) absorption spectroscopy (UV-Vis).

In UV-Vis absorption spectroscopy, a light source is passed through a clear container called a *cuvette* containing a solution of a solute X in an otherwise optically transparent solvent. As light passes through the cuvette, light of particular wavelengths will be *absorbed* to generate excited states in the solution-phase species X, while light at other wavelengths will pass through the cuvette without loss in intensity. The intensity of light at a given wavelength λ that transmits through the cuvette P is measured, and this transmittance is compared to the transmittance in the absence of X, known as the blank transmittance P_0.

The logarithm of the ratio of these two values is called the *absorbance*:

$$A = log(\frac{P}{P_0}) \tag{19}$$

, and the collection of these values across a range of energies is known as the *absorption spectrum*. In the simplest case, the absorbance at a given wavelength A(λ) of a solution of X is related to the concentration of X, the molar absorptivity of X at a given wavelength $\varepsilon(\lambda$, and the path length ℓ by Beer's law:

$$A(\lambda) = [X]\varepsilon(\lambda)\ell \tag{20}$$

. Given the linear relationship between concentration and optical absorption, one can determine the concentration of X in an unknown solution by comparison to the absorbance of known solutions, i.e. by reference to a calibration line. Note that because absorbance is a logarithmic function of transmittance, values of absorbance above 1 correspond to extremely small amounts of transmitted light. A general rule was established in the early days of UV-Vis absorption spectroscopy that absorbance measurements above a value of 1 are not reliable for experimental reasons, however, with modern charge-couple device detectors and high intensity lamps, absorbance values of up to 3 can routinely be reported with reasonable certainty. In all cases, reference to an external calibration is important to determine the range over which absorption measurements are valid for a particular solution. In general, the concentrations of *n* light-absorbing species in solution can be determined by measuring the absorption spectrum at *n* different wavelengths if the absorption spectrum of each species is well characterized in isolation. Unfortunately this was not the case for the mixtures of halogens and sodium trihalide obtained in the final chapter, and a modified data analysis method was developed to accurately quantify both solution-phase species. This method makes use of the fact that a UV-Vis absorption spectrum can be modeled by a sum of an arbitrary number of Gaussian or Lorentzian peaks [22, 23]. The basic principle

and method by which this analysis was performed is detailed below and in Appendix A.

When the absorption spectrum of each species in isolation is not well-characterized, quantification of multiple species with overlapping absorption bands is difficult. This was the case in the work presented in chapter 5, where the reaction between halogen species X_2 and sodium halide NaX was found to produce a trihalide species NaX_3, which produces very strong near-UV absorption that cannot be isolated in the absence of X_2. This solution-phase equilibrium makes quantification especially difficult, as the solubility of NaX is quite small in organic solvents, and NaX does not absorb light in the UV-Vis region of the electromagnetic spectrum. Simultaneous quantification of X_2 and NaX_3 was performed by least-squares fitting of multiple gaussian-type peak to UV-Vis absorption spectra as detailed in the following process:

1. Record the absorption spectrum of a standard solution of pure halogen dissolved in the solvent of interest. Call this spectrum S_1. Record the initial halogen concentration ($[X_2]_1$).

2. Add an arbitrary (but small) amount of crystalline sodium halide salt (NaX) to the cuvette and measure the absorption spectrum repeatedly as the reaction between X_2 and NaX proceeds to equilibrium. Record absorption spectra periodically until a steady state is reached and the spectrum does not change. Call the final spectrum S_2.

3. View both S_1 and S_2 and select a region of wavelengths in which both S_1 and S_2 exhibit reasonable levels of absorption for the chosen instrument and have visibly different absorption peaks. Call the lower wavelength boundary λ_a and the upper boundary λ_b. Figure 2.16 shows an example of the absorption spectra over a broad range of wavelengths and figure 2.17 shows the same spectra in a narrowed range of wavelengths.

4. Fit a sum of n Gaussian or Lorentzian functions to the absorption spectrum S_1 in the region $\lambda_1 \leq \lambda \leq \lambda_2$. Insert or remove peaks until a reasonable fit is obtained. Call

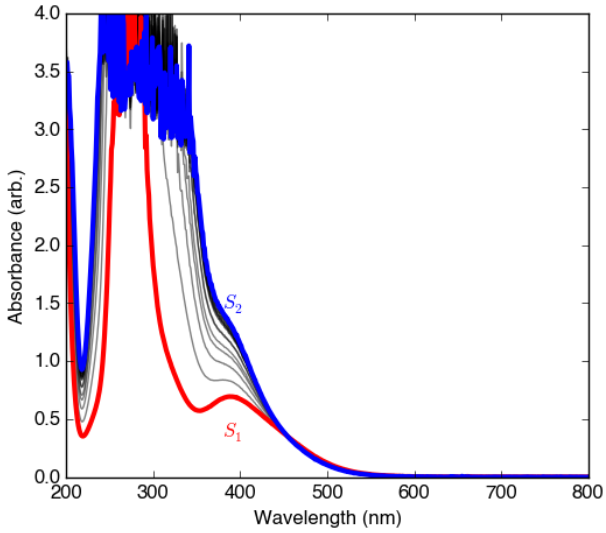

Figure 2.16: The UV-Vis absorption spectrum of iodine (Br_2) in acetonitrile (CH_3CN) is shown in red (S_1). Reaction with a small amount of crystalline NaBr leads to the formation of $NaBr_3$, which absorbs strongly below $\lambda = 450$ nm. The final absorption spectrum S_2 represents the concentrations of Br_2 and $NaBr_3$ at equilibrium.

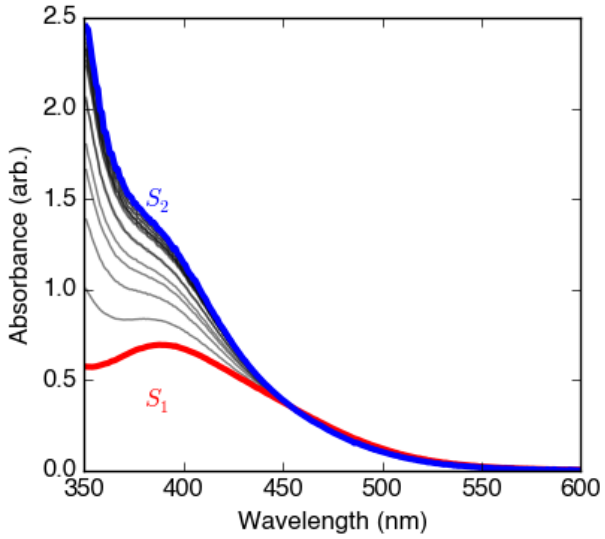

Figure 2.17: S_1 and S_2 are shown in a restricted wavelength range where both Br_2 and $NaBr_3$ contribute to the absorption spectrum and the absorbance values fall within the linear range of the instrument.

the final collection of peaks P_{X_2}. As an example, if Gaussian peak shapes are used, S_i is modeled as:

$$S_1[\lambda_a, \lambda_b] \approx P_{X_2} = \sum_{i=1}^{n} a_i \, exp(-\frac{(\lambda - p_i)^2}{2\omega_i^2}), \tag{21}$$

where a models the peak height, p models the peak center, and ω models the peak width. Figure 2.18 shows a sample fit to S_1.

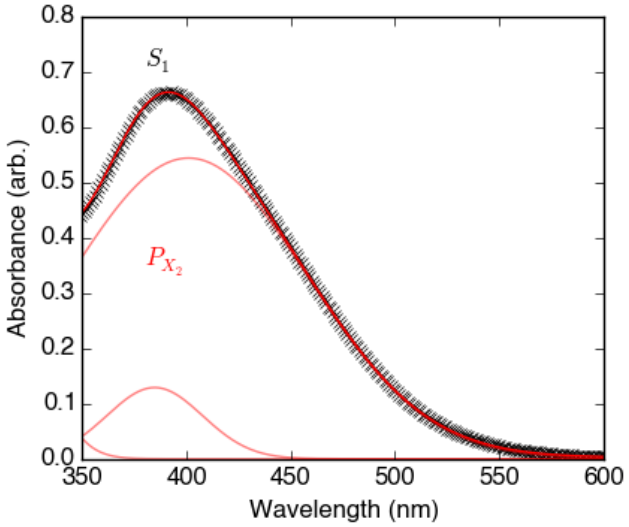

Figure 2.18: A fit of a collection of Gaussian functions P_{X_2} to the absorption spectrum S_1.

5. Fit S_2 to a sum of P_n scaled by a constant h_1 and a collection of m additional peaks (Gaussians, here) denoted by P_m:

$$S_2[\lambda_a, \lambda_b] \approx P_{X_2+NaX_3} = h_1 \times P_{X_2} + P_{NaX_3} \tag{22}$$

$$S_2[\lambda_a, \lambda_b] \approx P_{X_2+NaX_3} = h_1 \times P_{X_2} + \sum_{i=1}^{m} a_i \, exp(-\frac{(\lambda - p_i)^2}{2\omega_i^2}). \tag{23}$$

Note that the concentration of halogen after the reaction has reached equilibrium $[X]_2$

is now given by:

$$[\mathrm{X_2}] \;=\; h_1 \times\; [\mathrm{X_2}]_1 \tag{24}$$

and the concentration of trihalide is given by:

$$[\mathrm{NaX_3}] \;=\; (1 \;-\; h_1) \times\; [\mathrm{X_2}]_1. \tag{25}$$

Figure 2.19 shows the resulting data and obtained in this step.

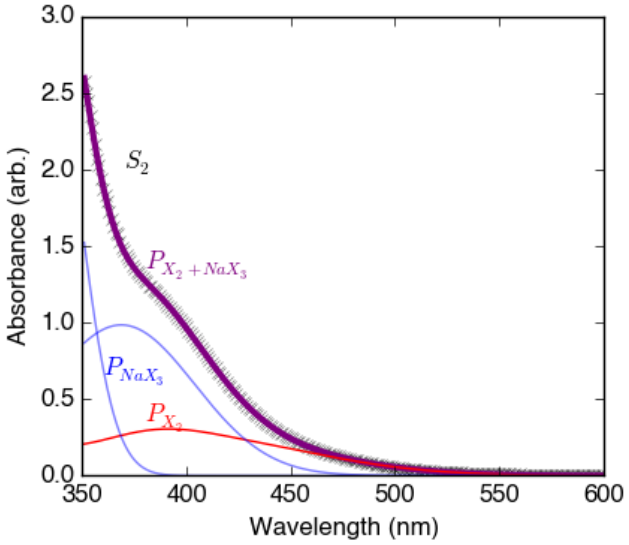

Figure 2.19: A fit of the collection of Gaussian functions $\mathrm{P}_{X_2+NaX_3}$ to the spectrum S_2.

The concentrations of halogen and sodium trihalide can now be determined in an unknown solution by fitting the absorption spectrum S_t with a linear combination of P_{X_2} and P_{NaX_3}:

$$S_t[\lambda_a, \lambda_b] \approx\; h_{X_2} \times\; P_{X_2} + h_{NaX_3} \times\; P_{NaX_3}, \tag{26}$$

where the coefficients h_{X_2} and h_{NaX_3} are related to the concentrations of $\mathrm{X_2}$ and $\mathrm{NaX_3}$:

$$[\mathrm{X_2}] \;=\; h_{X_2} \times\; [\mathrm{X_2}]_1 \tag{27}$$

and

$$[\mathrm{NaX_3}] \;=\; h_{NaX_3} \times \;(1 \;-\; h_1) \times \;[\mathrm{X_2}]_1. \tag{28}$$

The series of absorption spectra collected between S_1 and S_2 can also be used to construct a calibration line from which the error in the NaX_3 concentration can be determined (Figure 2.20). Figure 2.21 shows plots of concentration vs. time obtained from three separate reaction kinetics runs using this technique. The Python code used to produce these plots

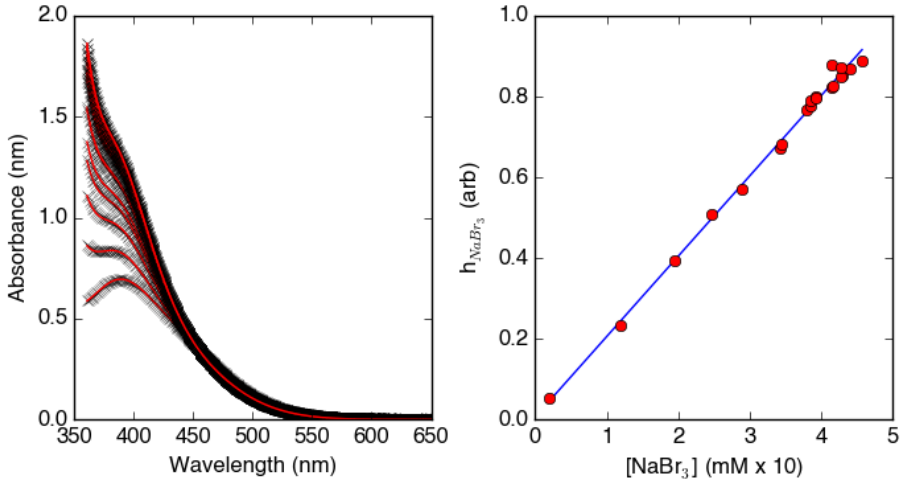

Figure 2.20: A calibration line for trihalide (NaX_3) concentration is produced by reacting a standard solution of halogen with a small amount of crystalline sodium halide salt (NaX) and monitoring the absorption spectrum until a steady state is reached. The data analysis procedure described in the text allows for both $[X_2]$ and $[NaX_3]$ to be calculated simultaneously by least-squares fitting.

is reproduced below for reference, and the gaussian functions used to model the absorption spectra are located in appendix A.

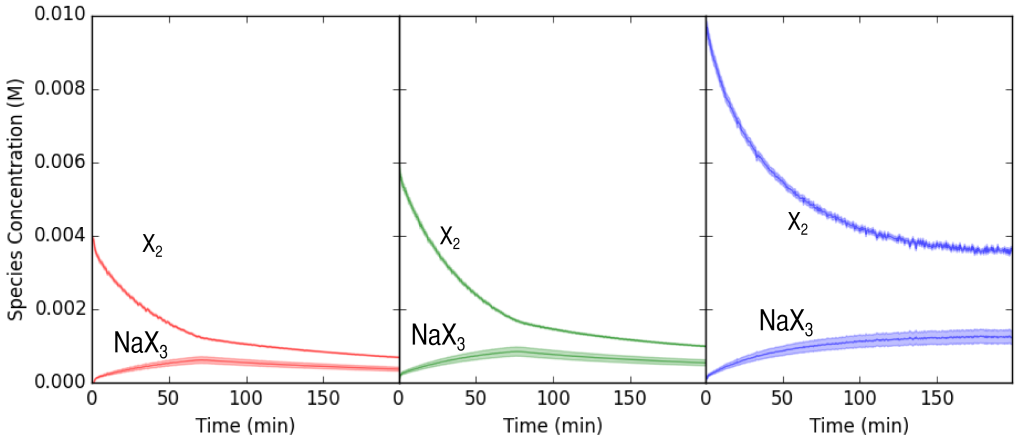

Figure 2.21: Plots of concentration versus time obtained from the data analysis procedure described in the text. Shaded regions represent the statistical error in the concentrations, computed from reference to external calibration curves.

2.9.1 Python Implementation

```python
# absorption_class.py
import spectral_functions
from scipy.optimize import curve_fit
import numpy as np


class AbsorptionSpectrum(object):
    """
    A collection of up to 5 gaussian peaks with independent parameters.

    Methods:
    generate_spectrum():
        builds the absorption spectrum based on the number of peaks
        and the provided peak_params.

    info():
        print the number of peaks and the current peak parameters

    fit(xvals, yvals):
        fits the peak parameters to the data provided

    predict(xvals, yvals):
        returns a scale factor for a spectrum of a different concentration

    get_fit_vals(xvals):
        returns an array with the fitted spectrum
    """
    SPECTRUM_MAPPING = dict(
        1: spectral_functions.gaussian1,
        2: spectral_functions.gaussian2,
        3: spectral_functions.gaussian3,
        4: spectral_functions.gaussian4,
        5: spectral_functions.gaussian5,
    )

    def __init__(self, n_peaks, guessed_params):
        self.spectrum = None
        self.n_peaks = n_peaks
        self.peak_params = np.concatenate((np.array(guessed_params),
                                           np.array([0.0])))
        self.cov = 0
        self.h = 1.0

    def generate_spectrum(self):
        """
        Selects the gaussian function with the appropriate number of peaks
        """
        self.spectrum = self.SPECTRUM_MAPPING[self.n_peaks]

    def add_peak(self, guessed_params):
        """
        adds a peak to the spectrum
        :param guessed_params:
                guessed parameters for added peak: [height, mean, variance]
        """
        self.n_peaks += 1
        orig_params = self.peak_params
        self.peak_params = np.concatenate((np.array(guessed_params),
                                           orig_params), axis=0)
        self.generate_spectrum()

    def fit(self, xvals, yvals):
        """
```

```
        optimizes all individual peak parameters to fit the spectrum provided.
        :param xvals:
            length n array of wavelengths
        :param yvals:
            length n array of absorbances
        """
        self.generate_spectrum()
        self.peak_params, self.cov = curve_fit(
            self.spectrum,
            xvals,
            yvals,
            self.peak_params
        )

    def predict(self, xvals, yvals):
        """
        optimizes a scale factor to fit the provided spectrum
        :param xvals:
            length n array of wavelengths
        :param yvals:
            length n array of absorbances
        :return:
            h scale factor (float)
        """

        def fn(xvals, h):
            return h * self.spectrum(xvals, *self.peak_params)

        self.h, _ = curve_fit(fn, xvals, yvals)

        return self.h

    def get_fit_vals(self, xvals):
        """
        show the predicted spectrum
        :param xvals:
                length n array of wavelengths
        :return:
            length n array of predicted absorbances
        """
        return self.spectrum(xvals, *self.peak_params)


class SecondSpectrum(AbsorptionSpectrum):
    def __init__(self, first_spectrum, n_peaks, guessed_params):
        self.first_spectrum = first_spectrum
        self.spectrum = None
        self.n_peaks = n_peaks
        self.peak_params = np.concatenate((np.array(guessed_params),
                                           np.array([0.0])))
        self.cov = 0
        self.h = 1.0

    def fit_second_spectrum(self, xvals, yvals):
        """
        Optimizes the peak parameters for a second species
        :param xvals:
            length n array of wavelengths
        :param yvals:
            length n array of absorbance values
        :return:
        """
        self.generate_spectrum()

```

```
128         def func(xvals, h1, *peak_params):
129             return (
130                 h1 * self.first_spectrum.get_fit_vals(xvals) +
131                 self.spectrum(xvals, *peak_params)
132             )
133 
134         h1 = np.array([1.0])
135         guess = np.concatenate((h1, self.peak_params))
136         vals, _ = curve_fit(func, xvals, yvals, guess)
137         self.peak_params = vals[1:]
138         self.h1 = vals[0]
139 
140     def get_fit_vals(self, xvals):
141         """
142         show the predicted spectrum
143         :param xvals:
144             length n array of wavelengths
145         :return:
146             length n array of predicted absorbances
147         """
148         self.generate_spectrum()
149 
150         def func(xvals, h1, *peak_params):
151             return (
152                 h1 * self.first_spectrum.get_fit_vals(xvals) +
153                 self.spectrum(xvals, *peak_params)
154             )
155 
156         return func(xvals, self.h1, *self.peak_params)
157 
158 # for testing
159 if __name__ == '__main__':
160     import numpy as np
161     from spectral_functions import gaussian1 as gauss
162     import matplotlib.pyplot as plt
163 
164     # simulate a peak with noise
165     npts = 500
166     xvals = np.linspace(0, 30, npts)
167     yvals = gauss(xvals, 15, 4, 2, 0)
168     yvals += 0.15 * np.random.randn(npts) + 1.13
169 
170     # fit a single peak
171     p1 = AbsorptionSpectrum(1, [13, 3.5, 2])
172     p1.fit(xvals, yvals)
173     fit1 = p1.get_fit_vals(xvals)
174 
175     yvals += gauss(xvals, 7, 18, 1, 0)
176 
177     # fit both peaks with two spectral components
178     p2 = SecondSpectrum(p1, 1, [7, 18, 1])
179     p2.fit_second_spectrum(xvals, yvals)
180     fit2 = p2.get_fit_vals(xvals)
181 
182     # plot the results
183     plt.figure()
184     plt.plot(xvals, yvals, '.', alpha=0.6, label='simulated spectrum')
185     plt.plot(xvals, fit1, color='red', linewidth=2, alpha=0.6,
186              label='first component')
187     plt.plot(xvals, fit2, color='blue', linewidth=2, alpha=0.6,
188              label='both components')
189     plt.legend()
190     plt.show()
```

```python
# data_workup_example.py
import pandas as pd
import numpy as np
import matplotlib.pyplot as plt
from scipy.optimize import curve_fit

import tools.spectral_functions as spec
import tools.data_io as data_io
from tools.absorption_class import AbsorptionSpectrum, SecondSpectrum

"""
Here we train a collection of gaussian-like functions to UV-Vis absorption
spectra collected on solutions of known bromine and sodium tribromide
concentration over the wavelength range 360 to 650 nm.

    *The pure bromine spectrum is represented by a sum of three gaussians.
    *The sodium tribromide spectrum is represented by a sum of two gaussians.

Once the individual spectral shapes are determined, the concentration of both
species in an unknown solution can be determined by finding the optimum
intensity contribution of each peakshape to the observed absorption spectrum.
"""

# load training data as pandas DataFrames and measurement time as arrays
train1, train1_t = data_io.clean_agilent_uvvis_data('data/TRAIN1.TXT')
train2, train2_t = data_io.clean_agilent_uvvis_data('data/TRAIN2.TXT')

# We are working with Bromine and Sodium Tribromide, so label accordingly
HALOGEN_LABEL = '[Br2] (M)'
TRIHALIDE_LABEL = '[NaBr3] (M)'
TIME_LABEL = 'Time (min)'
ABSORBANCE_LABEL = 'Absorbance (Arb.)'
WAVELENGTH_LABEL = 'Wavelength (nm)'

# get wavelength values from first column
WLs = train1.index.values[1:].astype(float)

##############FIT RAW BROMINE SPECTRUM################

# set upper and lower bounds for first training set
low, high = 320.0, 650.0
L1 = np.argwhere(WLs > low)[0][0]
L2 = np.argwhere(WLs > high)[0][0]

xvals, yvals = WLs[L1:L2], train1[0][1:].values[L1:L2]

# Initial values for curve_fit
p0_Br2 = [3.0, 280.0, 30.0,
          0.7, 390.0, 20.0,
          0.2, 460.0, 20.0]

Br2_spectrum = AbsorptionSpectrum(3, p0_Br2)

# optimize parameters
Br2_spectrum.fit(xvals, yvals)

# compute the fitted spectrum
Br2_fit = Br2_spectrum.get_fit_vals(xvals)

# show each individual peak
Br2_pks = Br2_spectrum.peak_params

g1, g2, g3 = (spec.gaussian1(xvals, Br2_pks[0], Br2_pks[1], Br2_pks[2], 0.0),
```

```
64                spec.gaussian1(xvals, Br2_pks[3], Br2_pks[4], Br2_pks[5], 0.0),
65                spec.gaussian1(xvals, Br2_pks[6], Br2_pks[7], Br2_pks[8], 0.0))
66
67  # plot results
68  plt.figure()
69  plt.title('Pure Br2 in Acetonitrile')
70  plt.xlabel(WAVELENGTH_LABEL)
71  plt.ylabel(ABSORBANCE_LABEL)
72  plt.plot(xvals, yvals, 'x', label='data')
73  plt.plot(xvals, Br2_fit, color='r', label='fit')
74  plt.plot(xvals, g1, xvals, g2, xvals, g3)
75  plt.legend()
76
77  ##########FIT SODIUM TRIBROMIDE SPECTRUM############
78
79  # set upper and lower bounds
80  low, high = 360.0, 650.0
81  L1 = np.argwhere(WLs > low)[0][0]
82  L2 = np.argwhere(WLs > high)[0][0]
83
84  last_line = len(train1_t) - 1
85  xvals, yvals = WLs[L1:L2], train1[last_line][1:].values[L1:L2]
86
87  # Initial values for curve_fit
88  NaBr3_p0 = [1.0, 400, 20,
89              2.5, 340, 20]
90
91  # optimize NaBr3 parameters
92  NaBr3_spectrum = SecondSpectrum(Br2_spectrum, 2, NaBr3_p0)
93  NaBr3_spectrum.fit_second_spectrum(xvals, yvals)
94  NaBr3_fit = NaBr3_spectrum.get_fit_vals(xvals)
95  NaBr3_pks = NaBr3_spectrum.peak_params
96
97  # show each individual peak contributing to the spectrum
98  g1 = spec.gaussian1(xvals, NaBr3_pks[1], NaBr3_pks[2], NaBr3_pks[3], 0.0)
99  g2 = spec.gaussian1(xvals, NaBr3_pks[4], NaBr3_pks[5], NaBr3_pks[6], 0.0)
100
101 # plot results
102 plt.figure()
103 plt.title('1-x B2 + x NaBr3 in Acetonitrile')
104 plt.xlabel(WAVELENGTH_LABEL)
105 plt.ylabel(ABSORBANCE_LABEL)
106 plt.plot(xvals, yvals, 'x', label='data')
107 plt.plot(xvals, NaBr3_fit, color='r', label='fit')
108 plt.plot(xvals, g1, xvals, g2)
109 plt.legend()
110
111
112 def variable_Br2_NaBr3_spectrum(WL, hBr2, hNaBr3):
113     """
114     Computes the predicted absorbance value for given wavelength,
115     Br2 height, and NaBr3 height.
116
117     Parameters
118     ----------
119     WL: scalar
120         Wavelength in nm
121
122     hBr2: scalar
123         height of Br2 absorption spectrum
124
125     hNaBr3: scalar:
126         height of NaBr3 absorption spectrum
127
```

```
    Returns
    -------
    Predicted Absorbance: float
    """
    return (hBr2 * Br2_spectrum.get_fit_vals(WL) +
            hNaBr3 * NaBr3_spectrum.get_fit_vals(WL))


###########TRAIN###############

# set upper and lower bounds
low, high = 360.0, 650.0
L1 = np.argwhere(WLs > low)[0][0]
L2 = np.argwhere(WLs > high)[0][0]

Br2_conc_i = 0.00342  # Initial Br2 concentration in Mol/L.

(hBr2, hNaBr3) = np.zeros((2, len(train2_t)))

f, (ax1, ax2) = plt.subplots(1, 2)
ax1.set_xlabel(WAVELENGTH_LABEL)
ax1.set_ylabel(ABSORBANCE_LABEL)
ax2.set_xlabel(TRIHALIDE_LABEL)
ax2.set_ylabel('Peakheight (arb.)')

for i in range(len(train2_t)):
    xvals, yvals = WLs[L1:L2], train2[i][1:].values[L1:L2]

    # optimize parameters
    train2_opt, train2_cov = curve_fit(variable_Br2_NaBr3_spectrum,
                                       xvals,
                                       yvals)

    # add values to appropriate arrays
    (hBr2[i], hNaBr3[i]) = train2_opt

    # compute the fitted spectrum
    fit = variable_Br2_NaBr3_spectrum(xvals, train2_opt[0], train2_opt[1])

    # plot data and fit for each spectrum
    ax1.plot(xvals, yvals, 'x')
    ax1.plot(xvals, fit, color='r')

# compute [NaBr3] for all spectra
NaBr3_conc = Br2_conc_i * (1.0 - hBr2 / hBr2[0])

# fit calibration line to data
line, cov = curve_fit(spec.linear, NaBr3_conc, hNaBr3)

# plot calibration points and line of best fit
ax2.plot(NaBr3_conc, hNaBr3, 'x')
ax2.plot(NaBr3_conc, spec.linear(NaBr3_conc, line[0], line[1]))

##############PREDICT#################


def compute_concs_from_spectra(dataset, time):
    """
    get_concs(dataset)

    Computes the concentrations of Br2 and NaBr3 in acetonitrile
    from trained peak profiles and calibration spectra.

    Parameters
```

```
    ----------
    dataset: Pandas DataFrame containing wavelengths in the index column,
             time values in the first row, and absorbance readings in all cells.

    Returns
    -------
    (time, Br2 concentration (M), NaBr3 concentration (M))
        (tuple of three NumPy arrays)
    """
    WLs = dataset.index.values[1:].astype(float)

    # lower and upper wavelengths for fit
    low, high = 360, 650

    # set upper and lower bounds
    L1 = np.argwhere(WLs > low)[0][0]
    L2 = np.argwhere(WLs > high)[0][0]

    hbr2, hnabr3 = np.zeros((2, len(time)))  # empty arrays for fitted parameters

    plt.figure()
    plt.axis([low, high, 0, 2])
    plt.title('All spectra + fits')
    plt.xlabel(WAVELENGTH_LABEL)
    plt.ylabel(ABSORBANCE_LABEL)

    for i in range(len(time)):
        xvals, yvals = WLs[L1:L2], dataset[i][1:].values[L1:L2]

        # optimize parameters
        g5Sopt, g5Scov = curve_fit(variable_Br2_NaBr3_spectrum, xvals, yvals)

        # compute the fitted spectrum
        fit = variable_Br2_NaBr3_spectrum(xvals, g5Sopt[0], g5Sopt[1])

        # add values to appropriate arrays
        (hbr2[i], hnabr3[i]) = g5Sopt

        # plot data and fit for each spectrum
        plt.plot(xvals, yvals, 'x', color='black', alpha=0.4)
        plt.plot(xvals, fit, color='r')

    return time, Br2_conc_i * (hbr2 / hbr2[0]), hnabr3 / line[0]


# Predict Br2 and NaBr3 concentrations for all spectra in calibration
time, cBr2, cNaBr3 = compute_concs_from_spectra(train1, train1_t)

# plot Conc. vs Time for the calibration run
FIGTITLE = 'Predicted Concentrations' )
plt.figure()
plt.title(FIGTITLE)
plt.xlabel(TIME_LABEL)
plt.ylabel('[X] (M)')
plt.plot(time, cBr2, 'x', color='red', label=HALOGEN_LABEL)
plt.plot(time, cNaBr3, 'x', color='blue', label=TRIHALIDE_LABEL)
plt.legend()
plt.show()
```

3 Evolution of Magnetism in the $Na_{3-\delta}(Na_{1-x}Mg_x)Ir_2O_6$ Series of Honeycomb Iridates

This work was co-written with the following authors and is published under
the following citation:

Journal of Solid State Chemistry **224**, 28-35 (2015)

http://dx.doi.org/10.1016/j.jssc.2014.03.013

David C. Wallace[1,2], Craig M. Brown[1,2], Tyrel M. McQueen[1,2,*]

[1]Department of Chemistry, The Johns Hopkins University, Baltimore, MD 21218, USA

[2]Institute for Quantum Matter, Department of Physics and Astronomy,
The Johns Hopkins University, Baltimore, MD 21218, USA

[3]NIST Center For Neutron Research, Gaithersburg, MD, 20899, USA

[4]Department of Chemical and Biomolecular Engineering,
University of Delaware, Newark, Delaware 19716, USA

[*]Corresponding Author

3.1 Abstract

The structural and magnetic properties of a new series of iridium-based honeycomb lattices with the formula $Na_{3-\delta}(Na_{1-x}Mg_x)Ir_2O_6$ ($0 \leq x \leq 1$) are reported. As x and δ are increased, the honeycomb lattice contracts and the strength of the antiferromagnetic interactions decreases systematically due to a reduction in Ir–O–Ir bond angles. Samples with imperfect stoichiometry exhibit disordered magnetic freezing at temperatures T_f between 3.4 K and 5 K. This glassy magnetism likely arises due to the presence of non-magnetic Ir^{3+}, which are distributed randomly throughout the lattice, with a possible additional contribution from stacking faults. Together, these results demonstrate that chemical defects and non-stoichiometry have a significant effect on the magnetism of compounds in the A_2IrO_3 materials family.

3.2 Introduction

5*d* transition metal oxide materials have recently attracted significant interest due to the comparable energy scales of crystal field stabilization, electronic correlations (Hubbard U), and spin-orbit coupling [24]. In particular, iridium oxides are of great interest due to the ability of Ir to adopt a d^5 electronic configuration in its 4+ oxidation state, yielding a singly-occupied orbital with non-trivial spin texture in the strong spin-orbit coupling limit. This electronic configuration has been predicted to give rise to an unusual pattern of superexchange interactions, resulting in magnetic frustration and possible spin liquid behavior [25–27]. For this reason, the A_2IrO_3 (A = Li, Na) family of layered honeycomb materials have been the subject of intense scrutiny [28–32].

The majority of experimental work on Na_2IrO_3 and Li_2IrO_3 has focused on single-crystalline specimens grown via "self-flux." Despite strong antiferromagnetic interactions in Na_2IrO_3, evidenced by a reported large negative Weiss temperature θ_W = -116 K, long-range antiferromagnetic order is only present below a Néel temperature of T_N = 15 K, demonstrating that that Na_2IrO_3 is in a magnetically frustrated regime [33, 34]. A study of

the $(Na_{1-x}Li_x)_2IrO_3$ solid solution revealed that θ_W as well as T_N vary significantly with x, and the magnetism reaches a peak in frustration at the intermediate value of $x = 0.7$ [35]. Isovalent substitution of Li for Na in the A_2IrO_3 structure presumably has the effect of modulating the exchange interaction strengths between neighboring Ir sites, however this effect has not been systematically explored. Recently, a broad variety of new ternary Ir oxides with the formula $Na_{3-\delta}MIr_2O_6$ (M = Zn, Cu, Ni, Co, Fe and Mn) were reported [49], but no unifying picture of the magnetism demonstrated by this family can yet be drawn.

Here, we report another new member of this chemical family, $Na_{3-\delta}(Na_{1-x}Mg_x)Ir_2O_6$, in which Mg substitutes for Na in the honeycomb planes and the Na content between planes is variable (Fig. 3.1(a)). Aliovalent substitution of Mg for Na in the honeycomb plane offers a convenient and controllable method by which to tune the lattice parameters of the unit cell and, in doing so, vary the exchange interactions between neighboring Ir sites. Additionally, we resolve the discrepancy in magnetic behavior between polycrystalline and single-crystalline samples of Na_2IrO_3, where the former are spin glasses and the latter exhibit long range antiferromagnetic (AFM) order [33], by showing that Na_2IrO_3 decomposes rapidly in air as previously reported, and that this decomposition destroys AFM order [51].

3.3 Materials and Methods

Polycrystalline Na_2IrO_3 was prepared via a method similar to what was previously reported [33]: Na_2CO_3 (NOAH Technologies Corp., 99.9%)[1], MgO (NOAH Technologies Corp., 99.99%) and Ir black (J&J Materials Inc.) were intimately ground using an agate mortar and pestle and pelletized. The sample was heated in a covered alumina crucible to 750 °C over a period of 4 hrs, held at that temperature for 30 hrs, then quenched in air. The pellet was then reground with an additional 5 mol % Na_2CO_3, pelletized, and placed into a fur-

[1]Certain commercial suppliers are identified in this paper to foster understanding. Such identification does not imply recommendation or endorsement by the National Institute of Standards and Technology, nor does it imply that the materials or equipment identified are necessarily the best available for the purpose.

nace preheated to 900 °C where it dwelled for and additional 48 hrs. After the final heating, samples were removed from the furnace and allowed to cool in an argon filled glovebox to prevent reaction with laboratory air. Polycrystalline samples of $Na_{3-\delta}(Na_{1-x}Mg_xIr_2)O_6$ were prepared via a similar method: Na_2CO_3, MgO and Ir metal powder were intimately ground and pelletized. Samples were heated in covered alumina crucibles to 750 °C over a period of four hrs, held at that temperature for 30 hrs, then quenched in air. Samples were then reground, pelletized, and placed into a furnace preheated to 900 °C where they dwelled for between 48 and 96 hrs, followed by quenching in air. The 900 °C heating was repeated with intermediate regrindings until the laboratory x-ray powder diffraction (XRPD) data showed no impurity phases and no change in lattice parameters or relative peak intensities between subsequent heatings. After the final heating, samples were processed and stored in an argon-filled glovebox to prevent reaction with air. Samples of suitable size for neutron powder diffraction (NPD) were prepared via a similar method, but with an additional two week heating at 900 °C.

Laboratory XRPD data were collected on a Bruker D8 Focus diffractometer using Cu-Kα radiation with λ_1 = 1.5406 Å and λ_2 = 1.5445 Å and equipped with a LynxEye CCD detector. Rietveld refinements to laboratory XRPD data were performed using TOPAS (Bruker AXS). NPD data were collected at the NIST Center for Neutron Research using the BT-1 high-resolution powder diffractometer with an incident wavelength of λ = 1.5419 Å using a Cu (311) monochromator and with 15' and 60' for primary and secondary collimation, respectively. Rietveld refinements to NPD data were performed in GSAS/EXPGUI [16, 37]. Samples were loaded into vanadium cells and sealed in an inert helium glovebox to prevent exposure to air. DC and AC magnetization measurements were carried out using a Quantum Design Physical Properties Measurement System. Elemental analyses were performed via inductively-coupled plasma optical emission spectroscopy (ICP-OES) by Evans Analytical Group. XRPD simulations were performed using DIFFaX [18].

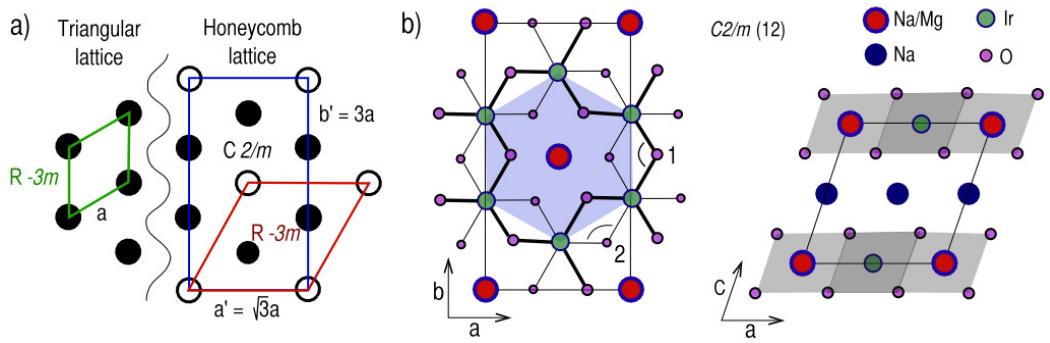

Figure 3.1: **(a)** A simple triangular lattice can be described by an R-*3m* unit cell (green) with in-plane lattice parameter a. Formation of honeycomb order by substitution of one third of the atoms in the triangular lattice is accommodated by a $\sqrt{3}$ expansion of the triangular lattice constant yielding a larger R-*3m* unit cell (red). Different stacking arrangements (not shown) can require a lower symmetry unit cell, such as the C2/*m* cell shown (blue). **(b)** The structure of $Na_{3-\delta}(Na_{1-x}Mg_x)Ir_2O_6$ is described by the C2/*m* cell shown in the *ab*-plane. Oxygen atoms above the honeycomb plane are bonded to Ir with thick black lines, while those below the plane are bonded to Ir with thin lines. IrO_6 octahedra share edges to form a honeycomb lattice, highlighted by a light blue hexagon. Two distinct Ir–O–Ir bond angles, labeled 1 and 2, are possible in this structure. The structure is also shown in the *ac*-plane to highlight the stacking arrangement corresponding to the C2/*m* cell.

3.4 Results and Discussion

3.4.1 Structure

The structure of the A_2IrO_3 family of materials is derived from the layered triangular lattice compound α–$NaFeO_2$ (Fig. 3.1(a)): when Na substitutes for one third of the Fe sites in $NaFeO_2$ in an ordered fashion, a layered honeycomb lattice is formed and the chemical formula becomes Na_2FeO_3. For this reason, the structural formula of A_2IrO_3 can be described more intuitively as $A_3A'Ir_2O_6$, where electronically active $A'Ir_2O_6$ honeycomb layers, comprised of tilted, edge-sharing octahedra, are separated by electronically inert layers of A cations. The honeycomb order in these layers is energetically favorable due to the large differences in atomic radii and oxidation states of Ir in comparison to the A' cation. Because electronically active honeycomb layers are separated by electronically inert triangular layers, the A_2IrO_3 family are essentially layered two dimensional materials.

Table 3.1: Results of Rietveld refinement to NPD data collected on $Na_3Mg_{0.5}Ir_2O_6$ (sample 7).

$Na_3Mg_{0.5}Ir_2O_6$	(*C2/m* (12))		5 K	100 K	295 K
		a (Å)	5.3565(3)	5.3585(3)	5.3621(5)
		b (Å)	9.3172(5)	9.3216(5)	9.3294(9)
		c (Å)	5.6032(3)	5.6069(4)	5.6186(4)
		β (°)	108.617(7)	108.632(8)	108.58(1)
Na1 (2*d*)	$\frac{1}{2}$,0,$\frac{1}{2}$	occ.	0.81(1)	0.81(1)	0.81(1)
		U_{iso}	0.020(1)	0.021(1)	0.025(2)
Na2 (4*h*)	$\frac{1}{2}$,*y*,$\frac{1}{2}$	occ.	0.81(1)	0.81(1)	0.81(1)
		y	0.328(2)	0.334(2)	0.326(3)
		U_{iso}	0.020(1)	0.021(1)	0.025(2)
Na3/Mg1 (2*a*)	0,0,0	occ.	0.54/0.46	0.54/0.46	0.54/0.46
		U_{iso}	0.0247(4)	0.0209(1)	0.0180(5)
Ir1 (4*g*)	$\frac{1}{2}$,*y*,0	*y*	0.1691(8)	0.1660(6)	0.1740(7)
		U_{iso}	0.0247(4)	0.0209(1)	0.0180(5)
O1 (8*j*)	*x*,*y*,*z*	*x*	0.772(1)	0.754(2)	0.765(2)
		y	0.1657(9)	0.1723(7)	0.1668(9)
		z	0.7939(6)	0.7956(8)	0.794(1)
		U_{iso}	0.0197(3)	0.0212(6)	0.0296(9)
O2 (4*i*)	*x*,0,*z*	*x*	0.717(2)	0.728(2)	0.719(3)
		z	0.203(1)	0.204(2)	0.201(2)
		U_{iso}	0.0197(3)	0.0212(6)	0.0296(9)
Ir–O–Ir 1(°)			99.1(4)	97.5(3)	100.7(6)
Ir–O–Ir 2(°)			94.0(3)	95.0(3)	93.8(3)
		χ^2	1.25	1.211	1.009
		R_{wp}	9.98	10.35	12.87
		R_p	7.95	8.25	11.09

This fact can give rise both to interesting physics, and to complex structural disorder.

Fig. 3.2(a) shows simulated XRPD data that demonstrate how disordered stacking arrangements affect the observed XRPD pattern. When honeycomb lattices are stacked in a perfectly ordered manner, sharp reflections are observed in the XRPD data between scattering angle 2θ = 19° and 32° – these are often referred to as supercell reflections, as the arise from the additional honeycomb ordering within the triangular layer. This structure (Fig. 3.1(a)) can be accounted for by a larger R$\bar{3}$*m* cell where the *a* axis is expanded by $\sqrt{3}$ compared to the triangular R$\bar{3}$*m* cell, or to lower symmetry variations such as the monoclinic C2/*m* or C2/*c* cells commonly observed (Fig. 3.1(b)) [34, 38]. If stacking faults

Table 3.2: Results of Rietveld refinement to NPD data collected on $Na_{2.4}MgIr_2O_6$ (sample 11).

$Na_{2.4}MgIr_2O_6$	(*C2/m* (12))		5 K	100 K
		a (Å)	5.3084(6)	5.3091(5)
		b (Å)	9.197(1)	9.1992(9)
		c (Å)	5.6461(3)	5.6473(3)
		β (°)	108.440(7)	108.441(6)
Na1 (2*d*)	$\frac{1}{2}$,0,$\frac{1}{2}$	occ.	0.77(1)	0.77(1)
		U_{iso}	0.025(1)	0.041(9)
Na2 (4*h*)	$\frac{1}{2}$,*y*,$\frac{1}{2}$	occ.	0.77(1)	0.77(1)
		y	0.331(3)	0.343(2)
		U_{iso}	0.025(1)	0.041(9)
Na3/Mg1 (2*a*)	0,0,0	occ.	0/1	0/1
		U_{iso}	0.0220(5)	0.041(5)
Ir1 (4*g*)	$\frac{1}{2}$,*y*,0	*y*	0.1634(9)	0.171(1)
		U_{iso}	0.0230(5)	0.041(5)
O1 (8*j*)	*x*,*y*,*z*	*x*	0.763(2)	0.766(2)
		y	0.162(1)	0.164(1)
		z	0.802(1)	0.798(1)
		U_{iso}	0.0184(4)	0.012(4)
O2 (4*i*)	*x*,0,*z*	*x*	0.724(3)	0.726(2)
		z	0.198(2)	0.189(2)
		U_{iso}	0.0184(4)	0.012(4)
		Ir–O–Ir 1 (°)	97.8(6)	99.5(5)
		Ir–O–Ir 2 (°)	94.4(4)	93.9(3)
		χ^2	1.051	1.015
		R_{wp}	9.26	9.10
		R_p	7.95	8.00

Table 3.3: results of ICP-OES elemental analysis performed on $Na_3Mg_{0.5}Ir_2O_6$ and $Na_{2.4}MgIr_2IrO_6$ compared with compositions determined from Rietveld refinement to NPD data. Ir contents determined from ICP-OES are anomalously low due to complications which arose in the dissolution process.

Sample No.	*NPD Formula*		Na : Mg : Ir molar ratio
7	$Na_{2.5}Na_{0.5}Mg_{0.5}Ir_2O_6$	*ICP-OES*	6.52 : 1.00 : 3.23
		NPD	7.00 : 1.00 : 4.00
11	$Na_{2.4}MgIr_2O_6$	*ICP-OES*	2.30 : 1.00 : 1.49
		NPD	2.40 : 1.00 : 2.00

are introduced, even with a low probability of occurrence, the supercell reflections become broadened and attenuated as shown in Fig. 3.2(a) with 5% stacking faults. Fig. 3.2(b) shows XRPD data collected on three different samples of Na_2IrO_3, each with a different degree of structural disorder. Rietveld refinement to data collected on a sample with stacking faults can incorrectly account for the observed loss in supercell reflection intensity by introducing cation site mixing in the honeycomb plane. The energy cost associated with producing a stacking fault in Na_2IrO_3 and structurally analogous systems is very small, and is thus significantly more likely to occur than antisite disorder [34, 36]. Similarly, a refinement can give the illusion of small particle size in order to account for the observed broadening of the supercell reflections. The same effect is observed in neutron diffraction, though the honeycomb order may be less apparent if atoms in the honeycomb layer have similar neutron scattering cross sections. It is therefore quite difficult to make accurate structural characterizations of samples with significant stacking disorder using neutron or x-ray diffraction techniques.

Fig. 3.3 shows NPD datasets collected on $Na_3Mg_{0.5}Ir_2O_6$ at T = 5, 100, and 295 K, along with Rietveld refinements to the data. Small supercell reflections were observed that could not be indexed using the standard R$\bar{3}m$ cell for a triangular lattice. To account for this, a refinement was attempted using an R$\bar{3}m$ cell with a $\sqrt{3}$ expansion of the a-axis from the corresponding triangular cell, but this did not accurately index the observed supercell reflections. The reflections were properly indexed using the lower symmetry monoclinic space group C2/m (12). In order to determine cation site occupancies, it was assumed that no site mixing occurs between sites in the honeycomb plane (4g and 2a), and the 4g site was fixed at full Ir occupancy. The 2a site was assumed to have mixed Na/Mg occupancy. It was further assumed that Mg only substitutes for Na at the 2a site. The interplane Na sites (2d and 4h) were constrained to have the same occupancy, as were the O1 and O2 sites (8j and 4i). Occupancies were then allowed to refine freely within the constraints. The occupancies determined from refinement to the T = 5 K data were then fixed in refinements

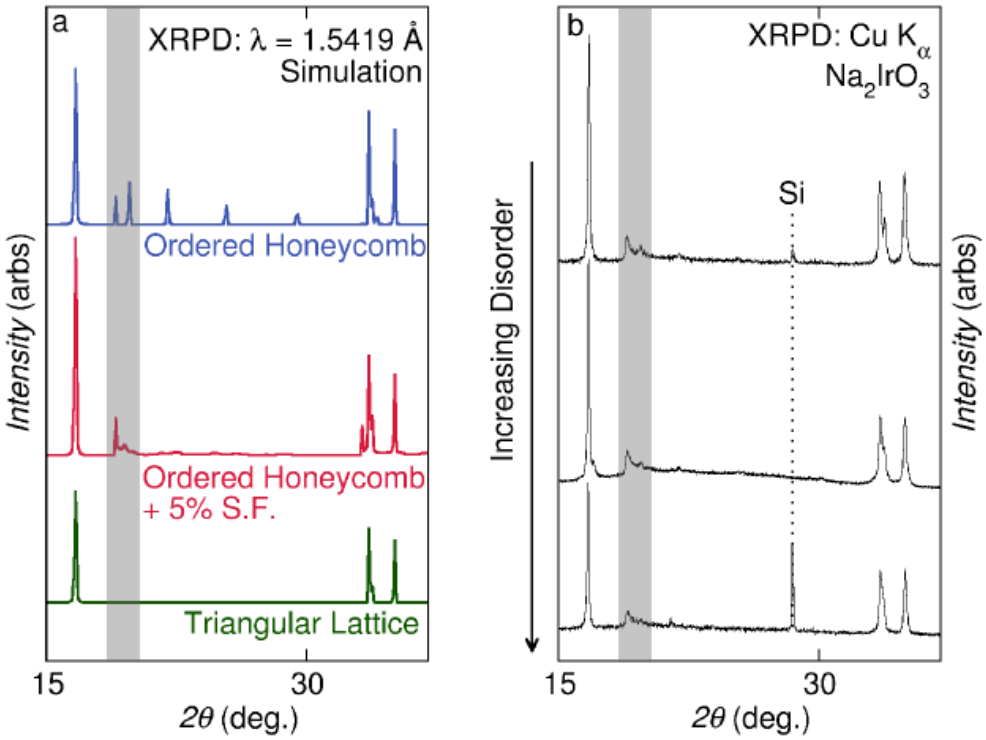

Figure 3.2: **(a)** XRPD patterns simulated using DIFFaX are shown for layered structures of the following types: triangular (green), ordered honeycomb (blue), and ordered honeycomb with 5% stacking faults (red). The influence of honeycomb ordering on the XRPD pattern is most apparent in the shaded region between $2\theta = 18^\circ$ and 22°. **(b)** XRPD data collected on three different samples of Na_2IrO_3 with varying degrees of structural disorder. The top sample has the fewest stacking faults, as illustrated by the sharp peaks in the shaded region between $2\theta = 18^\circ$ and 22°.

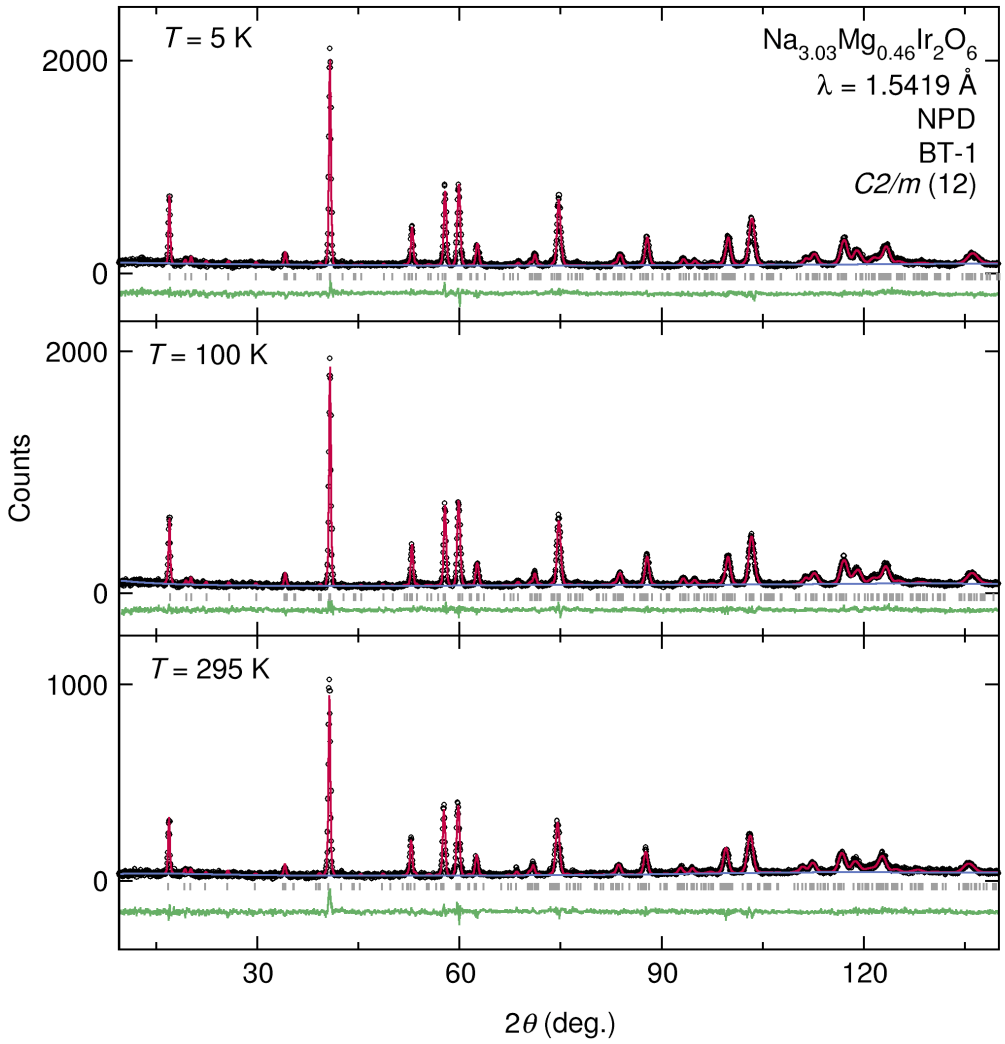

Figure 3.3: NPD data (black circles) collected on $Na_3Mg_{0.5}Ir_2O_6$ at T = 5 K, 100 K, and 295 K are shown along with Rietveld refinements (red) and the difference between the data and the fit (green). Tick marks (gray) indicate the positions of expected Bragg reflections.

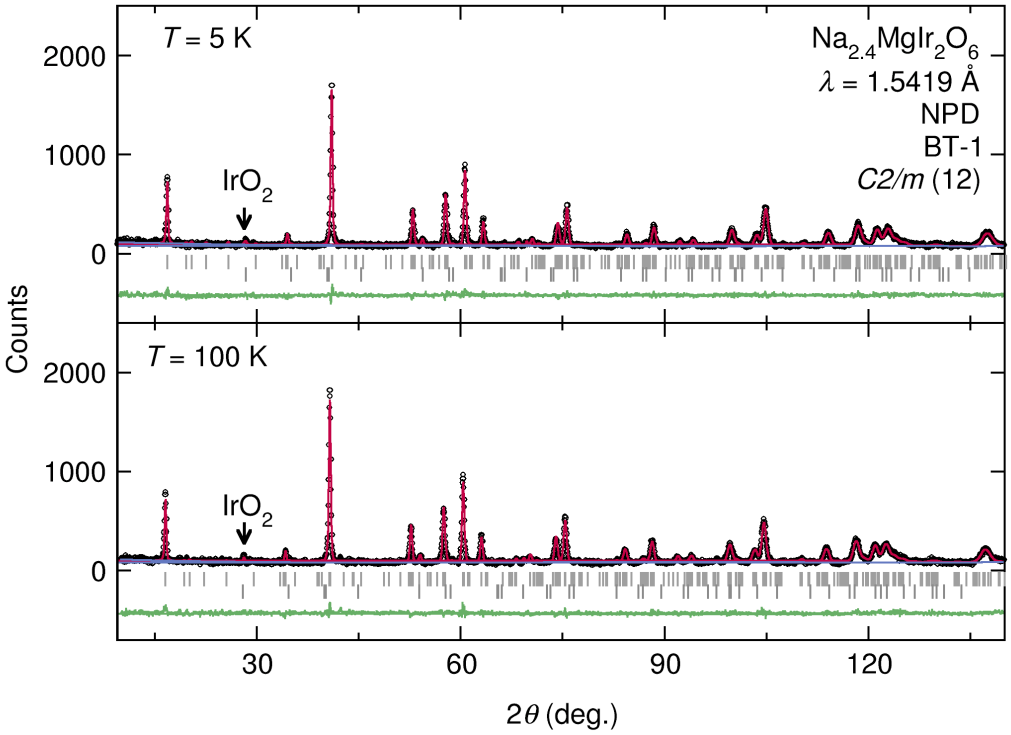

Figure 3.4: NPD data (black circles) collected on $Na_{2.4}MgIr_2IrO_6$ at T = 5 K and 100 K are shown along with Rietveld refinements (red) and the difference between the data and the fit (green). A small ($\sim$ 10%) IrO_2 impurity was present in the sample, and was included as a separate phase in the refinements. Tick marks (gray) indicate the positions of expected Bragg reflections. Tick marks corresponding to the IrO_2 impurity peak positions are located below the tick marks for the structure.

to data collected at higher temperatures. Due to the high correlation between isotropic displacement and occupancy, occupancies were determined with fixed U_{iso} = 0.005, then U_{iso} was allowed to refine freely. The results of these refinements are listed in Table 3.1. Fig. 3.4 shows NPD datasets collected on $Na_{2.4}MgIr_2O_6$ at T = 5 K and 100 K. Rietveld refinements to these datasets were carried out in the same way as for the previous sample, however, a small IrO_2 impurity was present in this sample, and was included as a separate phase in the refinements. The results of these refinements are listed in Table 3.2. Lattice parameters for $Na_{2.4}MgIr_2O_6$ at room temperature were determined from laboratory XRPD data collected using an air-free sample holder sealed under argon.

To confirm the compositions of the samples used for NPD, elemental analyses were performed via ICP-OES. The results of these analyses are shown in Table 3.3. Initial attempts to dissolve the samples were unsuccessful, and the samples had to be recovered and re-dissolved using microwave digestion. While the Na/Mg ratios agree well with the compositions determined from NPD, the Ir content is anomalously low for both samples, which is likely due to the difficulty associated with fully dissolving Ir and its oxides.

Table 3.4: Target stoichiometries and unit cell parameters determined from XRPD data collected at room temperature of all compounds studied in this work. Compositions marked with an asterisk were determined by Rietveld refinement to NPD data collected on the final product and verified via ICP-OES. The 4*g*/2*a* site mixing percentages, referred to as "% Disorder," are a rough measure of the amount of structural disorder present in the sample.

Sample No.	*Target Stoichiometry*	*a* (Å)	*b* (Å)	*c* (Å)	β (°)	*% Disorder*
1	$Na_3NaIr_2O_6$	5.4288(1)	9.4029(1)	5.6133(2)	108.999(4)	30%
2	$Na_3NaIr_2O_6$ (8h in air)	5.4270(1)	9.3999(1)	5.6135(2)	108.991(5)	20%
3	$Na_3Na_{0.9}Mg_{0.1}Ir_2O_6$	5.4194(1)	9.3867(1)	5.6088(3)	108.63(5)	38%
4	$Na_3Na_{0.8}Mg_{0.2}Ir_2O_6$	5.4132(3)	9.3759(3)	5.6188(3)	108.685(6)	50%
5	$Na_3Na_{0.7}Mg_{0.3}Ir_2O_6$	5.4036(2)	9.3593(2)	5.6198(3)	108.901(6)	37%
6	$Na_3Na_{0.5}Mg_{0.5}Ir2O_6$	5.3893(1)	9.3345(1)	5.6291(3)	108.914(5)	32%
7	$Na_{2.5}Na_{0.5}Mg_{0.5}Ir_2O_6$*	5.3621(5)	9.3294(9)	5.6186(4)	108.58(1)	–
8	$Na_3Na_{0.52}Mg_{0.48}Ir_2O_6$	5.3860(2)	9.3290(2)	5.6316(3)	108.880(5)	38%
9	$Na_{2.56}Na_{0.5}Mg_{0.5}Ir_2O_6$	5.3623(3)	9.2878(3)	5.6427(1)	108.295(2)	30%
10	$Na_{2.46}Na_{0.24}Mg_{0.76}Ir_2O_6$	5.3488(1)	9.2643(1)	5.6459(2)	108.620(4)	28%
11	$Na_{2.4}MgIr_2O_6$*	5.3171(1)	9.2094(1)	5.6707(3)	108.499(6)	32%

The structures of all other samples in the series were characterized via laboratory XRPD. Rietveld refinements were carried out using the reported structure for Na_2IrO_3 (space group C2/*m*) [34]. However, because Ir is the dominant x-ray scatterer and stacking disorder is present, the *a* and *b* lattice parameters of the monoclinic cell were first obtained by performing a Le Bail fit to the data using space group $R\bar{3}m$, where the *a*-axis is the nearest-neighbor distance in the honeycomb lattice. The resulting *a* lattice parameter was converted to the the *a* and *b* lattice parameters of the monoclinic cell, which were then fixed for the remainder of the refinement. In this way, site mixing between the 4*g* and 2*a* sites can be introduced in order to improve relative peak intensities without adversely affecting the lattice parameters. This is particularly important when comparing compounds within a series that may have varying degrees of stacking disorder and site mixing. For reporting purposes, we refer to the resulting site-mixing percentages as the percent of disorder, as they are likely due to stacking faults rather than site mixing. The lattice constants and percents of disorder determined for these compounds are listed in Table 3.4.

In order to distinguish between the effects of Mg substitution and Na deficiency, two series of compounds were prepared using the exact same heating schedule. The first series were prepared with the nominal formula $Na_3Na_{1-x}Mg_xIr_2O_6$, and the second series had the nominal formula $Na_{3-\delta}Na_{0.75}Mg_{0.25}Ir_2O_6$. Plots of lattice parameters versus nominal composition demonstrate the influence of both Mg substitution (Fig. 3.5(a)) and Na-deficiency (Fig. 3.5(b)) on the lattice parameters. Substitution of Mg for Na in the honeycomb plane causes the *a*- and *b*-axes to contract, and the *c*-axis to expand slightly. This result supports the assumption that Mg substitutes into the honeycomb plane, as substitution between the planes would cause the *c*-axis to contract due to electrostatics and the reduced size of Mg relative to Na. Similarly, Na-deficient samples show a contraction of the *a*- and *b*-axes and an expansion of the *c*-axis. Because both Na and Mg contents are variable, compounds in the $Na_{3-\delta}(Na_{1-x}Mg_x)Ir_2O_6$ series have a broad range of possible unit cell parameters.

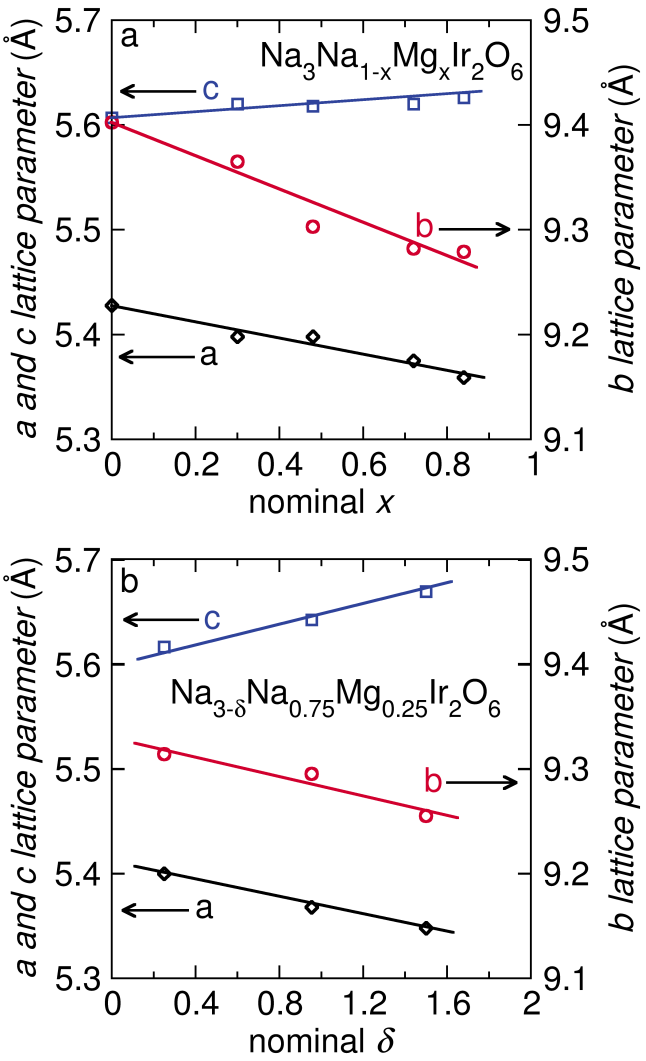

Figure 3.5: Plots of lattice parameters vs. nominal chemical composition for the cases of varied Mg substitution ($Na_3(Na_{1-x}Mg_x)Ir_2O_6$) **(a)** and varied Na-content ($(Na_{3-\delta}(Na_{0.75}Mg_{0.25})Ir_2O_6$) **(b)**. Substitution of Mg for Na in the honeycomb plane causes the *a*- and *b*-axes (black diamonds and red circles, respectively) to contract and the *c*-axis (blue squares) to expand. Decreasing the amount of sodium in the lattice has a similar effect.

3.5 Magnetic Properties

To investigate the influence of lattice geometry on the magnetic properties of the A_2IrO_3 family, zero-field-cooled (ZFC) magnetization data were collected under an applied magnetic field of $\mu_0 H = 1$ T on each of the compounds in the $Na_{3-\delta}(Na_{1-x}Mg_x)Ir_2O_6$ series. Fig. 3.6 shows plots of inverse magnetic susceptibility ($\chi^{-1} \approx \frac{H}{M}$) versus temperature for all compounds studied in this work. Datasets are staggered along the y-axis for visibility. Linear fits to the data in the paramagnetic regime ($T > 60$ K) yield the Curie constant C, the Weiss temperature θ_W, and the temperature-independent susceptibility χ_0 (Table 3.5). θ_W, a measure of the average magnetic interaction strength, is negative for all members of the series, indicating that antiferromagnetic interactions dominate in these materials. Fig. 3.7 shows a plot of θ_W versus the average nearest neighbor Ir–Ir distance for all members of the $Na_{3-\delta}(Na_{1-x}Mg_x)Ir_2O_6$ series. There is a clear trend in the magnitude of θ_W as a function of Ir–Ir distance, illustrated with a solid red line. Contraction of the honeycomb plane results in a decrease in the magnitude of θ_W. The change in interaction strength is likely due to modulation of the Ir–O–Ir bond angles, which become narrower as the lattice contracts. Contraction of the lattice causes these angles to decrease, resulting in increased ferromagnetic exchange and a concomitant decrease in the magnitude of θ_W. To illustrate this effect, the average Ir–O–Ir bond angles at $T = 5$ K are given on the plot for the two samples that were analyzed via NPD, along with the average of the two angles reported for Na_2IrO_3 [34].

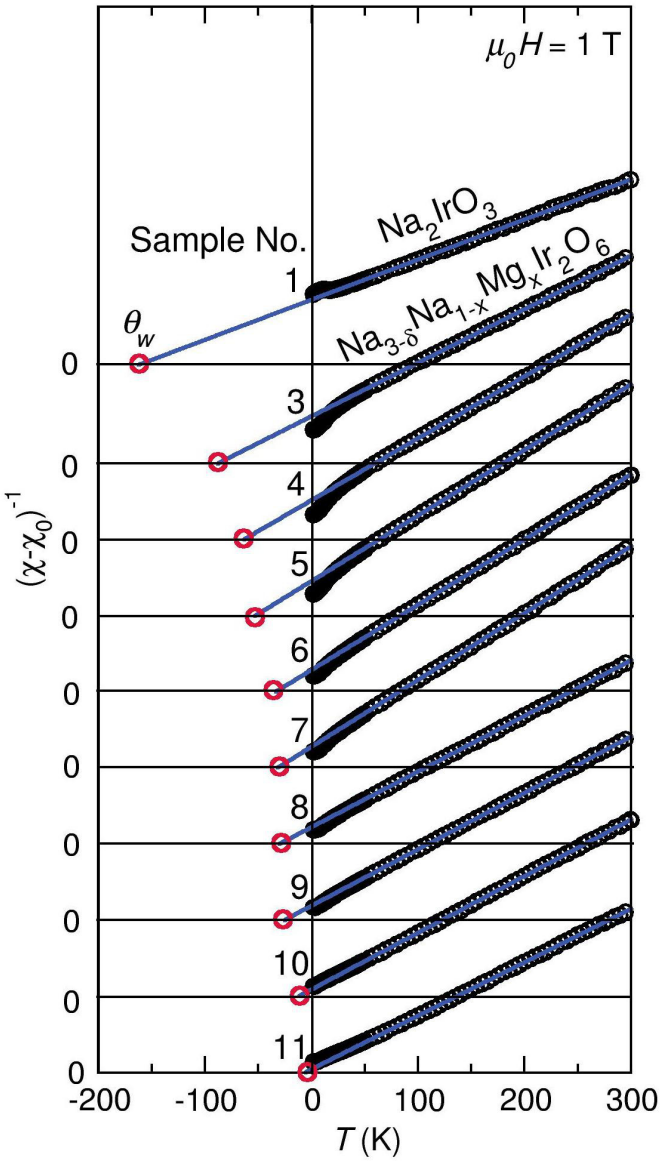

Figure 3.6: Inverse magnetic susceptibility is plotted against temperature for each member of the series. Datasets are shifted along the y-axis for visibility. Linear fits to inverse magnetic susceptibility data over the range $T = 60$ K to 300 K yield the Curie constant C and the Weiss temperature θ_W for each member of the series. Datasets are shifted along the y-axis for visibility. The Weiss temperatures θ_W for each member of the series are indicated by red circles, corresponding to the x-intercept of the linear extrapolation from the Curie-Weiss regime.

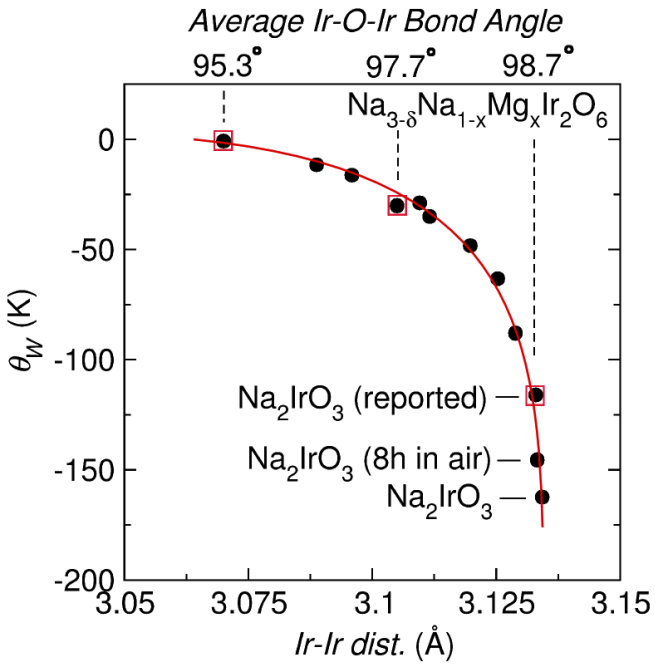

Figure 3.7: Plot of the Weiss temperature θ_W versus the average nearest neighbor Ir–Ir distance for all compounds studied in this work. Negative values of θ_W indicate that antiferromagnetic interactions dominate the magnetic susceptibility of these layered honeycomb iridates, and the magnitude of θ_W is a measure of the strength of these interactions. Expansion of the honeycomb plane increases the overall antiferromagnetic interaction strength as Ir–O–Ir bond angles deviate from 90°. Average Ir–O–Ir bond angles, determined from analysis of NPD data, are shown for two points on the plot, as well as the reported value for Na_2IrO_3, denoted by red boxes [34]. θ_W is largest in Na_2IrO_3 and is diminished by chemical substitution and sodium vacancies, as well as decomposition in air. The smooth curve through the data is a guide to the eye.

Table 3.5: Curie-Weiss parameters determined from linear least-squares fitting to inverse magnetic susceptibility data in the paramagnetic regime.

Sample No.	*Target Stoichiometry*	χ_0 ($\frac{emu}{molIr \cdot K}$)	C ($\frac{emu \cdot K}{molIr \cdot Oe}$)	θ_W (K)	Ir^{3+}:Ir^{4+} (± 0.1)
1	$Na_3NaIr_2O_6$	$1.1(6) \cdot 10^{-4}$	0.544(3)	-162.4(9)	0:1
2	$Na_3NaIr_2O_6$(8h in air)	$-5(2) \cdot 10^{-7}$	0.338(8)	-146(2)	0.3:0.7
3	$Na_3Na_{0.9}Mg_{0.1}Ir_2O_6$	$-9(1) \cdot 10^{-5}$	0.406(7)	-87(1)	
4	$Na_3Na_{0.8}Mg_{0.2}Ir_2O_6$	$-9(1) \cdot 10^{-5}$	0.345(4)	-63(2)	
5	$Na_{3.06}Na_{0.7}Mg_{0.3}Ir_2O_6$	$-6(1) \cdot 10^{-5}$	0.33(1)	-48(3)	
6	$Na_{3.26}Na_{0.5}Mg_{0.5}Ir2O_6$	$3(1) \cdot 10^{-5}$	0.330(5)	-35(2)	0.4:0.6
7	$Na_{2.5}Na_{0.5}Mg_{0.5}Ir_2O_6$*	$3.7(8) \cdot 10^{-4}$	0.384(8)	-30(1)	0.1:0.9
8	$Na_3Na_{0.52}Mg_{0.48}Ir_2O_6$	$-3.4(6) \cdot 10^{-5}$	0.333(6)	-28(2)	0.3:0.7
9	$Na_{2.56}Na_{0.5}Mg_{0.5}Ir_2O_6$	$-9(1) \cdot 10^{-5}$	0.380(4)	-16(2)	0.1:0.9
10	$Na_{2.46}Na_{0.24}Mg_{0.76}Ir_2O_6$	$-1.2(9) \cdot 10^{-4}$	0.383(9)	-11(1)	
11	$Na_{2.4}MgIr_2O_6$*	$-1.1(7) \cdot 10^{-4}$	0.396(5)	-1(1)	0.2:0.8

Table 3.6: Freezing temperatures T_f, activation energies E_a, and characteristic frequencies ω_0 determined from an Arrhenius analysis of AC magnetic susceptibility data collected on members of the $Na_{3-\delta}(Na_{1-x}Mg_x)Ir_2O_6$ series.

Sample No.	*Target Stoichiometry*	T_f(100 Hz)	E_a (K)	ω_0 (Hz)
5	$Na_3Na_{0.7}Mg_{0.3}Ir_2O_6$	3.8	118(9)	10^{15}
6	$Na_3Na_{0.5}Mg_{0.5}Ir2O_6$	4.8	235(9)	10^{23}
7	$Na_{2.5}Na_{0.5}Mg_{0.5}Ir_2O_6$*	4.9	190(13)	10^{18}
8	$Na_3Na_{0.52}Mg_{0.48}Ir_2O_6$	4.3	155(20)	10^{17}
9	$Na_{2.56}Na_{0.5}Mg_{0.5}Ir_2O_6$	4.1	166(14)	10^{19}
11	$Na_{2.4}MgIr_2O_6$*	3.4	187(11)	10^{25}

The Curie constant C is directly related to the number of Ir^{4+} species in the sample, as Ir^{3+}, Na, and Mg are all diamagnetic. We therefore use both the nominal compositions and the calculated values for C to estimate the ratio of Ir^{3+} to Ir^{4+}, using the compounds whose compositions are known (Na_2IrO_3, $Na_3Mg_{0.5}Ir_2O_6$ and $Na_{2.3}MgIr_2O_6$) as reference points (Table 3.5). It must be noted that in the strong spin-orbit coupling limit there is a substantial orbital contribution to the observed susceptibility of the Ir^{4+} electrons. Nevertheless, these estimates show unambiguously that a significant quantity of low-spin Ir^{3+} can exist as non-magnetic "holes" in A_2IrO_3 honeycomb lattices. This is unsurprising from a chemical standpoint, as the Ir^{3+}/Ir^{4+} redox cycle is well documented in the literature, and has even been studied for use in water oxidation catalysis [39]. It is likely that the reduced Ir species are distributed in a disordered manner throughout the lattice, which would explain the origin of the spin glass-like behavior observed in many low quality Na_2IrO_3 samples.

Samples in the $Na_{3-\delta}(Na_{1-x}Mg_x)Ir_2O_6$ series exhibit spin glass-like behavior. Fig. 3.8 (a) shows AC magnetic susceptibility data collected on $Na_3Mg_{0.5}Ir_2O_6$ and $Na_{2.3}MgIr_2O_6$. In both sets of data there is a broad peak in the real component of the AC susceptibilityχ' at low temperatures, the position T_f and height χ'_{max} of which vary as a function of the frequency ω of the AC field. Analysis of the data in the context of a canonical spin glass using the Vogel–Fulcher law or standard theory for dynamical scaling yield unphysical parameters and therefore little insight [40]. The linear relationship between of $\ln(\omega)$ and $\frac{1}{T_f}$ indicates an Arrhenius–type activation barrier, with activation energies E_a between 100

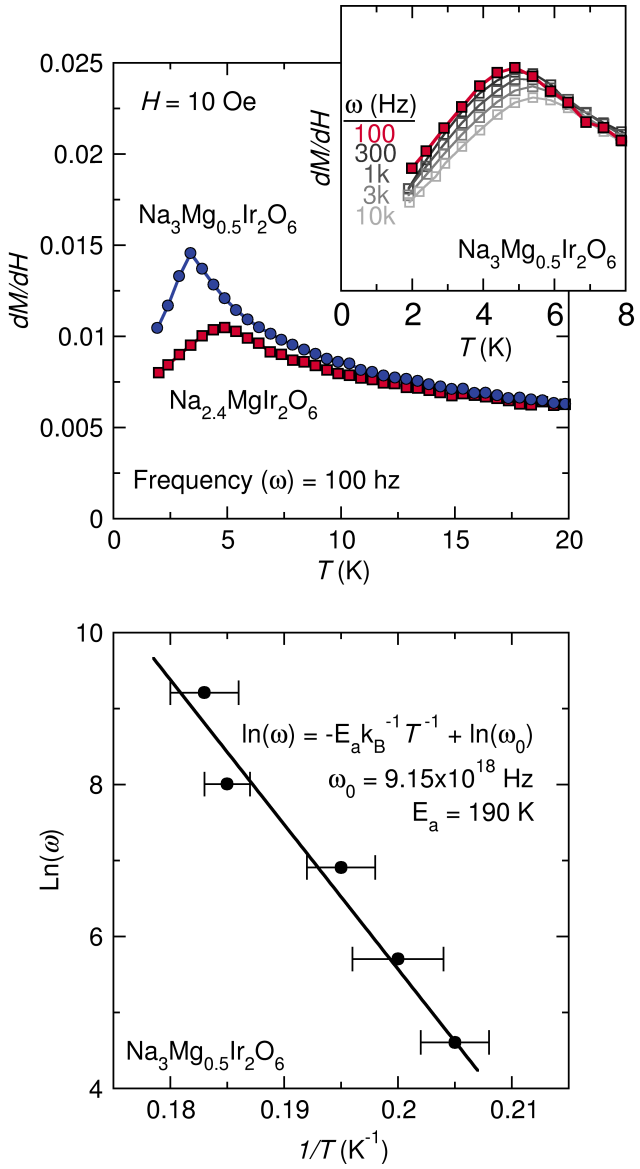

Figure 3.8: **(a)** AC susceptibility data collected on two representative samples from the $Na_{3-\delta}Na_{1-x}Mg_xIr_2O_6$ series under an applied field of $H = 796$ A/m (10 Oe) with amplitude of $H = 398$ A/m (5 Oe). Both samples show a peak in the real component χ' of the AC susceptibility at the freezing temperature T_f, and the magnitude of the peak decreases and shifts to higher temperatures as the frequency of the AC field is increased, consistent with a spin glass-like transition (inset). **(b)** A plot of $\ln(\omega)$ versus $\frac{1}{T_f}$ yields a roughly linear dependence, indicating proximity to a super paramagnetic regime, and the slope and intercept of the linear fit yield activation energy E_a and the characteristic frequency ω_0 for spin reorientation.

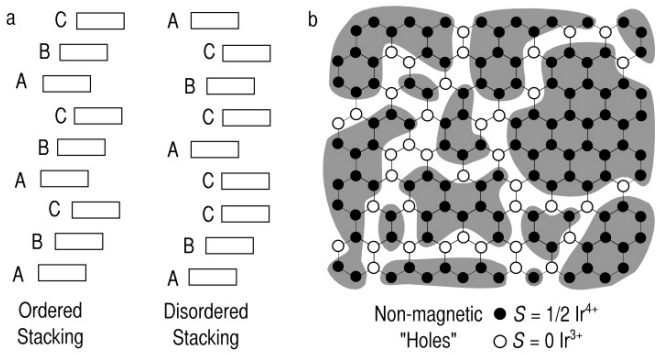

Figure 3.9: Common types of disorder in A_2IrO_3 honeycomb iridates. **(a)** In a fully ordered sample, honeycomb layers are stacked in a perfectly repeating pattern (ABCABCABC, for example). Stacking faults (ABCCACBCA, here) complicate structural characterization as they masquerade as (Na/Mg) mixing onto the Ir site. **(b)** Non-magnetic Ir^{3+} also exist due to chemical defects. These "holes" perturb the magnetic order in A_2IrO_3 materials, and can lead to the disordered freezing of spins commonly observed in polycrystalline samples. We speculate that this type of disorder leads to the formation of isolated "islands" of AFM order, which vary in size and interact weakly with one another, which is one possible explanation for the pseudo–superparamagnetic behavior observed in AC magnetic susceptibility measurements.

K and 300 K and characteristic frequencies ω_0 on the scale of 10^{15} Hz to 10^{25} Hz [41] (Fig. 3.8 (b)). While these large values, located in Table 3.6, are clearly unphysical, they do imply that the frozen, disordered magnetic state observed in these and other iridates is closer to superparamagnetism than to spin glass. This implication is best understood by considering the two major sources of disorder in honeycomb iridates: stacking faults (Fig. 3.9(a)) and non-magnetic Ir^{3+} "holes" (Fig. 3.9(b)). Stacking faults occur due to the negligible energy difference between all possible stacking arrangements, but may have little influence on magnetic order because exchange interactions between neighboring layers are small compared to the interactions within each two dimensional layer. Non-magnetic Ir^{3+} "holes" are also likely to exist due to the ease with which Ir^{4+} can be reduced. This type of defect, in contrast to stacking faults, can have a significant effect on magnetic order even at low levels, as it gives rise to the possibility of isolated antiferromagnetic domains [29]. Such a picture could explain the apparent proximity to a superparamagnetic state which in fact arises due to a distribution of local AF domain sizes.

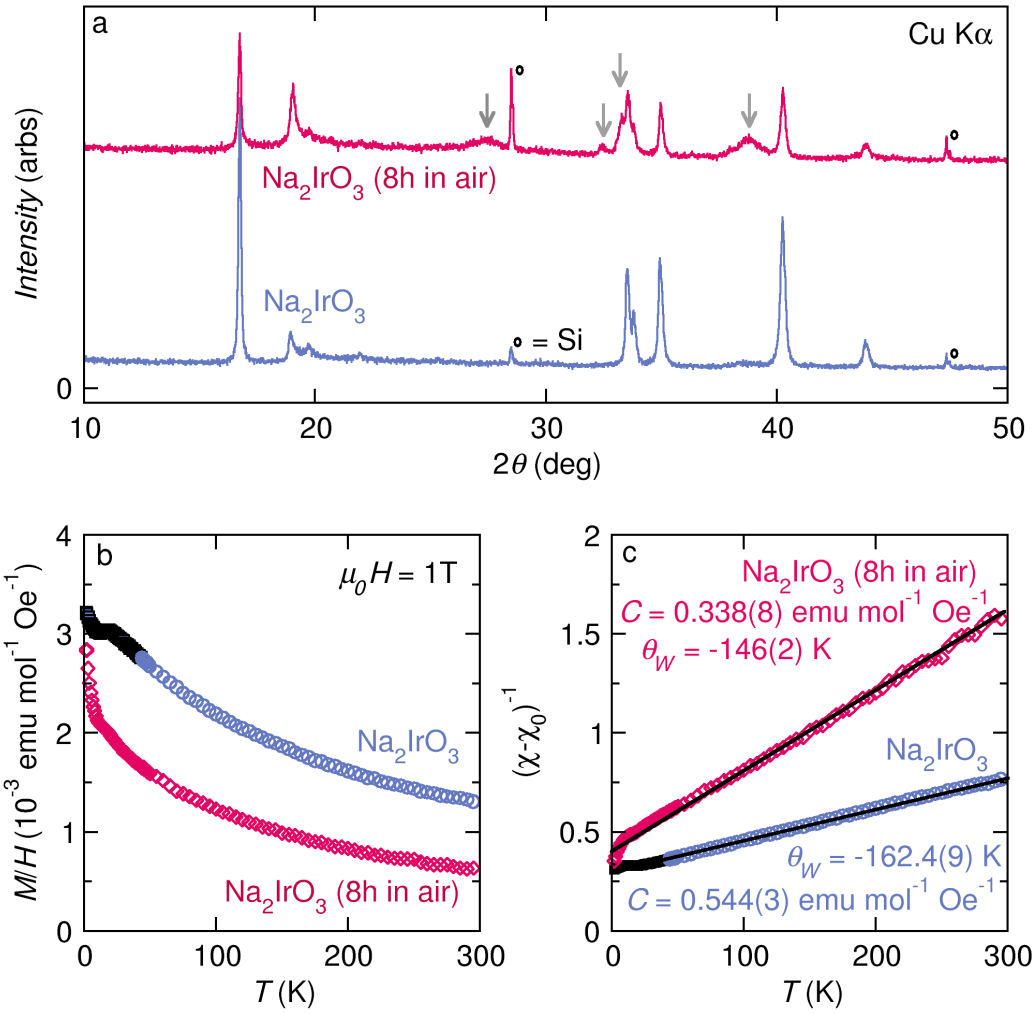

Figure 3.10: **(a)** XRPD data collected over the 2θ range 10° to 50° in six minutes on Na_2IrO_3 immediately after removal from an argon-filled glovebox (blue, bottom) and after eight hours of exposure to laboratory air (red, top). A reaction occurs between Na_2IrO_3 and one or more components of the air that causes the relative intensities of the C2/*m* reflections to change, and new reflections emerge, highlighted with gray arrows. Small circles indicate reflections due to crystalline Silicon, which was used as an internal standard for the purpose of Rietveld refinement. **(b)** The magnetic susceptibilities of polycrystalline Na_2IrO_3 (blue circles) and the same powder after eight hours of exposure to air at room temperature (red diamonds) are compared. When handled in air-free conditions, Na_2IrO_3 exhibits long-range AFM order, as evidenced by the local maximum in the magnetic susceptibility at T_N = 15 K. **(c)** A plot of inverse magnetic susceptibility versus temperature, along with linear fits to both datasets above T = 60 K yield the Weiss temperature θ_W and Curie constant C for Na_2IrO_3 before (blue circles) and after (red diamonds) exposure to air.

Fig. 3.10 (a) shows XRPD data collected over the 2θ range 10° to 50° in six minutes on a nearly pristine sample of Na_2IrO_3, collected immediately upon removal from an argon-filled glovebox, where the sample was ground and prepared after heating at 900 °C. XRPD data collected on powder from the same sample after eight hours of exposure to laboratory air show significant changes in the relative intensities of the Bragg peaks, as well as the development of broad new peaks, however there is only a minor change in the lattice parameters of the Na_2IrO_3 unit cell over this time period. In contrast, the magnetic properties are significantly affected by the reaction. When handled properly, polycrystalline Na_2IrO_3 exhibits long range AFM order, as evidenced by the local peak in the magnetic susceptibility data below T_N = 15 K (Fig. 3.10(b)). After eight hours of exposure to air, there is no such local maximum. Curie-Weiss fitting to the linear region of the data above T = 60 K shows that θ_W decreases substantially as a result of the reaction (Fig. 3.10(c)). The Curie constant also decreases significantly, suggesting that the average oxidation state of Ir is changing as a result of the reaction, resulting in fewer $S = \frac{1}{2}$ Ir^{4+} species. The fact that the lattice parameters of the Na_2IrO_3 cell do not change significantly as a result of exposure to air suggests that this is not simply a result of hydration, as one might expect from experience with structurally analogous systems [42]. The appearance of new peaks suggests that a chemical reaction is occurring between one or more components of laboratory air and Na_2IrO_3, a possibility that was very recently explored in detail [51]. This result suggests the origin of the discrepancy between magnetic data collected on single crystalline and polycrystalline samples: the small surface area to volume ratio of single crystalline samples hinders the reaction, leaving much of the sample's bulk unreacted. Unfortunately, this implies that previous studies on the magnetic properties and structure of single-crystalline Na_2IrO_3 may have yielded inaccurate data due to sample inhomogeneity.

3.6 Conclusions

A new series of compounds based on the A_2IrO_3 prototype with the formula $Na_{3-\delta}(Na_{1-x}Mg_x)Ir_2O_6$ ($0 \leq x \leq 1$) were synthesized and characterized using NPD, XRPD, ICP-OES, and magnetometry. Substitution of Mg for Na results in contraction of the *a*- and *b*-axes and expansion of the *c*-axis, suggesting that Mg substitution occurs primarily in the honeycomb plane. Similarly, Na deficiency between honeycomb planes contracts the *a*- and *b*-axes and expands the *c*-axis. All samples exhibit stacking disorder, which complicates structural characterization. Magnetic data collected on the compounds studied in this series suggest that there are two main variables that determine the magnetic properties of compounds in the A_2IrO_3 family: (1) the strength of the magnetic superexchange interactions between neighboring $S = \frac{1}{2}$ Ir^{4+} species is dependent on the angle of the Ir–O–Ir bonds, for which the in plane lattice parameters *a* and *b* are a good structural marker, and (2) the number of $S = \frac{1}{2}$ Ir^{4+} sites is influenced by the chemical composition of the compound because the oxidation state of Ir is variable. This demonstrates that chemical defects can lead to significant numbers of non-magnetic "holes", which are likely the root of the pseudo-superparamagnetic behavior observed in many polycrystalline samples. We further showed that Na_2IrO_3 reacts quickly with laboratory air, producing significant changes in its magnetic behavior, and reported magnetic data on high-quality polycrystalline Na_2IrO_3, which shows long-range AFM order. Together, our results demonstrate that defects and disorder have significant effects of the magnetism of the A_2IrO_3 family, and that these materials can be chemically tuned to in order to explore experimentally what may prove to be a rich magnetic phase diagram.

3.7 Acknowledgements

Acknowledgement is made to the donors of the American Chemical Society Petroleum Research Fund and the David and Lucille Packard Foundation for support of this research.

4 New Honeycomb Iridium (V) Oxides: $NaIrO_3$ and $Sr_3CaIr_2O_9$.

This work was co-written with the following authors and is published under
the following citation:
Dalton Trans. **44**, 20344-20351 (2015)
http://dx.doi.org/10.1039/C5DT03188E

David C. Wallace,[a,b] and Tyrel M. McQueen[a,b,c,*]
[a]Department of Chemistry, The Johns Hopkins University, Baltimore, MD, USA
[b]Institute for Quantum Matter, The Department of Physics and Astronomy,
The Johns Hopkins University, Baltimore, MD, USA
[c]Department of Materials Science and Engineering,
The Johns Hopkins University, Baltimore, MD, USA
[*]Corresponding Author

4.1 Abstract

We report the structures and physical properties of two new iridates, $NaIrO_3$ and $Sr_3CaIr_2O_9$, both of which contain continuous two-dimensional honeycomb connectivity. $NaIrO_3$ is produced by room temperature oxidative deintercalation of sodium from Na_2IrO_3, and contains edge-sharing IrO_6 octahedra that form a planar honeycomb lattice. $Sr_3CaIr_2O_9$, produced *via* conventional solid-state synthesis, hosts a buckled honeycomb lattice with novel corner-sharing connectivity between IrO_6 octahedra. Both of these new compounds are comprised of Ir^{5+} ($5d^4$) and exhibit negligible magnetic susceptibility. They are thus platforms to investigate the origin of the nonmagnetic behavior exhibited by Ir^{5+} oxides, and provide the first examples of a $J = 0$ state on a honeycomb lattice.

4.2 Introduction

Research into 5d transition metal compounds has blossomed in recent years due to the potential for new electronic and magnetic phenomena to emerge from the interplay between crystal field effects, electronic correlations (Hubbard U) and strong spin-orbit coupling (SOC). Iridium is an appealing element in which to study these physics due to its tendency to adopt a 4+ oxidation state, where the ground electronic configuration $5d^5$ is predicted to yield a $J = \frac{1}{2}$ electronic state in the presence of strong SOC [24]. Further, iridates are known to crystallize in numerous structure types, each with unique Ir-Ir connectivity, and this fact has made them an active area of study[33, 43–45]. In aggregate, recent literature on the magnetic and electronic properties of iridates are unified by a desire to probe the influence of strong SOC and U on electronic behavior[46]. Iridium–based honeycombs, in particular the A_2IrO_3 (A = Li/Na) family, have fallen under intense scrutiny following predictions that they might host a spin-liquid ground state[25–32]. Efforts to produce new iridium oxide honeycomb lattices have intensified[47–49], but 4d and 5d materials containing continuous honeycomb connectivity remain scarce.

Here we report the synthesis and characterization of two new honeycomb iridates based

on Ir^{5+} ($5d^4$). The first, $NaIrO_3$ is produced via *chimie douce* oxidative deintercalation of sodium from Na_2IrO_3, which preserves the planar honeycomb network of edge-sharing IrO_6 octahedra. The second, $Sr_3CaIr_2O_9$, is a 2:1 ordered perovskite, which shares its structure with $Sr_3CaRu_2O_9$[50], and consists of layers of IrO_6 octahedra forming a buckled honeycomb lattice. Magnetic susceptibility data collected on both compounds demonstrate weak temperature-independent magnetism, and resistivity measurements show semiconducting behavior consistent with hopping conductivity. These compounds are thus ideal to investigate the interplay between non-cubic crystal fields and SOC. By comparison with related 4d and 5d honeycomb compounds with partially filled t_{2g} subshells, we find that d electron count correlates strongly with the magnetic behavior, and present a thorough structural analysis of $Sr_3CaIr_2O_9$ and $Sr_3CaRu_2O_9$ that ultimately suggests the correlation is driven by SOC.

4.3 Results

4.3.1 Syntheses and Structures

Polycrystalline Na_2IrO_3 was prepared *via* previously reported methods[51]. $NaIrO_3$ was prepared *via* the oxidative deintercalation reaction:

$$Na_2IrO_3 + \frac{x}{2}\,Br_2 \underset{\text{Acetonitrile}}{\longrightarrow} (1-x)\,Na_2IrO_3 + x\,NaIrO_3 + x\,NaBr. \tag{29}$$

Polycrystalline Na_2IrO_3 was removed from the glovebox and immediately combined on the benchtop with a stock solution of elemental Bromine (Sigma–Aldrich, 99.99%) in acetonitrile (Fischer Scientific, HPLC grade). The progress of the reaction was monitored visually by observing a disappearance of color the from oxidant solution, and was presumed to be complete when the color reached a steady state or disappeared completely, depending on the targeted product stoichiometry. Upon reaching completion, the fine, black, polycrystalline product was collected *via* vacuum filtration and rinsed several times with fresh

acetonitrile to remove crystalline NaBr. The 1:1 relationship between oxidant consumption and Na^+ deintercalation of equation 1 was confirmed by laboratory X-ray powder diffraction (XRPD) data collected on powders after vacuum evaporation of the solvent, which showed crystalline NaBr as the only side product. In contrast to the precursor material Na_2IrO_3 which degrades rapidly in laboratory air [51], $NaIrO_3$ is stable under ambient conditions, as XRPD data showed no evidence of decomposition after several months of air exposure. However, $NaIrO_3$ degrades rapidly upon heating above 200°C in air, as evidenced by the broadening of diffraction peaks and appearance of new reflections. Attempts at producing intermediate stoichiometries (i.e. $Na_{2-x}IrO_3$) were unsuccessful, and instead produced two-phase samples containing a mixture of Na_2IrO_3 and $NaIrO_3$. Further, no phase width was observed in $NaIrO_3$, as reactions performed with excess bromine produced only $NaIrO_3$ with no observable difference in lattice parameters or physical properties.

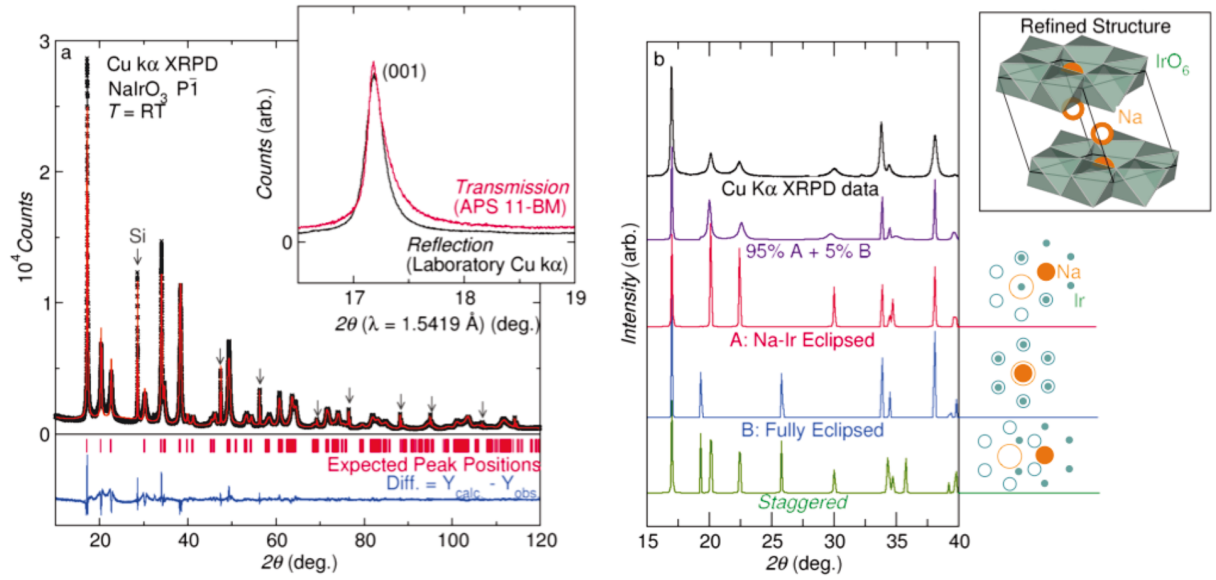

Figure 4.1: **a)** Laboratory XRPD data (black) collected on $NaIrO_3$ along with Rietveld refinement of the structure in $P\bar{1}$ to the data (red) and calculated difference between the model and the data (blue) are shown in the main frame. Stacking faults between honeycomb layers complicate the refinement, as can be seen from the missed intensities and peak shape mismatches between $2\theta = 15°$ to $35°$. In the inset, the observed profile of the (001) peak, as observed by laboratory XRPD data collected in reflection geometry, is compared to the profile observed from synchrotron XRPD data collected on APS 11-BM in transmission geometry. **b)** Laboratory XRPD data (black, top) along with simulations for three distinct stacking arrangements of adjacent $NaIr_2$ honeycomb layers (red, blue and green) are shown. A fourth simulation (purple) shows the pattern that results from having a 95% probability of an Na–Ir eclipsed stacking arrangement with a 5% probability of a fully eclipsed stacking fault, which provides a good description of the observed diffraction pattern. In the upper right-hand corner the structure of $NaIrO_3$ is shown, in which IrO_6 octahedra (green) share edges to form honeycomb layers with Na cations (orange) occupying the honeycomb "holes" and partially occupying the spaces sandwiched between Na and Ir sites in the honeycomb layers.

The structure of $NaIrO_3$ was solved in space group $P\bar{1}$ *via* Rietveld refinement to laboratory XRPD data (Fig. 4.1(a)). Final structural parameters are listed in table 4.1. Solution of the structure in higher symmetry cells was prevented by the high degree of inter-plane stacking disorder, which arises due to the fact that there are several possible translations that can take place in the honeycomb plane from one layer to another, each of which generates a different stacking pattern at minimal energetic cost. Stacking disorder is a well known structural perturbation in many layered compounds, and evidence of this disorder can be plainly seen in the poorly-fit peak broadening and incorrect intensities present at low diffraction angles. Further evidence of this structural disorder is provided by synchrotron XRPD data (Fig. 4.1 (a, inset)), which show highly asymmetric $\langle 0\ 0\ l \rangle$ peaks– this may occur as a consequence of decomposition in the intense synchrotron beam. Using DIFFaX[53], we modeled the diffraction patterns for three distinct stacking variants. When viewed from perpendicular to the honeycomb plane, these stacking variants can be described based on which atoms in the honeycomb plane eclipse (sit directly above) the Na ion in the adjacent plane. The three primary stacking possibilities are: 1) Na-Ir eclipsed; 2) Na-Na fully eclipsed, which produces infinite Na channels; 3) staggered, in which none of the atoms in the honeycomb plane eclipse those in the adjacent plane, which is the pattern adopted by the parent material Na_2IrO_3. The simulated diffraction patterns for these stacking arrangements, along with XRPD data collected on a sample of Na_2IrO_3 are shown in figure Fig. 4.1(b). The observed XRPD pattern closely resembles the simulation obtained for the Na-Ir eclipsed variant, but with noticeable broadening and attenuation of several peaks. A fourth pattern was simulated based on a model consisting of 95% Na-Ir eclipsed stacking with a 5% probability of a fully-eclipsed stacking fault. This model produces a good qualitative agreement with the raw XRPD data, suggesting that the fully eclipsed stacking variant may only be slightly less energetically favorable than the Na-Ir eclipsed variant. The presence of the fully eclipsed stacking fault suggests that further synthetic work may yield control over stacking order in this compound. For an in-depth discussion

on stacking disorder in honeycomb iridates, see ref. [54]. This is the second known structure with the formula $NaIrO_3$-a post-perovksite structure with the same formula is obtained when synthesized under high-pressure and temperature [55]. Neither structural polymorph of $NaIrO_3$ can be synthesized using conventional solid-state techniques, a fact that underscores the novelty and relative instability of the Ir^{5+} oxidation state.

Table 4.1: Structural parameters for $NaIrO_3$ obtained from Rietveld refinement to laboratory XRPD data.

$NaIrO_3$	($P\bar{1}$ (2))	T = RT			
a (Å)	b (Å)	c (Å)	α (°)	β (°)	γ (°)
5.2808(3)	5.2870(3)	6.0014(3)	90.002(9)	115.762(6)	60.112(5)
	Atom	Wyckoff Site	x, y, z	occ.	$100\times U_{iso}$
	Ir1	(2i)	0.1641(5), 0.1562(6), 0.0098(2)	1	0.16(2)
	Na1	(1e)	$\frac{1}{2}$, 0, $\frac{1}{2}$	1	0.47(9)
	Na2	(2i)	0.210(4), 0.663(4), 0.563(2)	0.5(1)	0.47(9)
	O1	(2i)	0.948(2), 0.468(2), 0.153(2)	1	1.1(1)
	O2	(2i)	0.239(2), 0.844(2), 0.206(3)	1	1.1(1)
	O3	(2i)	0.639(3), 0.103(3), 0.190(2)	1	1.1(1)
				χ^2	3.70
				R_{wp}	10.65
				R_p	8.00

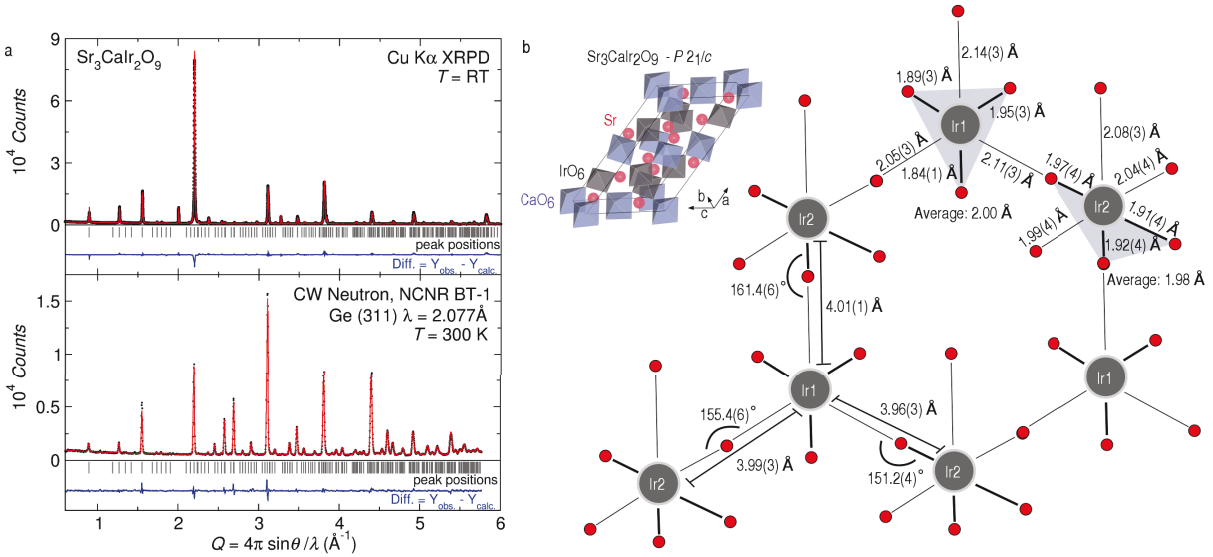

Figure 4.2: **a)** Rietveld refinement of the structure of $Sr_3CaIr_2O_9$ to laboratory XRPD data (top) and NCNR BT-1 NPD data (bottom) are shown. Data points are displayed in black, the fit in orange, and the difference between the data and fit, blue. Expected peak positions for the monoclinic cell are displayed as gray tick marks below the data in each pane. **b)** The unit cell of $Sr_3CaIr_2O_9$ is displayed along with a cutout of the honeycomb network formed by corner-sharing IrO_6 octahedra in the a-b plane. Ir–Ir distances and Ir–O–Ir bond angles are shown in the bottom left of the honeycomb structure, and Ir–O bond lengths for each of the two iridium sites are shown in the upper right hand corner. Despite the uniformity of the Ir–Ir distances in the honeycomb lattice, the IrO_6 octahedra exhibit significant asymmetric distortions, and these distortions are illustrated by gray triangles in the plane formed by the three most closely bonded oxygen atoms of each octahedron. These distortions are inconsistent with a Jahn-Teller effect, and instead are likely driven by strong SOC of the Ir^{5+} ion as described in the text.

Polycrystalline $Sr_3CaIr_2O_9$ was prepared *via* conventional solid state synthesis: $SrCO_3$ (NOAH Technologies, 99.9%), $CaCO_3$ (NOAH Technologies, 99.98%) and IrO_2 (J&J Materials, 99%) were ground thoroughly in an agate mortar and pestle, heated in a capped alumina crucible to 750°C at 200°C/hr, held at temperature for 12 hours, and then furnace-cooled to room temperature. The powder was then reground and pelletized, heated to 1050°C at 200°C/hr in the same uncapped crucible, held at temperature for 80 hours, and then furnace-cooled to room temperature.

The structure of $Sr_3CaIr_2O_9$ was solved in space group $P2_1/c$ (14) *via* Rietveld refinement to neutron powder diffraction (NPD) and XRPD data (Fig. 4.2 (a)), and was found to be isostructural to $Sr_3CaRu_2O_9$[50]. Final structural parameters are listed in table 4.2. The monoclinic structure of $Sr_3CaIr_2O_9$, visible in Fig. 4.2 (b), can be described as a 2:1 ordered perovskite with the formula $A_3BB'_2O_9$, where IrO_6 and CaO_6 octahedra share corners to form the perovskite lattice and Sr^{2+} cations occupy the 12-fold coordinate A sites. In contrast to the $Ba_3MIr_2O_9$ (M = Mg, Ca, Sc, Ti, Zn, Sr, Zr, Cd, In, etc.) family of 6H-perovskite-like structures, which host face-sharing Ir_2O_9 dimers[56], the IrO_6 octahedra of $Sr_3CaIr_2O_9$ share corners to form a buckled honeycomb lattice in the b–c plane. While the structure of $Sr_3CaIr_2O_9$ may seem odd given the apparent wealth of other Barium-based compounds with analogous stoichiometry, it is actually unsurprising that a conventional perovskite lattice is formed in this case due to the improved match in ionic radii between Sr and Ir. The same is true of $Sr_3CaRu_2O_9$, which also has a similar collection of Ba-based 6H-perovskite-type cousins. While many different perovskites containing iridium have been reported in addition to the widely studied Sr_2IrO_4, this seems to be a rare example of an iridium-based perovskite containing honeycomb connectivity. Furthermore, the corner-sharing bonding motif of the honeycomb lattice is the first of its kind in iridates, and thus opens a new avenue along which to search for new honeycomb materials that are free from stacking disorder and are air–stable.

The corefinement of the $Sr_3CaIr_2O_9$ structure to both XRPD and NPD data yielded sta-

ble oxygen positions that can be used to investigate the honeycomb connectivity in detail (Fig. 4.2 (b)). As a result of octahedral tilting, the Ir–O–Ir bond angles between nearest-neighbor sites on the honeycomb lattice are significantly less than the ideal 180° expected for an undistorted perovskite. The Ir–O bond lengths are also distorted: for the first iridium site, three adjacent Ir–O bonds are significantly shorter than the overall average of 1.99 Å, while the opposite three are significantly longer. A similar "three short, three long" pattern is also observed to a lesser degree on the second iridium site, where the three short bonds form a plane that is roughly perpendicular to the plane formed by the longer three bonds. This pattern results in significant variations in the bridging Ir–O–Ir bond lengths: the shortest Ir–Ir distance (3.96(3) Å) is formed via Ir–O bonds of very similar lengths (2.04(4) & 2.05(3) Å, respectively), while the longest (d_{Ir-Ir} = 4.01(1) Å) is formed via Ir–O bonds of very disproportionate lengths (2.14(3) & 1.92(4) Å, respectively). These non-uniform exchange interactions result in an effective dimerization between Ir sites even though the distances between adjacent iridium sites on the honeycomb lattice are remarkably similar. These observations are consistent with a non-spherical perturbation to the d-electron states of Ir 5+ , which will be discussed in detail in the next section.

4.3.2 Physical Properties

Fig. 4.3 shows magnetic susceptibility data collected on $NaIrO_3$ and $Sr_3CaIr_2O_9$, along with linear fits to the χ_0-corrected inverse susceptibilities (inset). In contrast to Na_2IrO_3, which has a magnetic moment of 2.0(1) μ_B per Ir site and a Weiss temperature θ_W = -159(3) K, honeycomb $NaIrO_3$ shows only a small temperature-independent susceptibility $\chi_0 = 3.29\times10^{-4}$ emu/mol Ir in the high temperature regime and a Curie tail at low temperatures. A Curie-Weiss fit to the magnetic susceptibility data (Fig. 4.3 (inset)) yields a Curie constant of C = $4.3(1)\times10^{-3}$ emu/mol Ir K, and a Weiss temperature θ_W = 0(2) K. Similar magnetic behavior is observed in $Sr_3CaIr_2O_9$ (Fig. 4.3). $Sr_3CaIr_2O_9$ was initially obtained as a phase-pure powder after 6 short heatings, and a Curie-Weiss fit to the magnetic suscep-

Table 4.2: Structural parameters for $Sr_3CaIr_2O_9$ obtained from Rietveld refinement to Rietveld refinement to NPD and laboratory XRPD data.

$Sr_3CaIr_2O_9$	($P2_1/c$ (14))	T = 300 K		
a (Å)	b (Å)	c (Å)	β (°)	Volume (Å^3)
17.1476(9)	5.7126(3)	9.8841(6)	125.137(3)	791.7
Atom	Wyckoff Site	x, y, z	occ.	$100\times U_{iso}$
Sr1	(4e)	0.254(2), 0.536(2), 0.750(2)	1	1.83(7)
Sr2	(4e)	0.417(1), 0.026(3), 0.080(2)	1	1.83(7)
Sr3	(4e)	0.921(1), 0.524(3), 0.089(2)	1	1.83(7)
Ca1	(2a)	0, $\frac{1}{2}$, $\frac{1}{2}$	1	1.28(3)
Ca2	(2d)	$\frac{1}{2}$, 0, $\frac{1}{2}$	1	1.28(3)
Ir1	(4e)	0.167(1), 0.995(3), 0.836(1)	1	1.25(8)
Ir2	(4e)	0.326(1), 0.499(3), 0.158(2)	1	1.25(8)
O1	(4e)	0.434(1), 0.027(3), 0.622(3)	1	1.64(5)
O2	(4e)	0.882(1), 0.995(4), 0.040(3)	1	1.64(5)
O3	(4e)	0.091(1), 0.734(4), 0.713(3)	1	1.64(5)
O4	(4e)	0.068(1), 0.288(4), 0.178(2)	1	1.64(5)
O5	(4e)	0.412(1), 0.814(4), 0.848(3)	1	1.64(5)
O6	(4e)	0.749(1), 0.793(5), 0.534(2)	1	1.64(5)
O7	(4e)	0.723(1), 0.212(4), 0.988(3)	1	1.64(5)
O8	(4e)	0.383(1), 0.220(4), 0.305(3)	1	1.64(5)
O9	(4e)	0.232(1), 0.501(4), 0.205(3)	1	1.64(5)
			χ^2	1.77
			R_{wp}	5.58
			R_p	4.12

Table 4.3: Comparison of magnetic moments of $NaIrO_3$ and $Sr_3CaIr_2O_9$ with several previously reported Ir^{5+} compounds. With the exception of Sr_2YIrO_6, all compounds exhibit small magnetic moments consistent with a $J = 0$ state in the bulk Ir^{5+} species, where the measured susceptibility is due to a small magnetic impurity or contribution from polycrystalline edge states.

Compound [ref.]	μ_{eff} (μ_B/Ir)
$Sr_3CaIr_2O_9$ (**this work**)	0.18
Honeycomb $NaIrO_3$ (**this work**)	0.18
$Sr_5La_6Ir_4O_{24}$[45]	0.3
Post-perovskite $NaIrO_3$[55]	0.28
$Ba_3ZnIr_2O_9$[62]	0.2
Sr_2YIrO_6[63]	0.91

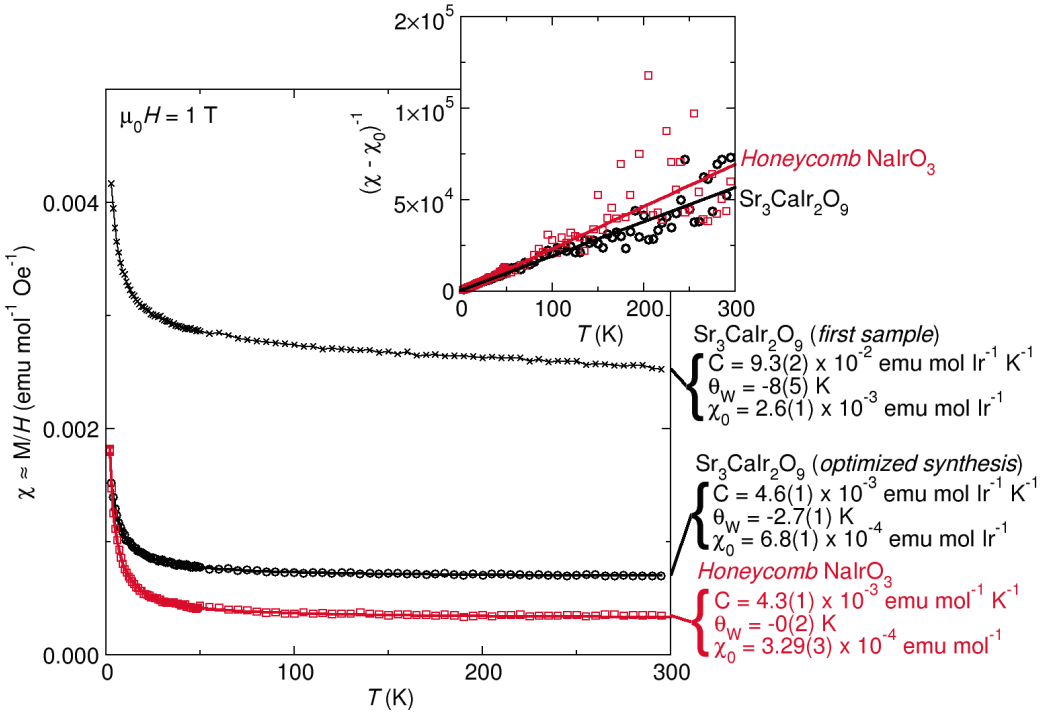

Figure 4.3: Magnetic susceptibility data collected on $NaIrO_3$ (red squares), the first sample of $Sr_3CaIr_2O_9$ (black crosses), and a sample of $Sr_3CaIr_2O_9$ produced *via* an optimized synthetic procedure (black circles) are shown. All magnetic data were collected on polycrystalline samples, and a correction for the temperature-independent susceptibility of the sample holder was applied to the data in order to extract real values of χ_0 for each sample. Two datasets are shown for $Sr_3CaIr_2O_9$ to illustrate that the observed sample χ_0's are due to magnetic defects, the concentration of which can be substantially reduced through correct sample preparation. Linear fits to the χ_0-corrected inverse susceptibility data for $NaIrO_3$ and $Sr_3CaIr_2O_9$, visible in the inset, were used to extract Curie constants C and Weiss temperatures Θ_W for $NaIrO_3$ and the optimized sample of $Sr_3CaIr_2O_9$. Both samples exhibit weak, temperature-independent susceptibility consistent with a small concentration of magnetic defects. These data demonstrate that the Ir^{5+} species in the bulk of both compounds have no unpaired electrons.

tibility data collected on this sample (Fig. 4.3 (inset)) yielded a temperature-independent susceptibility of $\chi_0 = 2.6(1)\times10^{-3}$ emu/mol Ir, a Curie constant C = $9.3(1)\times10^{-3}$ emu/mol Ir K, and a Weiss temperature θ_W = -8(5) K. Optimization of the stoichiometry and heating schedule for $Sr_3CaIr_2O_9$ (See E.S.I.) yielded a sample whose diffraction peaks were significantly sharper and more intense, consistent with an improvement in crystallinity and homogeneity. This improvement resulted in a substantial reduction of C, Θ_W and χ_0 ($4.6(1)\times10^{-3}$ emu/mol Ir K, -8(5) K, and 3.29×10^{-4} emu/mol Ir, respectively). In all samples, the small observed magnetic moments are likely due to dilute magnetic impurities or orphan spins–roughly 1 % of free $S = \frac{1}{2}$ spins in the bulk could account for the observed susceptibility. Furthermore, the small Weiss temperatures observed from all datasets indicate that the magnetic electrons are non-interacting, which lends further weight to the argument for magnetic defects and impurities rather than intrinsic magnetism. These results are thus consistent with a $J = 0$ state in the Ir^{5+} metal centers of both compounds. Furthermore, the magnetic moments observed for Ir^{5+} in these compounds are consistent with what is observed in many other Ir^{5+} compounds (Table 1).

The observed temperature-independent susceptibility is not due to delocalization of charge carriers to form a metal, as is the case in other iridates such as [Rb/K]Ir_4O_8[57, 58]. Fig. 4.4 shows electrical resistivity data collected on polycrystalline bar of $NaIrO_3$ and $Sr_3CaIr_2O_9$. In both datasets, sample resistance increases on cooling, diverging rapidly below $T\sim$100 K, and exceeding the detection limit of the instrument below $T\sim$75 K in the case of $NaIrO_3$. A simple Arrhenius-like activation barrier did not yield a good fit to the resistivity data. Instead, the behavior of both $NaIrO_3$ and$Sr_3CaIr_2O_9$ is well described by a variable-range hopping model. The conductivity is consistent with hopping in two or three dimensions: a plot of $\ln\rho$ vs. $T^{-\frac{1}{3}}$ (Fig. 4(inset)) or $\ln\rho$ vs. $T^{-\frac{1}{4}}$ (not shown) yields a linear relationship. This is similar to what is found for Na_2IrO_3 and indeed many other 4d and 5d honeycombs, and consistent with the materials structure[33, 69].

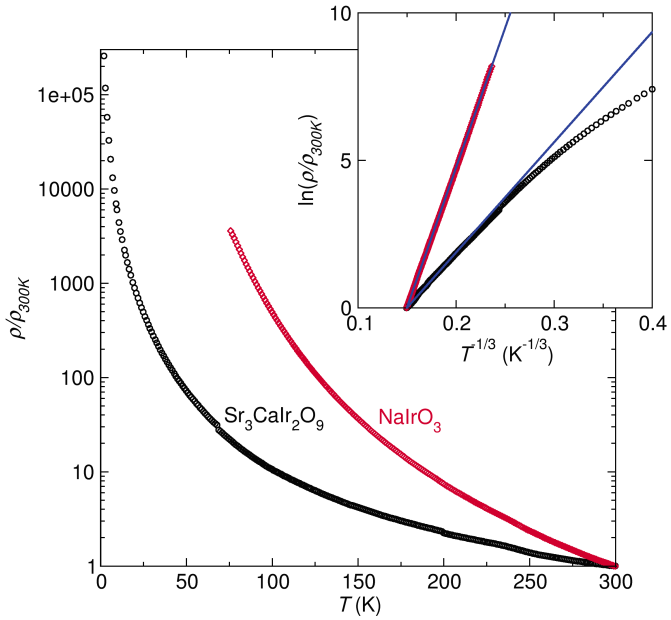

Figure 4.4: Four-probe resistivity data collected as a function of temperature on sintered polycrystalline bars of $NaIrO_3$ (red diamonds) and $Sr_3CaIr_2O_9$ (black circles) are shown. The increase in resistance of the pellets on cooling is a hallmark of electrically insulating materials. In the inset, the natural logarithm of the normalized resistance is plotted as a function of $T^{-\frac{1}{3}}$. Both datasets are linear in this plot in the high-temperature regime consistent with 2-dimensional variable-range hopping of impurity-localized charge carriers.

Table 4.4: Comparison of known 4d and 5d honeycomb compounds organized by connectivity and primary metal ion. Basic magnetic properties are listed for reference.

Type	Compound [ref.]	Connectivity	Electronic configuration	Magnetic Properties
Planar	$SrRu_2O_6$[64, 65]	edge-sharing	$4d^3$	AFM, μ_{eff} = 1.43(1) μ_B
	$Ag_3LiRu_2O_6$[66]	edge-sharing	$4d^4$	Weak, temperature-independent
	$(Li/Na)_2RuO_3$[67]	edge-sharing	$4d^4$	Weak, temperature-independent
	$NaIrO_3$ (**this work**)	edge-sharing	$5d^4$	Weak, temperature-independent
	α–$RuCl_3$[68]	edge-sharing	$4d^5$	AFM, μ_{eff} = 2.2 μ_B
	Li_2RhO_3[69]	edge-sharing	$4d^5$	Spin-glassy AFM , μ_{eff} = 2.0 μ_B
	Li_2IrO_3[70]	edge-sharing	$5d^5$	AFM, μ_{eff} = 2.03 μ_B
	Na_2IrO_3[33]	edge-sharing	$5d^5$	AFM, μ_{eff} = 2.02 μ_B
	Li_2PtO_3[71]	edge-sharing	$5d^6$	Unreported
Harmonic	$^{\mathscr{H}}\langle 1\rangle$-$Li_2IrO_3$[48]	edge-sharing	$5d^5$	Anisotropic, μ_{eff} = 2.03 μ_B
Buckled	$Sr_3CaRu_2O_9$[50]	corner-sharing	$4d^3$	Unreported
	$Sr_3CaIr_2O_9$ (**this work**)	corner-sharing	$5d^4$	Weak, temperature-independent
	thin film $Ca_{0.5}Sr_{0.5}IrO_3$[47]	corner-sharing	$5d^5$	Unreported

4.4 Discussion

Both $NaIrO_3$ and $Sr_3CaIr_2O_9$ are important new additions to a select few 4d and 5d compounds that exhibit honeycomb connectivity between MO_6 octahedra, tabulated in Table 2. For a given d electron count, there is little difference in observed magnetic moments between the 4d and 5d groups, despite the fact that both crystal field and SOC energy scales change significantly when moving down the periodic table. While the magnetic moments observed for the d^5 configurations are unsurprising given the expected magnetic moment of $\mu \sim 1.9\mu_B$ for a $S = \frac{1}{2}$ system, the weak temperature-independent magnetism observed for both $4d^4$ Ru^{4+} and $5d^4$ Ir^{5+} is an unexpected result in the low-spin octahedral crystal field case, which should have 2 unpaired electrons and total spin $S = 1$. Fig. 4.5 shows three possible origins of a nonmagnetic state in an $Ir^{5+}O_6$ ($Ru^{4+}O_6$) octahedron. One possibility is that direct overlap between adjacent Ir sites generates new molecular orbitals, which removes the threefold degeneracy of the t_{2g} manifold and results in a $S = 0$ state, a scenario that has been proposed for Li_2RuO_3 based on the significant variation in Ru-Ru bondlengths[59]. The second possibility is that distortions from perfect octahedral symmetry remove the degeneracy of the t_{2g} manifold locally (*i.e.* a Jahn-Teller distortion), thus resulting in a completely filled, twofold degenerate ground state. Such distortions are thought to be highly important in the Ir^{5+} perovskites $[Sr/Ba]_2IrO_4$, and may also be driven by extended crystal field effects (*i.e.* interactions beyond nearest-neighbor oxygen and iridium atoms)[60, 61]. The final possibility outlined here is that SOC is the strongest perturbation to the cubic crystal field in Ir^{5+}, which is consistent with electronic structure calculations performed by Phelan *et al.* on $Sr_xLa_{11-x}Ir_4O_{24}$[45]. While the computational route invariably leads to the conclusion that SOC produces a nonmagnetic state in Ir^{5+}, one can also reach this conclusion on paper using group theory. To understand how SOC produces a $J = 0$ state in this case, one must generate appropriate term symbols for electronic states in the presence of SOC by referencing the double group for O_h symmetry. In addition to the five irreducible representations of standard character table for group O_h, the

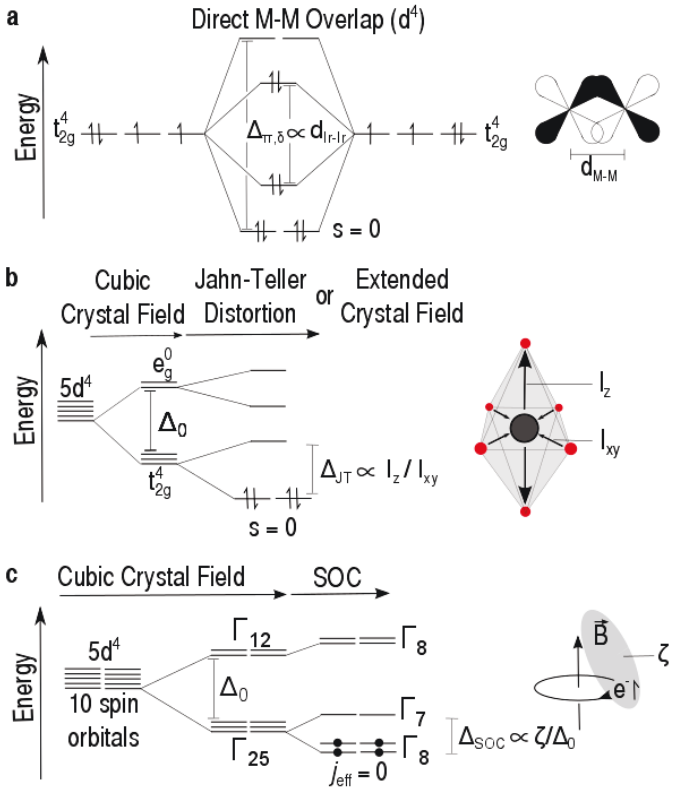

Figure 4.5: Potential origins of $S = 0$ and $J_{\text{eff}} = 0$ states in Ir^{5+} iridates. **a)** Direct π and δ overlap between adjacent iridium sites yields a nonmagnetic ($S = 0$) state by removing the threefold degeneracy of the isolated t_{2g} manifolds. The energy of the splitting, $\Delta_{\pi,\delta}$, is proportional to the distance between adjacent iridium sites, d_{Ir-Ir}. **b)** A local distortion of the cubic crystal field *via* Jahn-Teller distortion or interaction with cations outside the first coordination sphere (extended crystal field) splits the t_{2g} manifold by an energy proportional to the axial elongation (I_z/I_xy), which also yields a $S = 0$ state. **c)** The ground state of the d^4 configuration in a cubic crystal field can be split by SOC to yield a $J = 0$ ground state, which originates from $S = 1$ and $L = 1$ spin and orbital angular momenta. The upper bound to the magnitude of this splitting is proportional to the bare ion SOC constant ξ. relative to the crystal field Δ_0.

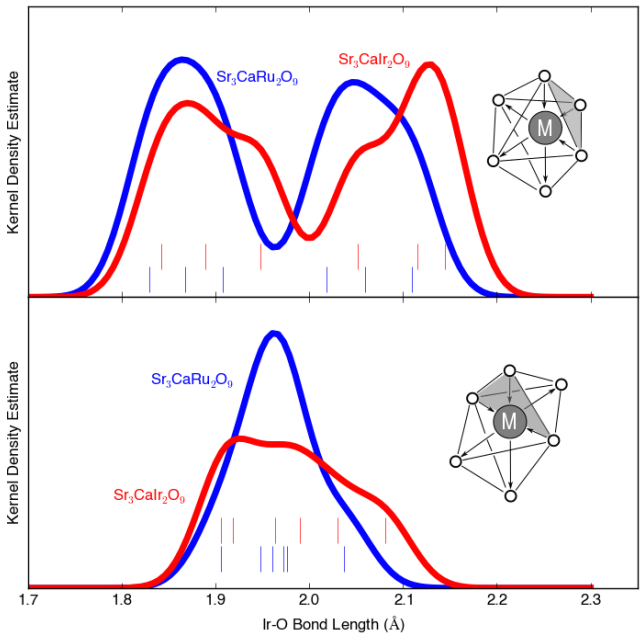

Figure 4.6: Visual comparison of M–O (M = Ir, Ru) bond lengths in $Sr_3CaIr_2O_9$ and$Sr_3CaRu_2O_9$. Gaussian kernel density estimates (KDE) computed on the Ir–O bond lengths present in $Sr_3CaIr_2O_9$ (red) and $Sr_3CaRu_2O_9$ (blue) provide a visual comparison of the octahedral distortions present in both compounds. The top and bottom panes contain data for the 1st and 2nd metal sites in each structure, respectively; in each pane, the solid lines represent KDE's and the small tick marks represent the actual M–O bond lengths. A distinct "3–short, 3–long" bond length pattern is observed in both compounds. Model octahedra in each pane show the shape of the distortion in both cases, with the plane formed by the closely bonded oxygen atoms highlighted in gray.

double group has six new irreducible representations ($\Gamma_6^{+/-}$, $\Gamma_7^{+/-}$, and $\Gamma_8^{+/-}$)[4]. By referencing to the O_h double group, one finds that SOC splits the Γ_{25}^+ (t_{2g}) manifold into two sets of spin orbitals: a twofold degenerate set with Γ_7^+ symmetry and a fourfold degenerate set with Γ_8 symmetry. The Γ_{12}^+ (e_g) manifold is not split in the presence of SOC, but does acquire a new irreducible representation Γ_8^+. Because orbitals from the original Γ_{25}^+ and Γ_{12}^+ manifolds share the same irreducible representations, they interact to form low- and high-energy pairs, akin to bonding and antibonding orbitals in a conventional MO diagram. The net result for the d^4 case is a completely filled Γ_8^+ manifold, which gives rise to the $J = 0$ state.

While the first scenario (direct metal-metal bonding) is well supported for the case

of Li_2RuO_3, it is not a likely explanation for our Ir^{5+} compounds, as $NaIrO_3$ and $Sr_3CaIr_2O_9$ show similar magnetic properties despite having wildly different Ir-Ir connectivity and internuclear distances. Further information can be obtained by examining the Ir–O bond lengths and octahedral distortions, as they provide direct signatures of orbital degeneracy. Fig. 4.6 compares the Ir–O bond lengths present in $Sr_3CaIr_2O_9$ and $Sr_3CaRu_2O_9$ using Gaussian kernel density estimates and illustrations to provide a visual understanding of the distortions present in these octahedra. Both compounds exhibit similar "three short, three long" distortions of the two octahedral metal sites, as discussed in section 2.1. These distortions are distinctly asymmetric, and thus inconsistent with a Jahn–Teller effect. The asymmetry is also likely not due to extended crystal field effects, as both Ir sites have similar extended coordination spheres (proximity to Ca^{2+} and Sr^{2+} ions). Rather, the observed asymmetry is likely a direct consequence of SOC, which, due to the mixing of bare-ion orbital identities, gives rise to asymmetric (i.e. direction-dependent) exchange. The fact that the octahedral distortions are amplified in $Sr_3CaIr_2O_9$ compared to $Sr_3CaRu_2O_9$ provides further support for the influence of SOC. Future spectroscopic experiments can directly probe for the excited states predicted by this model, and the optical signatures should also respond to application of a magnetic field, thus yielding a powerful method of investigating SOC–driven physics in these compounds.

4.5 Conclusions

Two new insulating honeycomb iridates, $NaIrO_3$ and $Sr_3CaIr_2O_9$, have been synthesized and characterized *via* diffraction experiments, magnetometry, and resistivity. In both compounds, iridium exists in a 5+ oxidation state, yielding a $5d^4$ electronic configuration. Magnetization measurements demonstrate that both compounds exhibit negligible magnetic susceptibility, implying that both of these compounds are in close proximity to either a $S = 0$ or a $J = 0$ magnetic state. Structural studies performed on $Sr_3CaIr_2O_9$ suggest SOC is the dominant energy scale in determining the ground magnetic state of Ir^{5+} compounds.

Further spectroscopic experiments on these compounds will shed light on the nature of the magnetism observed in iridates.

4.6 Acknowledgements

DCW and TMM gratefully acknowledge support from the David and Lucile Packard Foundation and the American Chemical Society Petroleum Research Fund. The Institute for Quantum Matter is supported by the U.S. Department of Energy, Office of Basic Energy Sciences, Division of Material Sciences and Engineering under Grant No. DE-FG02-08ER46544. R. DCW and TMM are grateful to the NIST Center for Neutron Research for the neutron diffraction beam time obtained on BT-1.

4.7 Instrumental Details

All laboratory X-ray powder diffraction (XRPD) data were collected on a Bruker D8 Focus diffractometer with a LynxEye CCD detector. Neutron Powder Diffraction (NPD) data were collected on the BT-1 powder diffractometer at the NIST Center for Neutron Research. Ge (311) (λ = 2.077 nm) monochromation along with 15' and 60' source and sample collimation were employed, and the sample was housed in a 4mm cylindrical vanadium can. A high-temperature vacuum furnace was used for both 300K and 1100K diffraction experiments. Synchrotron XRPD data were collected at Argonne National Laboratory *via* the Advanced Photon Source 11-BM rapid access mail-in program. DC magnetization measurements were collected on powder samples, and four-probe resistance measurements were performed on rectangular bars cut from sintered polycrystalline pellets. All physical properties measurements were performed on a Quantum Design Physical Property Measurement system.

5 Binding–Limited Deintercalation Kinetics at the Solid–Liquid Interface

Under Review, *Nature Communications*

David C. Wallace[1,2], Benjamin A. Trump[1,2], Tyler A. Chavez[1] and Tyrel M. McQueen[1,2,3,*]

[1]Department of Chemistry,

The Johns Hopkins University, Baltimore, MD 21218, USA

[2]Institute for Quantum Matter, Department of Physics and Astronomy,

The Johns Hopkins University, Baltimore, MD 21218, USA

[3]Department of Materials Science and Engineering,

The Johns Hopkins University, Baltimore, MD 21218, USA

[*]Corresponding Author

5.1 Abstract

We investigate the kinetics of Na^+ ion deintercalation *via* the *chimie douce* reaction between Br_2 or I_2 and a phase-separating solid state cathode material Na_2IrO_3. In contrast to expectations for a diffusion-limited process, the observed heterogeneous reaction rates decrease on warming at temperatures above 0°C, corresponding to an apparent negative activation barrier for ion deintercalation. At lower temperatures, a positive activation barrier is observed. These observations directly imply that solid state diffusion is not the rate limiting step at temperatures above 0°C. We present a phenomenological model in which the sign change in activation energy occurs due to the negative temperature dependence of the oxidant binding affinity. Our results demonstrate that it is possible to perform bulk solid state chemical transformations in which diffusion is not the rate limiting step, opening the door to improved battery performance and selective bond making and breaking in the solid state.

5.2 Introduction

The principle of deintercalation, i.e. the electrochemically-driven removal of ions from a solid, forms a foundation for many of today's technologies; from the lithium ion batteries that power electronics, to the oxygen sensors that ensure safe and efficient operation of combustion engines, deintercalation chemistry is everywhere [72–74]. Cation deintercalation reactions have the basic form:

$$A^+M^{(n-1)+}B^{n-}_{(s)} \longrightarrow M^{n+}B^{n-}_{(s)} + A^+ \tag{30}$$

where AMB is a solid comprised of a cation A, a metal M in a high oxidation state, and a small, electronegative species B. Removal of a cation A to produce an oxidized solid MB is an endothermic process, meaning that an electrochemical driving force must be applied to the system in order for deintercalation to occur. This is often accomplished by

constructing a galvanic cell, where the oxidation half reaction is balanced by a separate reduction half reaction, and a bias voltage between the two half reactions is applied; this is the basic principle behind many of today's batteries. Another method of accomplishing deintercalation utilizes a solution-phase species with a strong oxidizing potential to provide the electrochemical driving force for deintercalation. When an oxidant X is employed in this manner, the deintercalation reaction becomes:

$$A^{+}M^{(n-1)+}B^{n-}_{(s)} + X_{(sol)} \longrightarrow M^{n+}B^{n-}_{(s)} + A^{+}X^{-}_{(sol)}, \tag{31}$$

where (s) indicates solid-phase, and (sol) indicates solution-phase. Reactions of this type, often referred to as soft chemistry or "*chimie douce*," are said to yield kinetic–not thermodynamic–products because small thermal energy scales favor reaction routes with low activation barriers, rather than those that yield the most thermodynamically stable products [75]. For this reason *chimie douce* techniques offer convenient routes to producing metastable compounds with interesting structural, magnetic and electronic properties. For example, the ability to control cation stoichiometry using deintercalation chemistry has led to advancements in the study of superconductivity [76], battery cathode materials [77], and solid-state reactivity [78]. Such reactions are convenient because they eliminate the need for complicated galvanic cells and offer precise control over product stoichiometry. Despite their utility, little is known about the mechanistic details of these reactions, and research in the field is dominated by studies focused on the macroscopic properties of complete galvanic cells, rather than the microscopic details of oxidative deintercalation. In particular, it is often assumed that the rate at which deintercalation can occur in these reactions is governed by ionic transport (diffusion) in the solid state [79–82]. Solid state diffusion is particularly complex in phase separating materials such as $LiFePO_4$, where cation-rich and cation-poor regions are structurally distinct and spatially separate [83]. Such materials have attracted significant interest recently due to their potential to exhibit high cycling

(charge/discharge) rates. In phase separating materials, the cycling rate is thought to be heavily influenced by the phase transformation boundary in the solid, and numerous studies have been targeted at understanding the mechanism of charge transport in these materials both in the solid state and at the solid–liquid interface [84–87]. The electrolyte is known to play an important role in cell performance due to the potential for decomposition and/or formation of a solid–electrolyte interphase, but these effects are extrinsic to the cathode [88–90]. Very recently, interfacial charge transfer kinetics have been found to play a major role in certain porous electrodes [91], but in general reactions at interfaces are thought to proceed much more rapidly than diffusion in the solid. Here, by investigating the oxidative deintercalation of sodium ions from Na_2IrO_3, we provide evidence that reactions at the solid-electrolyte interface, namely the binding of solution phase oxidant to the solid surface, can limit the rate at which deintercalation occurs in *chimie douce* reactions.

We recently reported the synthesis of $NaIrO_3$ *via* oxidative deintercalation of sodium from Na_2IrO_3 [92]. Iridium is oxidized in this process by the formation of a sodium vacancy, as shown below using Kroger-Vink notation:

$$\mathrm{Na}_{\mathrm{Na}}^{\mathrm{x}} + \mathrm{Ir}_{\mathrm{Ir}}^{\mathrm{x}} + \mathrm{X} \longrightarrow \mathrm{V}_{\prime\mathrm{Na}} + \mathrm{Ir}_{\mathrm{Ir}}^{\bullet}. \tag{32}$$

The sodium vacancy is accommodated by a structural phase transition from Na_2IrO_3 to $NaIrO_3$, and no variability in sodium content is observed in either end member, meaning that Na_2IrO_3 is a rare example of a perfectly phase-separating cathode material. The reaction between Na_2IrO_3 and an oxidant, X, produces $NaIrO_3$ as follows:

$$\mathrm{Na_2IrO_{3(s)}} + f\ X_{(sol)} \longrightarrow f\ NaIrO_3 + (1-f)\ Na_2IrO_{3(s)} + f\ NaX_{(sol)}. \tag{33}$$

Complete sodium deintercalation can be achieved using either iodine or bromine in a variety of polar, aprotic solvents, with a temperature range limited only by the melting and boiling points of the chosen solvent. Na_2IrO_3 is a convenient material in which to study

the mechanism of oxidative deintercalation for several reasons: first, it is completely phase-separating (no intermediate $Na_{2-x}IrO_3$ phases exist). Second, both Na_2IrO_3 and $NaIrO_3$ are reasonably stable under ambient conditions. Third, the reaction can be completed using either iodine or bromine as an oxidant. Finally, the reaction takes place on a timescale that is convenient for kinetics experiments on the benchtop. Furthermore, the strong optical absorption bands of I_2 and Br_2 offer a convenient method by which the progress of the oxidative deintercalation reaction can be monitored quantitatively *in-situ*. We therefore studied the kinetics of oxidative sodium deintercalation from Na_2IrO_3 by monitoring the oxidant concentration in solution as a function of time.

5.3 Materials and Methods

5.3.1 Reagents and Instrumentation

Stock oxidant solutions were prepared using iodine (Sigma Aldrich, 99.8%) or bromine (Sigma Aldrich, 99.99%) in either acetonitrile (Fisher Scientific, HPLC grade), dichloromethane (Sigma Aldrich, HPLC grade), or chloroform (Millipore, 99.8%). Temperature-dependent Ultraviolet-Visible Absorbance Spectroscopy (UV-Vis) spectra were recorded with either a Cary Bio-50 spectrophotometer equipped with a liquid nitrogen cooled Unisoku USP-203-A cryostat (T $<$ 10 C) or a HP Model 8453A spectrophotometer equipped with a Neslab Endocal RTE-8DD refrigerated circulating bath (T $>$ 10 C). Laboratory X-ray powder diffraction (XRPD) data were collected on a Bruker D8 Focus diffractometer.

5.3.2 Experimental Procedure and Considerations

The reaction between Na_2IrO_3 and an oxidant, X, produces $NaIrO_3$ as follows:

$$Na_2IrO_{3(s)} + f\ X_{(sol)} \longrightarrow f\ NaIrO_3\ +\ (1-f)\ Na_2IrO_{3(s)}\ + f\ NaX_{(sol)}. \tag{34}$$

We initially endeavored to explore the kinetics of this reaction by monitoring the oxidant concentration in solution with single-wavelength UV-Vis absorption spectroscopy. The raw *absorbance vs. time* data were used to compute the *reaction progress*, f, as a function of time using the following equation:

$$f\ =\ \frac{2([X_2]_0\ -\ [X_2]_t) \times Volume)}{mol\ Na_2IrO_3} \tag{35}$$

where $[X_2]_0$ is the initial oxidant concentration, $[X_2]_t$ is the oxidant concentration at time t, and mol Na_2IrO_3 is the number of moles of Na_2IrO_3. Note that this equation assumes a 1:1 correspondence between X_2 consumption and product fraction. Fig. 5.1 shows reaction progress plots for three different sets of reaction conditions: X_2= Br_2 in acetonitrile,

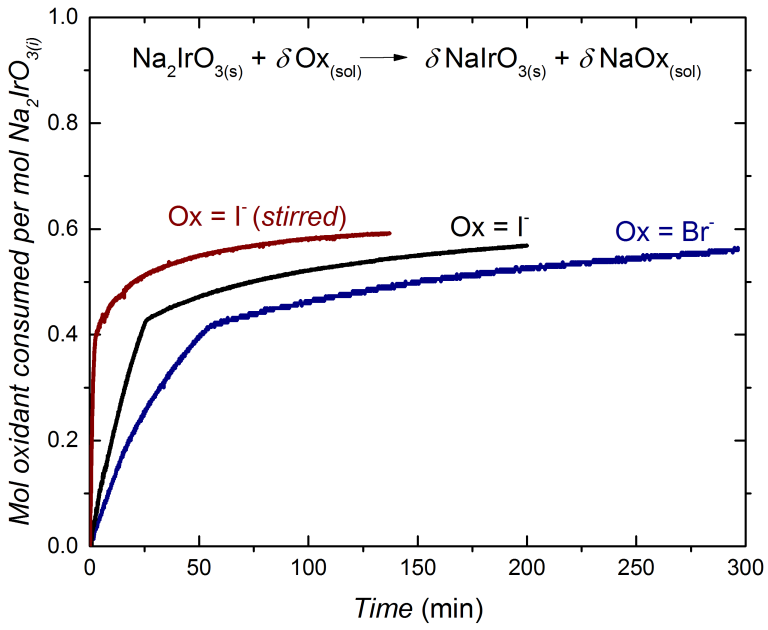

Figure 5.1: Reaction progress plots for three different sets of reaction conditions: X_2= Br_2 in acetonitrile (blue), X_2= I_2 in acetonitrile (black), and X_2= I_2 in acetonitrile with magnetic stirring (red). In all three cases a sharp "kink" is observed in the data, suggestive of an abrupt change in reaction kinetics.

X_2= I_2 in acetonitrile, and X_2= I_2 in acetonitrile with magnetic stirring. In all three cases a sharp "kink" was observed in the data, suggestive of an abrupt change in reaction kinetics. Further reactions were performed that confirmed the reproducibility of the kink. While the time at which the kink occurred varied between reactions due to stirring and temperature differences, the *progress f* at which it occurred was found only to be affected by the ratio between initial oxidant concentration and Na_2IrO_3 mass, and was highly reproducible for identical oxidant:Na_2IrO_3 mass ratios. Higher oxidant:Na_2IrO_3 caused the kink to occur at higher values of f.

Focusing on reactions between Br_2 and Na_2IrO_3 in varying ratios in acetonitrile, samples were quenched at various at various time points by collecting the partially reacted powder *via* vacuum filtration and rinsing with fresh solvent. Each powder sample was then

analyzed using XRPD and Rietveld refinement to the XRPD data using was performed to determine the phase fractions of reactant, Na_2IrO_3 (1-f), and product, $NaIrO_3$(f), present in each sample. Fig. 5.2 shows the phase fraction determined from XRPD data for various X_2:Na_2IrO_3 ratios, where each reaction was either quenched at its kink or allowed to reach completion. For each reaction a substantial difference in phase fraction ($NaIrO_3$/Na_2IrO_3) was observed between the quenched and completed samples, despite apparently similar stoichiometries.

Collection of multi-wavelength UV-Vis absorption data during the course of the reactions showed the emergence of an additional solution-phase species with a strong optical absorption band below 500nm. Titration experiments using solutions of halogens (I_2 or Br_2) and sodium halide salts (NaI or NaBr) in acetonitrile showed that the additional absorption bands arise due to the formation of sodium trihalide (NaI_3 or $NaBr_3$) in solution. The equilibrium between the solution-phase species is described by:

$$NaX + X_2 \rightleftharpoons NaX_3. \tag{36}$$

K_{eq} for these equilibria are relatively large in acetonitrile, with values of $8.2(6)\times10^4$ for Br_2 and $1(1)\times10^5$ for I_2. The trihalide equilibrium constant depends significantly the oxidant and solvent combination. No trihalides were observed to form in dichloromethane. Nevertheless, the presence of these solution-phase equilibria fully explains the kinks observed in our acetonitrile data: at times before the kink occurs, the limiting reagent in the solution-phase trihalide equilibrium is the sodium halide salt (NaX), and therefore the solution-phase equilibrium consumes X_2. The kink occurs when sufficient NaX has been produced by the deintercalation reaction.

To account for the trihalide equilibrium, new kinetics datasets were collected by scanning a broad spectrum of wavelengths at each time point and recording the resulting absorption data. These new datasets were used to compute the halogen and trihalide con-

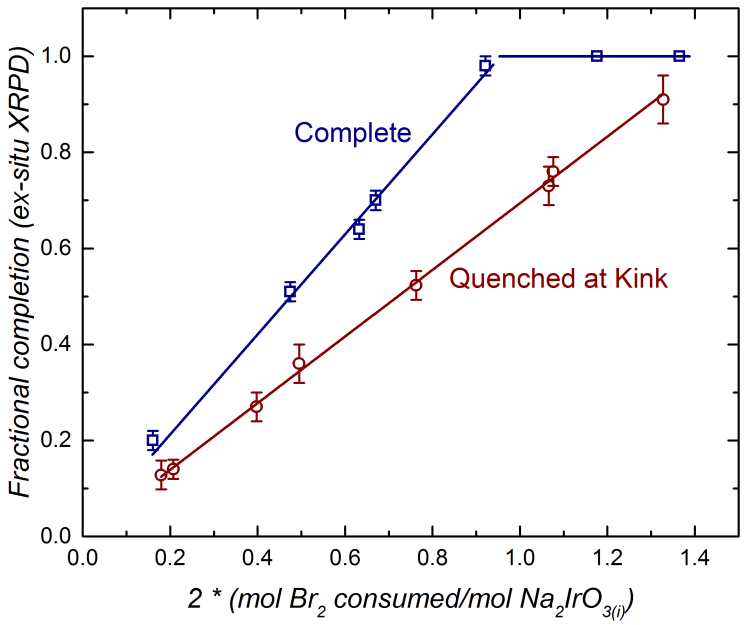

Figure 5.2: Plots of product phase fraction observed from Rietveld refinement to XRPD data plotted against reaction progress computed from single-wavelength UV-Vis data. Error bars represent the statistical uncertainty in the XRPD phase fraction.

centrations at each time point. We obtained a 1:1 correspondence between solution-phase concentrations ($[X_2]_t$, $[NaX_3]_t$) and observed reaction progress (f) as follows:

$$f = \frac{2((([X_2]_0 - [X_2]_t) - 3[NaX_3] \times Volume)}{mol\ Na_2IrO_3}. \quad (37)$$

The stoichiometric relationship in equation (5), was confirmed by comparison to XRPD data on quenched reactions. For all reactions studied, the progress computed from UV-Vis data was found to be in good agreement the product phase fraction observed in the XRPD data, as shown in Fig. 5.3. Furthermore, Transmission Electron Microscopy data (not shown) showed no evidence of additional amorphous solid phases. From all of these data, it is clear that the progress of the deintercalation reaction in the solid state can be measured by tracking the concentrations of solution-phase reactants and side-products. Therefore, in the interest of simplicity, when comparing the rates of reactions with identical Na_2IrO_3 masses, we present our results in the form of $d[X]/dt$ rather than df/dt.

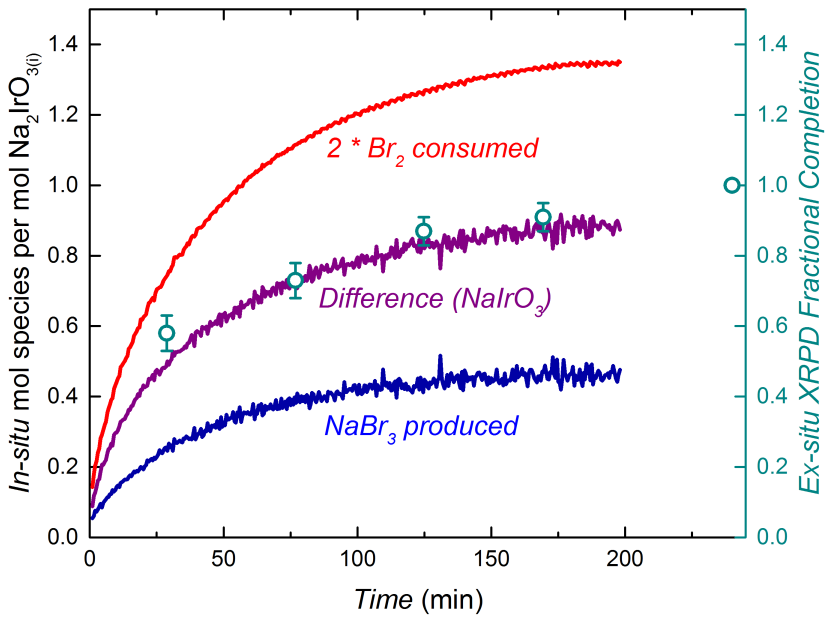

Figure 5.3: Molar quantities of Br consumed (red), $NaBr_3$ produced (blue), and $NaIrO_3$ produced (purple), all normalized by the number of moles of Na_2IrO_3 used in the reaction, are plotted versus time. Green circles with error bars show the phase fraction of $NaIrO_3$ at several time points, calculated from Rietveld refinement to laboratory XRPD data. The reaction progress f calculated from the XRPD data are in good agreement with the progress calculated from *in-situ* UV-Vis measurements.

5.4 Results and Discussion

Fig. 5.4 shows kinetics data collected on reactions between Na_2IrO_3 and bromine in dichloromethane (CH_2Cl_2). The natural logarithm of the total atomic bromine concentration is plotted as a function of time for three reactions of identical stoichiometry performed at $T = 10°$, 17.5° and 25° C, respectively. Over this temperature range the reaction rate was observed to *decrease* on warming, in stark contrast to what is expected from an energetics standpoint. Linear fits to the data over the time interval t = 5-24 min were used to construct an Arrhenius plot of the natural log of the apparent first-order rate constants versus inverse temperature (Fig. 5.4 (inset)), which showed an upward slope, implying a *negative* activation energy. Furthermore, the reaction rate was observed to increase drastically as a result of gentle stirring in this temperature regime (Supplementary). In order to explore this unexpected result in more detail, additional deintercalation reactions were carried out for a variety of oxidant/solvent combinations over a broad range of temperatures. Fig. 5.5(a) shows plots of oxidant concentration versus time for reactions between Na_2IrO_3 and either iodine or bromine in either chloroform ($CHCl_3$), dichloromethane (CH_2Cl_2), or acetonitrile (CH_3CN). In all cases, the initial Na_2IrO_3 mass and oxidant solution volumes were constrained to be the same. The oxidant concentrations were not constrained to be the same between different solvents, as the different optical absorptivities of each oxidant solution require that the concentration be adjusted to a reasonable level for accurate quantification. In all of these plots, the "shape" of each kinetic trace is related to the temperature at which the reaction was performed: reactions taking place at low temperatures appear linear, while reactions performed at high temperature have significant curvature. Because the shape of the kinetic trace is not consistent across all datasets, it was not possible to directly compare rate constants by linear fitting to zeroeth, first, or second-order plots, as is customary in kinetics research. Instead the numerical derivatives $d[X]/dt$ were calculated by performing linear fits to 12 minute subsets of each dataset at each time point.

Fig. 5.5(b) shows plots of $d[X]/dt$ versus time for all datasets presented in this work.

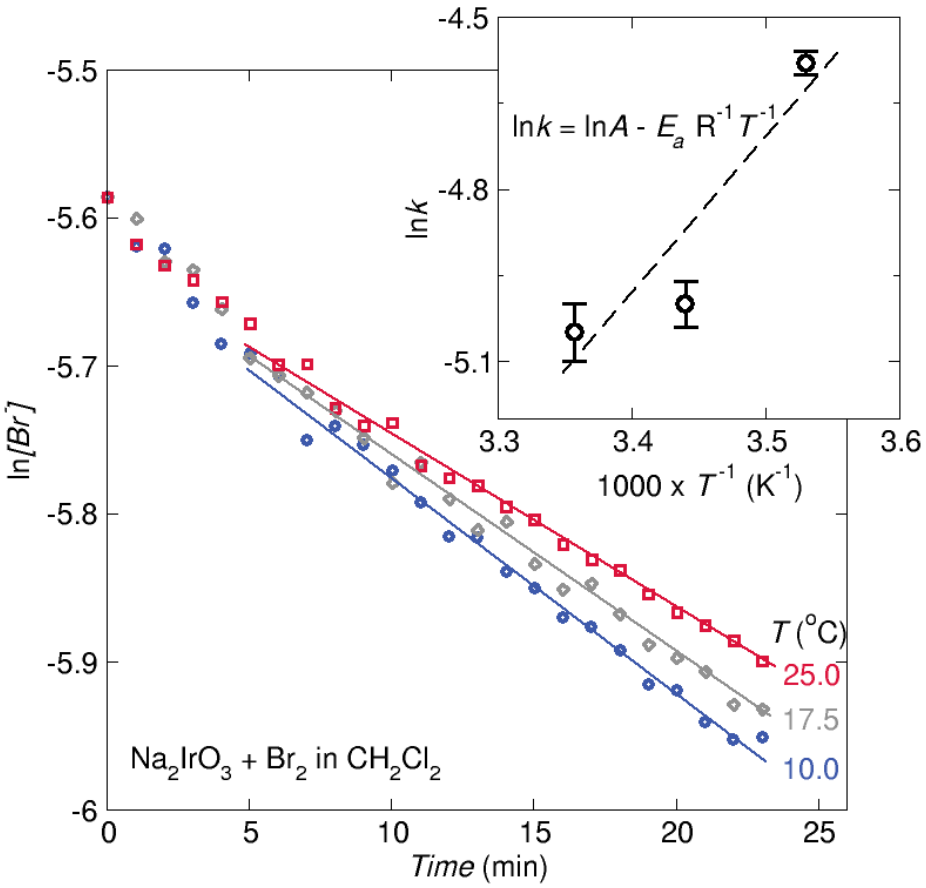

Figure 5.4: Deintercalation rates exhibit a negative temperature dependence at high temperatures. The natural log of the concentration of bromine in dichloromethane is plotted as a function of time for three stoichiometrically identical reaction performed at $T = 25.0°C$ (red squares), 17.5°C (gray diamonds), and 10.0°C (blue circles). Linear fits to the data over the time interval $5 < t < 24$ min, shown as solid lines, were used to extract first-order rate constants k for each of the reactions. Inset: There is a clear increase in the reaction rate on cooling, which is reflected in the upward slope of the plot of $\ln(k)$ vs. T^{-1}

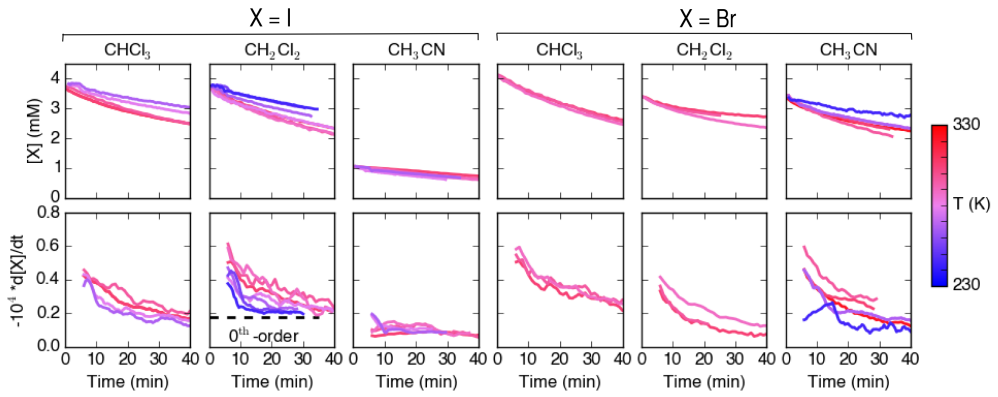

Figure 5.5: Oxidative deintercalation kinetics data show an unexpected temperature dependence. a-f) Reactions between Na_2IrO_3 and iodine (first 3 columns) or bromine (second 3 columns) are plotted on the top row. Each column represents a different solvent ($CHCl_3$, CH_2Cl_2, CH_3CN), and the solvents are arranged from left to right in order of increasing polarity. Bromine has a greater oxidizing potential than iodine by a factor of roughly 2. Temperature is represented by the color of each kinetic trace, with dark red being the warmest (323 K), and dark blue being the coldest (243 K). The apparent order of the reaction, which is reflected in the curvature of each kinetic trace, is strongly temperature and concentration dependent. **g-l)** The first derivative of oxidant concentration is plotted as a function of time and these plots are organized in the same manner as plots a-f. At high temperatures, reaction rates decrease gradually with respect to time until the reaction is complete. At low temperatures, the reaction rate decreases initially until reaching a roughly constant value, signaling a crossover into the diffusion-limited regime as described in the text.

At high temperatures the reaction rate decreases in magnitude continuously, while at the lowest temperatures the reaction rate initially decreases before reaching a constant value. The trend in the magnitudes of the reaction rates can also be roughly seen in these plots: the largest observed reaction rates are not achieved at the lowest or highest studied temperatures, but rather at some intermediate temperature between the two extremes. In order to illustrate this trend, the average reaction rate over the time interval of 15 to 20 minutes was computed for each reaction. Fig. 5.6(a) shows the natural logarithm of these average reaction rates, normalized by initial oxidant concentration, plotted as a function of inverse temperature (Arrhenius plot). The trend at high temperatures (low T^{-1}) is clear: reaction rates decrease on warming. At lower temperatures (Fig. 5.6(b)), the reaction rates recover the expected exponential temperature dependence, which manifests as a straight line with downward slope in the Arrhenius plot.

The decrease in reaction rates on warming in the high-temperature regime is interesting and unexpected from an energetics standpoint. An intuitive explanation for this behavior is obtained by examining how the rate of each individual step in the mechanism should respond to changes in temperature. At a minimum, the mechanism of charge and mass transport at the solid-electrolyte interface in a generic *chimie douce* reaction must contain five discrete steps, written in Kroger-Vink notation:

(1)	$\mathrm{X_{sol}} \longrightarrow \mathrm{X_{ads.}}$	*Oxidant Diffusion/Adsorption*
(2)	$\mathrm{M_M^x} + \mathrm{X_{ads}} \longrightarrow \mathrm{M_M^\bullet} + \mathrm{X_{ads}^-}$	*Oxidant-Metal RedOX*
(3)	$\mathrm{A_A^x} + \mathrm{X_{ads}^-} \longrightarrow \mathrm{V_{A(surf)}} + \mathrm{AX_{ads}}$	*Salt Formation*
(4)	$\mathrm{AX_{ads}} \longrightarrow \mathrm{AX_{sol}}$	*Salt Desorption/Diffusion*
(5)	$\mathrm{A_{A(bulk)}} + \mathrm{V_{A(surf)}} \longrightarrow \mathrm{V_{A(bulk)}} + \mathrm{A_{A(surf)}}$	*Solid State Cation Diffusion*

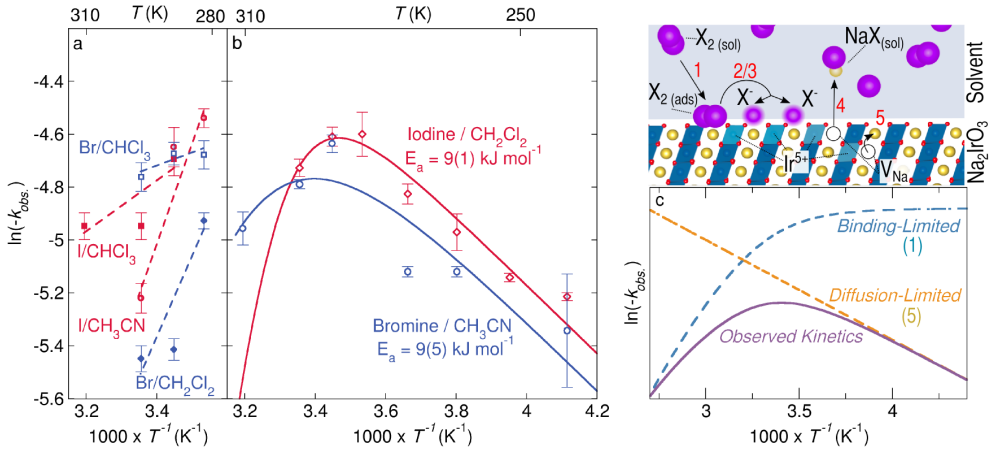

Figure 5.6: Crossover between binding-limited and diffusion-limited temperature regimes. **a)** An Arrhenius plot of ln(-$k_{obs.}$) vs. T^{-1} in the high-temperature regime. Error bars represent the standard deviations of the reaction rates in the 5 minute averaging window. There is a clear upward slope in each dataset, implying a negative activation energy. **b)** Data for two selected oxidant/solvent combinations are shown on an Arrhenius plot over a broad temperature range. At high temperatures (low T^{-1}) the reaction rate exhibits a negative temperature dependence, characterized by an upward slope in this plot, while at low temperatures (high T^{-1}) the reaction rate exhibits a standard, positive exponential temperature dependence, as expected for a diffusion-limited process. Solid lines represent fits of our phenomenological model to both experimental datasets. **c)** A graphical representation of the oxidative deintercalation mechanism shows each of the 5 elemental steps detailed in the text. The model presented in the text combines a sigmoidal term to represent oxidant binding affinity (blue dashes, step 1) and an exponential term to represent diffusion (orange dashes, step 5), and the product of these two terms produces a good qualitative description of the observed kinetic behavior (purple line).

A graphical representation of these steps is shown in Fig. 5.6(c). In the first step (1), an oxidant species in solution diffuses to the cathode and becomes adsorbed to the solid surface, at which point oxidant-metal RedOx (2) and salt formation (3) can occur either in series or in unison. Finally, formation of a cation vacancy on the surface by desorption and diffusion of the charge-balanced salt into the solvent (4) is followed by ionic diffusion in the solid state (5). Basic energetics dictates that steps 2-5 must increase in rate as temperature is increased. The reduction in rates at high temperatures also cannot be explained by the formation of an oxidant concentration gradient at the interface, as this, too, must become less favorable at higher temperatures due to increased diffusion in the liquid phase. The rate of the adsorption step, however, is expected to have a negative temperature dependence due to the loss in entropy associated with confinement of a solution phase particle to a surface. Thus the oxidant adsorption step is most likely rate-limiting in the high temperature regime. To explore this possibility, we construct a minimal phenomenological model consisting of a exponential term (Arrhenius-like activation barrier) to model solid state diffusion, and an additional sigmoidal term to model the surface binding affinity of the oxidant as a function of temperature:

$$Rate \sim\ k(T)_{diffusion} \times\ \rho(T)_{bind} = Ae^{\frac{-E_a}{RT}} \times\ \frac{1}{1+e^{-\alpha(T-\beta)}} \tag{38}$$

where E_a is the activation energy for diffusion of Na^+ in $Na_2IrO_3$and α and β characterize the binding affinity of the oxidant in a given solvent by controlling the width and center of the binding affinity curve as a function of temperature. Fits of this model to the data collected on reactions between Na_2IrO_3 and iodine in $CHCl_3$ and bromine in CH_3CN (Fig. 5.6(b)) yield activation energies E_a = 9(1) and 9(5) kJ/mol, respectively. While these values may seem small, they are close to the values found for cation migration in KNi_2Se_2 and KIr_4O_8 [57, 78], and roughly one third of that found for $NaCoO_2$ [95].

Our assertion that the reaction rate can be influenced by factors extrinsic to the cathode

material in the high-temperature regime is consistent with several key observations. First, for identical solvents and oxidant concentrations, deintercalations using iodine as an oxidant proceed more rapidly than those using bromine, despite the fact that bromine has an oxidation potential nearly twice that of iodine. Furthermore, the significant variability of the reaction rate as a function of solvent provides evidence that the reaction rate is strongly influenced by the choice of electrolyte solution, as the oxidant's affinity for the solvent has significant negative effect on its binding affinity. At low temperatures our model predicts a return to a standard Arrhenius-like activation barrier, which implies that a process intrinsic to the cathode material, such as solid state diffusion, is the rate limiting step in the mechanism. This is consistent with the observation that, at low temperatures, the reaction rate reaches a roughly constant value regardless of oxidant concentration, which can be plainly seen both in the raw concentration vs. time data (Fig. 5.5 (a)) and in the d$[X]$/dt vs time data (Fig. 5.5 (b)).

The fact that the rate of a *chimie douce* oxidative deintercalation reaction is not purely exponentially linked to temperature and electrochemical potential is highly important, and can be used to drive further progress in materials research. For example, a common problem in *chimie douce* chemistry is that rapid ion deintercalation produces large concentration gradients in the solid state that generate large inter-particle strain and reduce particle size. Our results suggest that *increasing* the temperature of such reaction could alleviate this problem by reducing the deintercalation rate and increasing the rate of diffusion in the solid, thereby decreasing strain and improving crystallinity. The ability to achieve slow deintercalation using using a strong oxidant at high temperature could therefore lead to the discovery of new, potentially novel materials.

Our results also have profound implications for the field of battery research. The understanding that the binding interaction between solution-phase charge transport agent and solid electrode is a key component of cell performance may be important to building a unified theory of electrode-electrolyte kinetics, and could be used to rationally select charge

transport agents for specific purposes. For example, in many materials cation migration occurs along multiple crystallographically distinct directions that can have different energetics [93, 94]; by choosing an appropriate charge transport agent that preferentially binds to a particular surface facet or morphology, one could effectively restrict the ion migration pathway in the solid. Further experimental and theoretical work is thus necessary to understand the implications and limitations of the binding-limited reaction rate phenomenon.

5.5 Methods

Polycrystalline Na_2IrO_3 was prepared *via* reported methods and kept in an argon-filled glovebox [51]. Reactions described by equation (4) were performed inside an Ultraviolet-Visible Absorption Spectrophotometer (UV-Vis) as follows: to a quartz cuvette was added 3.00mL of a standard oxidant solution consisting of I_2 or Br_2 in either acetonitrile (CH_3CN), dichloromethane(CH_2Cl_2), or chloroform($CHCl_3$). A UV-Vis absorption spectrum of the oxidant solution was collected to calibrate the instrument, then the deintercalation reaction was initiated by quickly transferring a known mass of Na_2IrO_3 from an inert atmosphere to the cuvette, which was then sealed with a glass stopper. Absorption spectra were collected at evenly-spaced time points throughout the course of the reaction, and each absorption spectrum was used to compute the oxidant concentrations at each time point. Particle settling was observed to interfere with the absorption measurement in the first few minutes of each dataset, but was negligible beyond 5 minutes. Solution phase equilibria–namely those between halogens (I_2 or Br_2), halide salts (NaI and NaBr) and trihalides (NaI_3 or $NaBr_3$)–were observed in several solvents, and were accounted for in our calculations. These concentrations, along with the known mass of Na_2IrO_3, were used to compute the total halogen concentration at time t, $[X]_t$, and the fractional completion of the reaction:

$$f = \frac{2(([X_2]_0 - [X_2]_t) - 3[NaX_3]) \times Volume}{mol\ Na_2IrO_3} = \frac{([X]_0 - [X]_t) \times Volume}{mol\ Na_2IrO_3}. \quad (39)$$

The 1:1 relationship between oxidant consumption and $NaIrO_3$ production implied by equation (5) was confirmed by reference to *ex-situ* Xray powder diffraction data (see SI.) In the interest of simplicity, when comparing the rates of reactions with identical Na_2IrO_3 masses, we present our results in the form of $d[X]/dt$ rather than df/dt. A more detailed discussion of the experimental procedure and considerations can be found in Supplementary Information.

5.5.1 Acknowledgements

The authors would like to thank Patrick Rogler and Jung-Yoon Lee for technical assistance. Funding for this work was provided by the American Chemical Society Division of Inorganic Chemistry Exxon-Mobil Solid State Faculty Fellowship and the National Science Foundation (NSF) Division of Materials Research (DMR) CAREER grant #1253562.

References

[1] J. G. Bednorz, K. A. Müller, Possible High-T_C Superconductivity in the Ba-La-Cu-O System. *Zeitschift für Physik B* **64**, 189-193 (1986)

[2] J. E. White, An Introduction To Group Theory For Chemists. it J. Chem. Ed. **44**, 128-135 (1967)

[3] D. M Bishop, Group Theory and Chemistry. Oxford: The Clarendon Press (1973) *print*

[4] M. S. Dresselhaus, G. Dresselgaus, A. Jorio, *Group Theory: Application to the Physics of Condensed Matter.*, Springer–Verlag Berlin Heidelberg, Leipzig, 2008

[5] D. A. McQuarrie, J. D. Simon, Physical Chemistry: A Molecular Approach. Sausalito, CA: University Science Books (1997) *print*

[6] R. H. Crabtree, The Organometallic Chemistry of the Transition Metals, 6th Edition. Hoboken, NJ: John Wiley and Sons, Inc. (2009) *print*

[7] N. W. Ashcroft, N. D. Mermin, Solid State Physics. Belmont, CA: Brooks/Cole, Cengage Learning (1976) *print*

[8] H. A. Jahn and E. Teller, Stability of Polyatomic Molecules in degenerate States. I. Orbital Degeneray.. *Roal Society Proceedings A* **161**, 220 (1937)

[9] B. Bleaney, K. D. Bowers, and R. S. Trenam, Paramagnetic Resonance in Diluted Copper Salts II: Salts with Trigonal Symmetry. *Royal Society Proceedings A.* **225**, 157-166 (1955)

[10] N. F. mott and R. Peierls, Discussion of the Paper by Boer and Verway, *Proceedings of the Physical Society* **49** 72-73, (1937)

[11] N. F. Mott, The Basis of the Electron Theory of Metals, with Special Reference to the Transition Metals, *Proceedings of the Physical Society. Section A* **62**, 416 (1949)

[12] A. S. Moskvin, True charge-transfer gap in parent insulating cuprates, *Physical Review B* **84**, 075116 (2011)

[13] W. H. Bragg, W. L. Bragg *Proc. R. Soc. Lond. A* **88**, 428-438 (1913)

[14] B. E. Warren. X-ray Diffraction. New York: Dover Publishing, (1990) *print*

[15] H. M. Rietveld. A profile refinement method for nuclear and magnetic structures. *Journal of Applied Crystallography* **2 (2)**, 65-71 (1969)

[16] A. C. Larson, R. B. Von Dreele, *Los Alamos National Laboratory Report LAUR*, 86–748. (2000)

[17] J. Rodriguez-Carvajal and T. Roisnel, FullProf.98 and WinPLOTR: New Windows 95/NT Applications for Diffraction Commission For Powder Diffraction, *International Union for Crystallography, Newletter* **20** (1998)

[18] M. M. J. Treacy, J. M. Newsam & M. W. Deem, A general recursion method for calculating diffracted intensities from crystals containing planar faults. *Proceedings of the Royal Society, London* **A433**, 499-520 (1991)

[19] J. B. Goodenough, Theory of the Role of Covalence in the Perovskite-Type Manganites [La,M(II)]MnO_3. *Physical Review* **100(2)**, 564-573 (1955)

[20] J. Kanamori, Theory of magnetic properties of ferrous and cobaltous oxides. I. *Progress of Theoretical Physics* **17**, 177-196 (1957)

[21] J. B. Goodenough, Suggestion Concerning the Role of Wave?Function Symmetry in Transition Metals and Their Alloys. *Journal of Applied Physics* **29**, 513 (1958)

[22] L. Antonov, S. Stoyanov, Analysis of the Overlapping Bands in UV-Vis Absorption Spectroscopy. *Applied Spectroscopy* **47**, 1030-1035 (1993)

[23] L. Antonov, D. Nedeltcheva, Resolution of overlapping UV-Vis absorption bands and quantitative analysis. *The Royal Society of Chemistry* **29**, 217-227 (2000)

[24] G. Jackeli & G. Khaliullin, Mott Insulators in the Strong Spin-Orbit Coupling Limit: From Heisenberg to a Quantum Compass and Kitaev Models. *Physical Review Letters* **102,** 017205 (2009)

[25] A. Shitade, H. Katsura, J. Kunes, X.-L. Qi, S.-C. Zhang, N. Nagaosa, Quantum Spin Hall Effect in a Transition Metal Oxide Na_2IrO_3. *Physical Review Letters* **102,** 256401 (2009)

[26] H. Gretarsson et al., Crystal-Field Splitting and Correlation Effect on the electronic structure of A_2IrO_3. *Physical Review Letters* **110,** 076402 (2013)

[27] J. Chaloupka, G. Jackeli & G. Khaliullin, Kitaev-Heisenberg Model on a Honeycomb Lattice: Possible Exotic Phases in Iridium Oxides A_2IrO_3. *Physical Review Letters* **105,** 027204 (2010)

[28] I. Kimchi, J. J. Analytis, A. Vishwanath, Three dimensional quantum spin liquid in a hyperhoneycomb iridate model and phase diagram in an infinite–D approximation. arXiv:1309.1171 (2013)

[29] E. C. Andrade, M. Vojta, Magnetism in spin models for depleted honeycomb–lattice iridates: Spin–glass order towards percolation. arXiv:1309.2951 (2013)

[30] J. G. Rau, E. K.-H. Lee, H.-Y. Kee, Generic spin model for the honeycomb iridates beyond the Kitaev limit. arXiv:1310.7940 (2013)

[31] H. Lei, Z. Zhong, H. Hosono, Structural, Magnetic, and Electrical Properties of $Li_2Ir_{1-x}Ru_xO_3$. arXiv:1311.7317 (2013)

[32] V. M. Katukuri, *et al.*, Kitaev interactions between $j = 1/2$ moments in honeycomb Na_2IrO_3 are large and ferromagnetic: Insights from *ab initio* quantum chemistry calculations. arXiv:1312.7437 (2013)

[33] Y.Singh & P. Gegenwart, Antiferromagnetic Mott insulating state in single crystals of the honeycomb lattice material Na_2IrO_3. *Physical Review B* **82**, 064412 (2010)

[34] S. K. Choi *et al.*, Spin Waves and Revised Crystal Structure of Honeycomb Iridate Na_2IrO_2. *Physical Review Letters* **108**, 127204 (2012)

[35] G. Cao *et al.*, Evolution of Magnetism in Single-Crystal Honeycomb Iridates. arXiv:1307.2212v1 (2013)

[36] J. Bréger *et al.*, High-resolution X-ray diffraction, DIFFaX, NMR and first principles study of disorder in the Li_2MnO_3–$Li[Ni_{1/2}Mn_{1/2}]O_2$ solid solution. *Journal of Solid State Chemistry*, **178**, 2575 (2005)

[37] B. H. Toby, EXPGUI, a graphical user interface for GSAS, *J. Appl. Crystallogr.*, **34**, 210–213. (2001)

[38] E. Climente-Pascual, *et. al*, Spin $\frac{1}{2}$ Delafossite Honeycomb Compound Cu_5SbO_6, *Journal of Inorganic Chemistry*, **51**, 557 (2012)

[39] J. D. Bakemore, *et al*, Half-Sandwich Iridium Complexes for Homogeneous Water-Oxidation Catalysis. *Journal of the American Chemical Society*, **132**, 16017 (2010)

[40] J. A. Mydosh, Spin Glasses: An Experimental Introduction, Taylor and Francis Inc. (1993) ISBN 0-7484-0038-9

[41] K. Binder, A. P. Young, Spin glasses: Experimental facts, theoretical concepts, and open questions. *Rev. Mod. Phys.*, **58**, 801 (1986)

[42] J. W. Lynn *et al.*, Structure and dynamics of superconducting Na_xCoO_2 hydrate and its unhydrated analog., *Physical Review B*, **68**, 214516 (2003)

[43] B.-J. Yang & Y. B. Kim, Topological insulators and metal-insulator transition in the pyrochlore iridates. *Phys. Rev. B.*, 2010, **82**, 085111

[44] X. Liu, Vamshi M. Katukuri, L. Hozoi, Wei-Guo Yin, M. P. M. Dean, M. H. Upton, Jungho Kim, D. Casa, A. Said, T. Gog, T. F. Qi, G. Cao, A. M. Tsvelik, Jeroen van den Brink, and J. P. Hill, Testing the Validity of the Strong Spin-Orbit-Coupling Limit for Octahedrally Coordinated Iridate Compounds in a Model System Sr_3CuIrO_6, *Phys. Rev. Lett.*, 2012, **109** 157401

[45] B. F. Phelan, J. Krizan, W. Xie, Q. Gibson, R. J. Cava, A new material for probing spin-orbit coupling in Iridates, *Phys. Rev. B.* 2015, **91**, 155117

[46] W. Witczak–Krempa, G. Chen, Y. B. Kim, & L. Balents, Correlated QuantumPhenomena in the Strong Spin-Orbit Regime, *Ann. Rev. Cond. Mat. Phys.*, 2013, **5**, 57-82

[47] D. Hirai, J. Matsuno, H. Takagi, Fabrication of (111)-oriented Ca0.5Sr0.5IrO3/SrTiO3 superlattices–A designed playground for honeycomb physics, *APL Materials*, 2015, **3**, 041508

[48] K. A. Modic, *et al.*, Realization of a three-dimensional spin-anisotropic harmonic honeycomb iridate, *Nature Communications*, 2014, **5**, 4203

[49] K. Baroudi *et al.*, Structure and Properties of α-$NaFeO_2$-type Ternary Sodium Iridates. *J. Sol. Stat. Chem.*, 2014, **210**, 195

[50] J. T. Rijssenbeek, S. Malo, V. Caignaert, K. R. Poeppelmeier, Site and Oxidation-State Specificity Yielding Dimensional Control in Perovskite Ruthenates, *Journal of the American Chemical Society*, 2002, **124**, 2090

[51] J. W. Krizan, J. H. Roudebush, G. M. Fox, & R. J. Cava, The chemical instability of Na_2IrO_3 in air, *Materials Research Bulletin*, 2014, **52**, 162-166

[52] T.Hahn, International Tables for Crystallography, Space-Group Symmetry. *Wiley* (2005).

[53] M. M. J. Treacy, J. M. Newsam & M. W. Deem, A general recursion method for calculating diffracted intensities from crystals containing planar faults. *Proceedings of the Royal Society, London*, 1991, **A433**, 499-520

[54] D. C. Wallace, C. M. Brown, T. M. McQueen, Evolution of Magnetism in the $Na_{3-\delta}(Na_{1-x}Mg_x)Ir_2O_6$ Series of Honeycomb Iridates, *J. Sol. Stat. Chem.*, 2015, **224**, 28-35

[55] M. Bremholm, S. R. Dutton, P. W. Stephens, R. J. Cava, $NaIrO_3$-A pentavalent post-perovskite, *J. Sol. Stat. Chem.*, 2011, **184**, 601-607

[56] T. Sakamoto, Y. Doi, Y. Hinatsu, Crystal Structures and magnetic properties of 6H-perovskite-type oxides $Ba_3MIr_2O_9$ (M = Mg, Ca, Sc, Ti, Zn, Sr, Zr, Cd and In), *Journal of Solid State Chemistry*, 2006, **179**, 2595-2601

[57] A. Talanov, W. A. Phelan, Z. A. Kelly, M. A. Siegler, T. M. McQueen, Control of the Iridium Oxidation State in the Hollandite Iridate Solid Solution $K_{1-x}Ir_4O_8$, *J. Inorg. Chem*, 2014, **53**, 4500-4507

[58] L. M. Schoop, J. W. Krizan, Q. D. Gibson, R. J. Cava, Structure and elementary properties of the new Ir hollandite $Rb_{0.17}IrO_2$, *J. Sol. Stat. Chem.*, 2014, **209**, 37-41

[59] S. A. J. Kimber, I. I. Mazin, J. Shen, H. O. Jeschke, S. V. Streltsov, D. N. Argyriou, R.Valenti, and D. I. Khomskii, Valence bond liquid phase in the honeycomb lattice material Li_2RuO_3, *Phys. Rev. B*, 2014, **89**, 081408

[60] N. A. Bogdanov, V. M. Katukuri, J. Romhanyi, V. Yushankhai, V. Kataev, B. Buchner, J. van den Brink, and L. Hozoi, Orbital reconstruction in nonpolar tetravalent transition-metal oxide layers, *Nat. Comm.*, 2015, **6**, 7306

[61] V. M. Katukuri, *et al.*, Electronic Structure of Low-Dimensional $4d^5$ Oxides: Interplay of Ligand Distortions, Overall Lattice Anisotropy, and Spin–Orbit Interactions, *J. Inorg. Chem*, 2014, **53**, 4833-4839

[62] A. Nag, *et al*, Spin-orbital liquid state assisted by singlet-triplet excitation in $J = 0$ ground state of $Ba_3ZnIr_2O_9$, *arXiv*, 2015, 1506.04312

[63] G. Cao. *et al*, Novel Magnetism of Ir^{5+} $5d^4$ Ions in the Double Perovskite Sr_2YIrO_6, *Phys. Rev. Lett.*, 2014, **112**, 056402

[64] C. I. Hiley, M. R. Lees, J. M. Fisher, D. Thomspsett, S. Agrestini, R. I. Smith, R. I. Walton, Ruthenium(V) Oxides from Low-Temperature Hydrothermal Synthesis, it J. Angew. Chem. Int. Ed., 2014, **53**, 4423-4427

[65] C. I. Hiley, D. O. Scanlon, A. A. Sokol, S. M. Woodley, A. M. Ganose, S. Sangiao, J. M. De Teresa, P. Manuel, D. D. Khalyavin, M. Walker, M. R. Lees, and R. I. Walton, Antiferromagnetism at T>500K in the layered hexagonal ruthenate $SrRu_2O_6$, *Physical Review B* **92** 104413 (2015)

[66] S. A. J. Kimber, *et al.*, Interlayer tuning of electronic and magnetic properties in honecomb ordered $Ag_3LiRu_2O_6$, *J. Mat. Chem.*, 2010, **20**, 8021-8025

[67] J. C. Want *et al.*, Lattice–tuned magnetism of $Ru^{4+}(4d^4)$ ions in single crystals of the layered honeycomb ruthenates Li_2RuO_3 and Na_2RuO_3, *Phys. Rev. B*, 2014, **90**, 161110(R)

[68] K. W. Plumb, J. P. Clancy, L. J. Sandilands, V. V. Shankar, Y. F. Hu, K. S. Burch, H.-Y. Kee, Y.-J. Kim, α–$RuCl_3$: A spin–orbit assisted Mott insulator on a honeycomb lattice, *Phys. Rev. B*, 2014, **90** 041112(R)

[69] Y. Luo, *et al.*, Li_2RhO_3: A spin-glassy relativistic Mott insulator, *Phys. Rev. B.*, 2013, **87**, 161121

[70] H. Kobayashi, M. Tabuchi, M.Shikano, H. Kageyama, Y. Kanno, Structure, and magnetic and electrochemical properties of layered oxides, Li_2IrO_3, *J. Mat. Chem*, 2003, **13**, 957-962

[71] M. J. O'Malley, H. Verweij, P. M. Woodward, Structure and properties of ordered Li_2IrO_3 and Li_2PtO_3, *J. Sol. Stat. Chem*, 2008, **181**, 1803-1809

[72] A. Yamada, S. C. Chung and K. Hinokuma, Optimized LiFePO4 for Lithium Battery Cathodes. *J. Electrochem. Soc.*,**148**, A224-A229 (2001)

[73] B. Dunn, H. Kamath, J.-M. Tarascon, Electrical Energy Storage for the Grid: A Battery of Choices. *Science* **334** 928-935 (2011)

[74] R. Ramamoorthy, P. K. Dutta, S. A. Akbar, Oxygen sensors: Materials, methods, designs and applications. *J. Mat. Sci.* **38**, 4271-4282 (2003)

[75] M. A. Hayward, Topochemical reactions of layered transition metal oxides. *Semicond. Sci. Technol.* **29**, 064010 (2014)

[76] K. Takada, H. Sakurai, E. Takayama-Muromachi, F. Izumi, R. A. Dilanian, T. Sasaki, Superconductivity in two-dimensional CoO2 layers. *Nature* **422**, 53 (2003)

[77] K. Mizushima, P.C. Jones, P.J. Wiseman, J.B. Goodenough, Li_xCoO_2 ($0 < x < 1$): A New Cathode Material for Batteries of High Energy Density. *Mat. Res. Bull.* **15**, 783-789 (1980)

[78] J. R. Neilson, T. M. McQueen, Bonding, Ion Mobility, and Rate-Limiting Steps in Deintercalation Reactions with $ThCr_2Si_2$-type KNi_2Se_2. *J. Am. Chem. Soc.* **134**, 7750 (2012)

[79] S. Y. Hong, Y. Kim, Y. Park, A. Choi, N.-S. Choi, K. T. Lee, Charge carriers in rechargeable batteries: Na ions vs. Li ions. *Energ. Eviron. Sci.* **6**, 2067-2081 (2013)

[80] J.-M. Tarascon and M. Armand, Issues and challenges facing rechargeable lithium batteries. *Nature* **414**, 359-357 (2001)

[81] L. P. Wang, L. Yu, X.Wang, M. Srinivasan, Z. J. Xu, Recent developments in electrode materials for sodium-ion batteries. *J. Mat. Chem. A* **3**, 9353-9378 (2015)

[82] N. Nitta, F. Wu, J. T. Lee, G. Yushin, Li-ion battery materials: present and future. *Materials Today* **18**, 252-264 (2015)

[83] A. K. Padhi, K. S. Nanjundaswamy, J. B. Goodenough, *J. Electrochem. Soc.* **144(b)**,1188-1194 (1997)

[84] D. Delmas, M. Maccario, L. Croguennec, F. Le Cras, F. Weill, Lithium deintercalation in $LiFePO_4$ nanoparticles via a domino-cascade model. *Nat. Mat.* **7**, 665 (2008)

[85] Y. Li *et al.*, Current-induced transition from particle-by-particle to concurrent intercalation in phase-separating battery electrodes. *Nature Materials* **13**, 1149-1156 (2014)

[86] K. Kirshenbaum, D. C. Bock, C.-Y. Lee, Z. Zhong, K. J. Takeuchi, A. C. Marschilok, E. S. Takeuchi, In situ visualization of $Li/Ag_2VP_2O_8$ batteries revealing rate-dependent discharge mechanism. *Science* **347** 6218.149 (2015)

[87] D. V. Safronova, I. Yu. Pinusa, I. A. Profatilovab, V. A. Tarnopoloskiib, A. M. Skundinc, A. B. Yaroslavtsev, Kinetics of Lithium Deintercalation from LiFePO4. *Inorg. Mat.* **47**, 303-307 (2011)

[88] D. Aurbach, *et al.*, Design of electrolyte solutions for Li and Li-ion batteries: a review. *Electrochem. Acta* **50**, 247-254 (2004)

[89] A. Ponrouch *et al.*, Towards high energy density sodium ion batteries through electrolyte optimization. *Energy & Environmental Science* **6**, 2361 (2013)

[90] P. Verma, P. Maire, P. Novak, A review of the features and analyses of the solid electrolyte interphase in Li-ion batteries. *Electrochem. Acta* **55**, 6332-6341 (2010)

[91] P. Bai, M. Z. Bazant, Charge transfer kinetics at the solid-solid interface in porous electrodes. *Nat. Comm.* **5**, 3585 (2014)

[92] D. C. Wallace, T. M. McQueen, New Honeycomb Iridium (V) Oxides: $NaIrO_3$ and $Sr_3CaIr_2O_9$. *Dalton Trans.* **44** 20344-20351DOI: 10.1039/C5DT03188E (2015)

[93] M. Ø. Filsø, M. J. Turner, G. V. Gibbs, S. Adams, M. A. Spackman and B. B. Iversen, Visualizing Lithium-Ion Migration Pathways in Battery Materials. *Chem. Eur. J.* **19**, 15535-15544. (2013)

[94] C. Eames, J. M. Clark, G. Rousse, J.-M. Tarascon, and M. S. Islam, Lithium Migration Pathways and van der Waals Effects in the $LiFeSO_4OH$ Battery Material. *Chemistry of Materials* **26**, 3672-3678 (2014)

[95] J. Su, Y. Pei, Z. Yangb and X. Wang, First-principles investigation on the structural, electronic properties and diffusion barriers of Mg/Al doped $NaCoO_2$ as the cathode material of rechargeable sodium batteries. *RSC Adv.* **5**, 27229-27234 (2015)

6 Appendix A: Supporting Python Code

```python
# gaussian_functions.py
import numpy as np


def gaussian1(WL,
              h1, l1, w1,
              c):
    """
    gaussian(WL, h1, l1, w1)

    computes the predicted absorbance value for given wavelength and Br2 height,
    with two additional Gaussian-like peaks to fit the NaBr3 peak contribtution.

    Parameters
    ----------
    WL: scalar
        Wavelength in nm

    h1: scalar
        Height of total Br2 spectrum

    w1: scalar
        NaBr3 peak widths in nm

    l1: scalar
        NaBr3 peak centers in nm

    Returns
    -------
    Predicted Absorbance: float
    """
    return h1 * np.exp(-((WL - l1) ** 2) / (2 * w1 ** 2)) + c


def gaussian2(WL,
              h1, l1, w1,
              h2, l2, w2,
              c):
    """
    gaussian(WL, h1, l1, w1)

    computes the predicted absorbance value for given wavelength and Br2 height,
    with two additional Gaussian-like peaks to fit the NaBr3 peak contribtution.

    Parameters
    ----------
    WL: scalar
        Wavelength in nm

    h1, h2 : scalar
        Height of total Br2 spectrum

    w1, w2: scalar
        NaBr3 peak widths in nm

    l1, l2: scalar
        NaBr3 peak centers in nm

    Returns
    -------
    Predicted Absorbance: float
    """
    return (
```

```
        h1 * np.exp(-((WL - l1) ** 2) / (2 * w1 ** 2)) +
        h2 * np.exp(-((WL - l2) ** 2) / (2 * w2 ** 2)) +
        c
    )


def gaussian3(WL,
              h1, l1, w1,
              h2, l2, w2,
              h3, l3, w3,
              c):
    """
    gaussian3(x, h1, l1, w1, h2, l2, w2, h3, l3, w3, c)

    computes the predicted absorbance value for given wavelength and Br2 height,
    with two additional Gaussian-like peaks to fit the NaBr3 peak contribution.

    Parameters
    ----------
    WL: scalar
        Wavelength in nm

    h1, h2, h3: scalar
        Peak heights in absorbance units

    w1, w2, w3: scalar
        Peak widths in nm

    l1, l2, l3: scalar
        Peak centers in nm

    c: scalar
        vertical offset to account for light scattering by powder

    Returns
    -------
    Predicted Absorbance: float
    """
    return (
        h1 * np.exp(-((WL - l1) ** 2) / (2 * w1 ** 2)) +
        h2 * np.exp(-((WL - l2) ** 2) / (2 * w2 ** 2)) +
        h3 * np.exp(-((WL - l3) ** 2) / (2 * w3 ** 2)) +
        c
    )


def gaussian4(WL,
              h1, l1, w1,
              h2, l2, w2,
              h3, l3, w3,
              h4, l4, w4,
              c):
    """
    gaussian3(x, h1, l1, w1, h2, l2, w2, h3, l3, w3, c)

    computes the predicted absorbance value for given wavelength and Br2 height,
    with two additional Gaussian-like peaks to fit the NaBr3 peak contribtution.

    Parameters
    ----------
    WL: scalar
        Wavelength in nm

    h1, h2, h3, h4: scalar
```

```
        Peak heights in absorbance units

    w1, w2, w3, w4: scalar
        Peak widths in nm

    l1, l2, l3, l4: scalar
        Peak centers in nm

    c: scalar
        vertical offset to account for light scattering by powder

    Returns
    -------
    Predicted Absorbance: float
    """
    return (
        h1 * np.exp(-((WL - l1) ** 2) / (2 * w1 ** 2)) +
        h2 * np.exp(-((WL - l2) ** 2) / (2 * w2 ** 2)) +
        h3 * np.exp(-((WL - l3) ** 2) / (2 * w3 ** 2)) +
        h4 * np.exp(-((WL - l4) ** 2) / (2 * w4 ** 2)) +
        c
    )


def gaussian5(WL,
              h1, l1, w1,
              h2, l2, w2,
              h3, l3, w3,
              h4, l4, w4,
              h5, l5, w5, c):
    """
    gaussian3(x, h1, l1, w1, h2, l2, w2, h3, l3, w3, c)

    computes the predicted absorbance value for given wavelength and Br2 height,
    with two additional Gaussian-like peaks to fit the NaBr3 peak contribtution.

    Parameters
    ----------
    WL: scalar
        Wavelength in nm

    h1, h2, h3, h4, h5: scalar
        Peak heights in absorbance units

    w1, w2, w3, w4, w5: scalar
        Peak widths in nm

    l1, l2, l3, l4, l5: scalar
        Peak centers in nm

    c: scalar
        vertical offset to account for light scattering by powder

    Returns
    -------
    Predicted Absorbance: float
    """
    return (
        h1 * np.exp(-((WL - l1) ** 2) / (2 * w1 ** 2)) +
        h2 * np.exp(-((WL - l2) ** 2) / (2 * w2 ** 2)) +
        h3 * np.exp(-((WL - l3) ** 2) / (2 * w3 ** 2)) +
        h4 * np.exp(-((WL - l4) ** 2) / (2 * w4 ** 2)) +
        h5 * np.exp(-((WL - l5) ** 2) / (2 * w5 ** 2)) +
        c
```

```
192     )
193
194
195 def linear(x, a, b):
196     return a * x + b
197
198
199 # Note that all code must be indented with 4 spaces
200 # Pay close attention to line lengths!
201 # In order to compile the Tex document in Terminal:
202 # xelatex -shell-escape DCW_dissertation.tex
```

```python
# data_io.py

import pandas as pd
import numpy as np

def clean_cary_uvvis_data(filename):
    """
    Import and clean raw UV-Vis kinetics data from Cary BioVis software.

    :param filename: string.  path to raw UV-Vis kinetics datafile as csv.
    (Raw datafile exported from Cary BioVis spectrophotometer software.)

    :return: Pandas DataFrame
    """
    df = pd.read_csv(filename, skiprows=1)

    time_rows = df['Wavelength (nm)'].values == '[Time] '
    time_indices = np.argwhere(time_rows).flatten()
    time_vals = df['Abs'][time_indices].values.astype(float)

    non_data_cols = df['Wavelength (nm)'].values == '[Wavelength] '
    n_cols_to_delete = len(np.argwhere(non_data_cols).flatten())

    last_wavelength_index = np.argwhere(pd.isnull(df['Abs'].values))[0][0]

    df = df.drop(df.index[last_wavelength_index:])
    df = df.drop(df.columns[2::2], axis = 1)
    df = df.set_index('Wavelength (nm)')
    if n_cols_to_delete > 0:
        df = df.drop(df.columns[-n_cols_to_delete:], axis = 1)

    n_rows = df.shape[1]
    df.columns = range(n_rows)

    df = df.sort_index()

    return df, time_vals

def clean_agilent_uvvis_data(filename):
    """
    Import and clean raw UV-Vis kinetics data from Agilent UV-Vis software.

    :param filename: string.  path to raw UV-Vis kinetics datafile as .TXT.
    (Raw datafile exported from Agilent UV-Vis spectrophotometer software.)

    :return:Pandas DataFrame
    """
    df = pd.read_csv(filename, encoding='utf-16', skiprows=5, sep='\t')

    df = df.transpose()

    df_t = df.iloc[[0]].values[0]/60.0

    return df, df_t

def write_concs(run_concs, TIME_LABEL, HALOGEN_LABEL, TRIHALIDE_LABEL, name):
    """
    write_concs(run_concs, name)

    Write time, [Br2], [NaBr3] as space-separated values to a file ('name.txt')

    Parameters
    ----------
```

```
    run_concs: a tuple containing three NumPy arrays: time, [Br2], [NaBr3]

    name: a string in quotes. This is the prefix of the file to be written.
        '.txt' will be appended to the end of the prefix.
    """
    with open(name + '.txt', 'w') as outfile:
        outfile.write('%s,%s,%s\n' % (TIME_LABEL,
                                      HALOGEN_LABEL,
                                      TRIHALIDE_LABEL))
        for i in range(len(run_concs[0])):
            outfile.write(str(run_concs[0][i]) + ',' +
                          str(run_concs[1][i]) + ',' +
                          str(run_concs[2][i]) + '\n')
```

Biography

David Cooper Wallace was born to Beth and Tim Wallace in Skagit Valley, Washington on November 19th, 1987. He was homeschooled during grades 3 through 11 before completing his high school education at Burlington Edison High. He attended Whitman college in Walla Walla, Washington, where he majored in chemistry and served in leadership roles on the snowboarding team, jazz ensemble, and interfraternity council. During his undergraduate education, David participated actively in research as an analytical chemist working under Professor Frank Dunnivant at Whitman, and under Professor Robert Wood at the University of Washington. In his graduate studies at Johns Hopkins University, under the guidance of Professor Tyrel M. McQueen, David has focused on the synthesis, physical properties and chemical reactivity of iridium oxide materials. David earned his Master of Arts degree in June 2013, and his Doctor of Philosophy degree in May 2016.